DELFT UNIVERSITY OF TECHNOLOGY

MASTER THESIS

On Modelling of FRP Wrapped Steel CHS joints

Author:
Daan GRÜNDEMAN
4207718

Supervisors:
dr.ir. F.P. VAN DER MEER
dr. M. PAVLOVIC
Prof.dr.ir L.J. SLUYS

November 4th, 2019

On Modelling of FRP Wrapped Steel CHS Joints

Master Thesis

by

D. L. Gründeman

in partial fulfilment of the requirements for the degree of

Master of Science

in Civil Engineering

at the Delft University of Technology,

to be defended publicly on Monday November 18, 2019 at 14:30.

Student number:	4207718	
Thesis committee:	Dr. ir. F. P. van der Meer,	TU Delft, Chairman
	Prof. dr. L. J. Sluys,	TU Delft
	Dr. M. Pavlovic,	TU Delft, Supervisor

An electronic version of this thesis is available at http://repository.tudelft.nl/.

TU Delft

ABSTRACT

The design of steel structures consisting mostly of Circular Hollow Sections (CHS) such as jacket structures and bridges is governed by fatigue loading due to the low fatigue resistance of the welded regions. A solution has been proposed where welding is completely avoided, thus eliminating the weakest factor of these structures. In this solution, joints are wrapped in FRP, which is bonded to the steel. Simple Finite Element (FE) models of these joints already exist. In this thesis, these models will be further developed in Abaqus for more accurate prediction of the behaviour of such FRP wrapped joints. A set of model and solver parameters will be established as a starting point for more detailed modelling of FRP wrapped joints with different geometry and static load conditions.

Because of large complexity of the models, and inclusion of many contact interactions, Abaqus/Explicit should be used to model such joints. The anisotropic nature of the FRP requires elements that are robust and able to handle this anisotropy. Also the complex, curved and layered geometry of the wrap requires elements that discretize a 3D volume. Without the use of user subroutines, continuum shell elements are the only elements that meet this requirement.

Prediction of the behaviour of axial joints was very accurate, although no unique set of input parameters for the Cohesive Zone Model were found. This is because multiple failure modes occur at the same time, which makes the system very sensitive to some parameters and completely insensitive to other parameters. Prediction of more complex X-joints was not very accurate. This is mostly due to differences between the geometry of the model and the real life joint. The models did suffer from hourglass modes. Different methods of hourglass control had limited effect. It was found that as irregularity of the mesh increases, the effects of hourglass modes decreases. However, the effect of hourglass modes needs to be decreased further. A solution to do this is proposed at the end of this thesis.

PREFACE

This thesis represents for me the end of an amazing phase of my life as a TU Delft student. But nevertheless, it also represents the beginning of new adventures and opportunities in the future. My choice to study Civil Engineering as a bachelors and Structural Engineering as a masters enabled me to find the interesting topic that is elaborated in this thesis.

To start at where it all began, I would like to thank Dr. M. Pavlovic for his suggestion to investigate this special research topic. Also I found our 2 weekly meetings very helpful. Exploring different modelling possibilities for this new joining method has been very interesting. I would like to extend my gratitude to Prof. Dr. Ir. L.J. Sluys for being part of the graduation committee. I also would like to thank Dr. Ir. F.P. van der Meer for being the chair of the graduation committee and the elaborate feedback on the draft version of this thesis.

I would like to thank my parents and sister for always supporting me during my studies and for their solicited and unsolicited advice.

I also would like to thank my friends for the company and fun activities. From the J22 campaign I sailed with Maarten and Joren, to making trips to München and Trondheim. But also smaller things, like eating together and drinking beers or watching a Formula 1 race. But also just the small talks over a coffee at the university.

Finally I would like to thank my girlfriend Janna for her unconditional love and support during this my studies and this thesis.

Daan Gründeman

Delft, November 4th, 2019

Contents

1

INTRODUCTION

1.1. BACKGROUND

Circular hollow sections (CHS) are used in a variety of steel structures, amongst which jacket structures and bridges are the most common. For these structures, fatigue loading is often the governing load in the design of these structures. Traditionally, the joints in these structures are made by welding. However, it is the welds that form the most critical part of the structure when regarding the fatigue resistance. The low fatigue resistance of the welds leads to overdimensioning of the members in the structures and prevents the use of high strength steel.

Figure 1.1: FRP wrapped joint [1]

To overcome this, an alternative joining method has been proposed. This joining method relies on an adhesive bond between the steel members and an Fibre Reinforced Polymer (FRP) wrap. This FRP wrap is wrapped around the joint in such a way that force transfer from one brace member to another brace or chord member is optimal. In figure 1.1, a joint which is wrapped in the manner described is shown.

Tensile tests were performed on the joint with the X90 geometry from figure 1.1 as well as on axial joints with a similar design. The specimens were clamped on the top side and a displacement was applied to the bottom side of the joint. The specimen with the X90 geometry failed by debonding, however, a circumferential crack was observed around the brace member at the root of the joint. The axial joints also failed by debonding, but final failure was normal failure of the bond initiated by yielding, and subsequently contraction of the cross-section of the steel member. The force-displacement curves of these specimen are shown in figure 1.2.

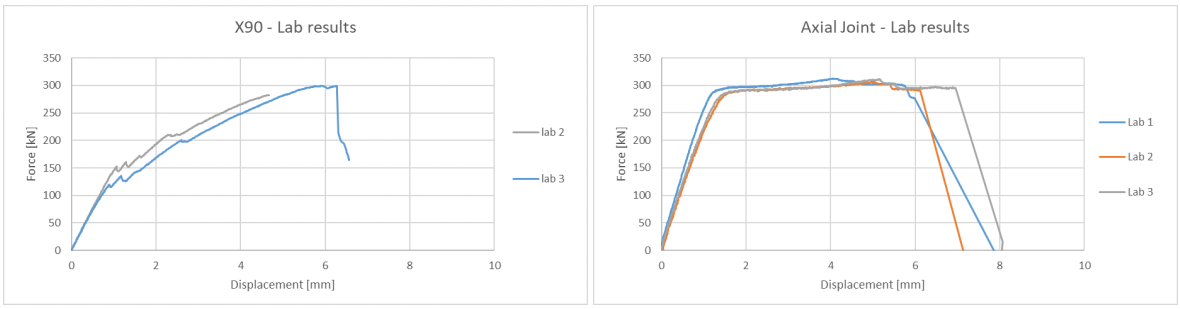

(a) Force-displacement curves X90 joint.[1]

(b) Force-displacement curves axial joint.

Figure 1.2: Force-displacement curves obtained from lab experiments

Models to describe the behaviour of such joints already exist, but these models are over-simplified, the FRP is modelled as a single homogenous isotropic piece of material and only debonding is included as a failure mode. However, they do provide a moderately good prediction of the force-displacement curve of the joints.[1] Therefore, in this thesis, the existing models will be made more comprehensive by adding complexity to the geometry, improving the model to describe debonding failure and including failure of the FRP itself. The goal of this thesis is for the final models to have similar force-displacement curves and similar failure modes as were observed in the lab. Abaqus was used for making the models from [1] and Abaqus offers many possibilities for modelling composites, therefore, the models in this thesis will also be made in Abaqus. It must be noted that the focus in this thesis is on developing a method for accurate modelling such joints, not on necessarily on the results of the models.

It is well known that under certain circumstances, Finite Element (FE) models can show some erratic behaviour called hourglass modes. This phenomenon will be described in this thesis, so will option to mitigate this behaviour.

1.2. RESEARCH QUESTION

The research question that will be answered in this thesis is as follows: '*How can FRP wrapped joints be modelled in an accurate way?*'

This question will be answered through four sub-questions:

1. Which solver and element types should be used to model FRP wrapped joints?
2. How can debonding of FRP wrapped joints be modelled?
3. How can failure of the FRP wrap be modelled?
4. How should hourglass modes be dealt with?

1.3. METHODOLOGY AND OUTLINE

First, a literature study is presented. In this literature study, several aspects of modelling composites will be elaborated. Also, cohesive zone modelling is explained.

In chapter 3, some choices in modelling strategy are explained.

In chapter 4, models describing the elastic behaviour of the wrapped joint are described, gradually adding complexity to the models. Also the results of static stress/displacement analyses will be compared to the results of explicit dynamic analyses.

In chapter 5, debonding of between the steel and FRP is discussed.

In chapter 6, a description of how the models describing failure of the FRP wrap is given

In chapter 7, hourglass modes and how to handle them are discussed.

In chapter 8, the conclusions can be found.

2

MODELLING OPTIONS

In this chapter some options for modelling are described. A description of element types will be given, as will as different solvers. Also a Cohesive Zone Model (CZM) and a failure model of the FRP will be described.

2.1. ELEMENT TYPES

2.1.1. SOLID ELEMENTS

Three-dimensional solid elements are the standard volume elements of Abaqus. The shapes a three-dimensional solid elements are available in in Abaqus are shown in figure 2.1. Solid element can be composed of a single homogeneous material, however, in Abaqus/Standard, solid elements can also include layers of different materials, which can be used for the analysis of laminated composites.

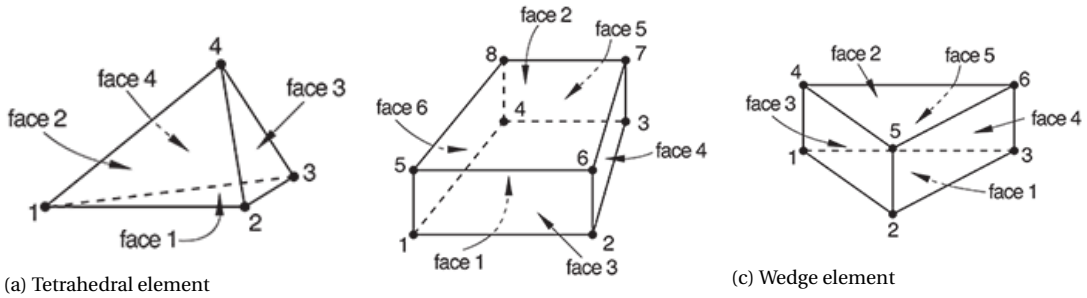

(a) Tetrahedral element

(b) Hexahedral element

(c) Wedge element

Figure 2.1: Element shapes

2.1.2. CONTINUUM SHELL ELEMENTS

For thin-walled structures another class of elements is frequently used. These elements are called shell elements. In shell elements, the geometry is defined at a reference surface, which is then used to discretize a body.
Contrary to regular shell elements, the thickness of continuum shell elements is determined from the element nodal geometry. This means that continuum shell elements can only be hexahedral or wedge elements. Continuum shell elements have only displacement

degrees of freedom, where conventional shell elements also have rotational degrees of freedom. The kinematic and constitutive behaviour of continuum shell elements is very similar to that of conventional shell elements. This is clarified by figure 2.2. When continuum shell elements are used, the thickness direction and the stacking direction of the elements needs to be defined. When modelling composites, both the stacking direction and the stiffness direction should be in the out-of-plane direction of the laminate.

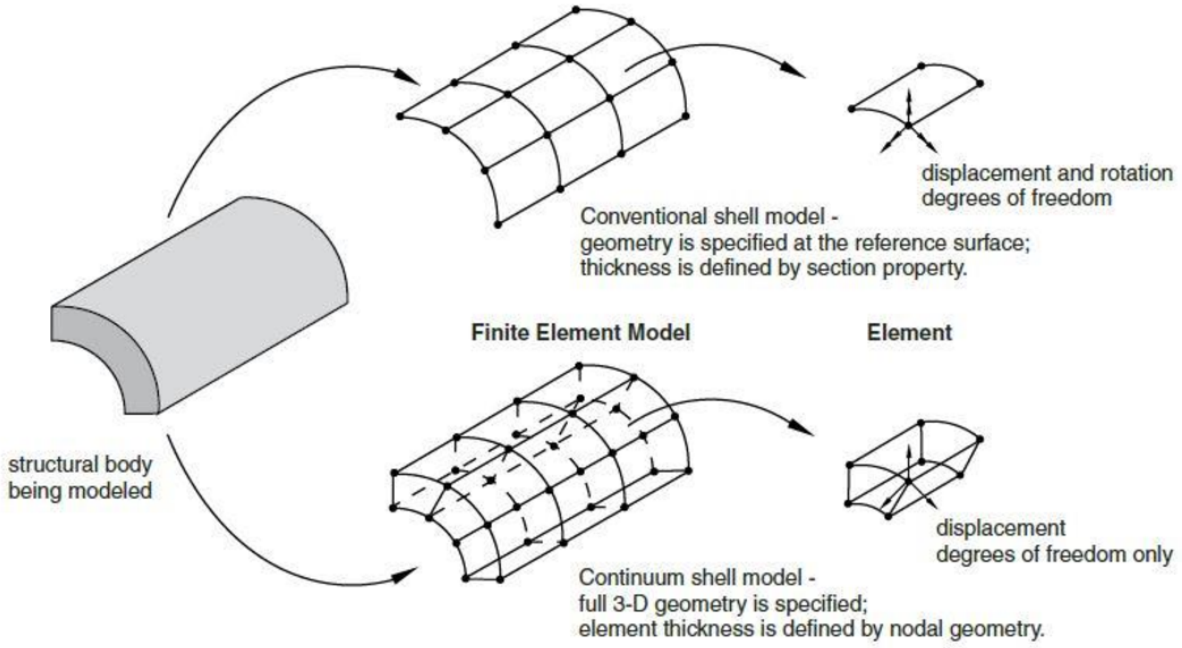

Figure 2.2: Difference between continuum shell and conventional shell elements[2]

2.1.3. HOURGLASS MODES

The final step of discretization of the elements is numerical integration. In order to perform this numerical integration, integration points and an integration scheme are needed. In general, full integration is recommended, this means that the solution obtained through the numerical integration scheme is exact. However, in some elements and certain applications, using full integration leads to problems such as shear locking, elements having an overly stiff response when subjected to bending. To overcome these problems reduced integration can be applied to elements. A reduced integration scheme uses less integration points than a full integration scheme.

A drawback of using reduced integration schemes is that this leaves the possibility for deformation modes to exist which do not contribute to the energy in the system. These deformation modes are called 'hourglass' modes. Examples of these hourglass modes are shown in figure 2.3. In many cases, these hourglass modes are restrained by neighbouring elements. For models where hourglass modes are not restrained by neighbouring elements, various hourglass control methods are implemented in Abaqus.

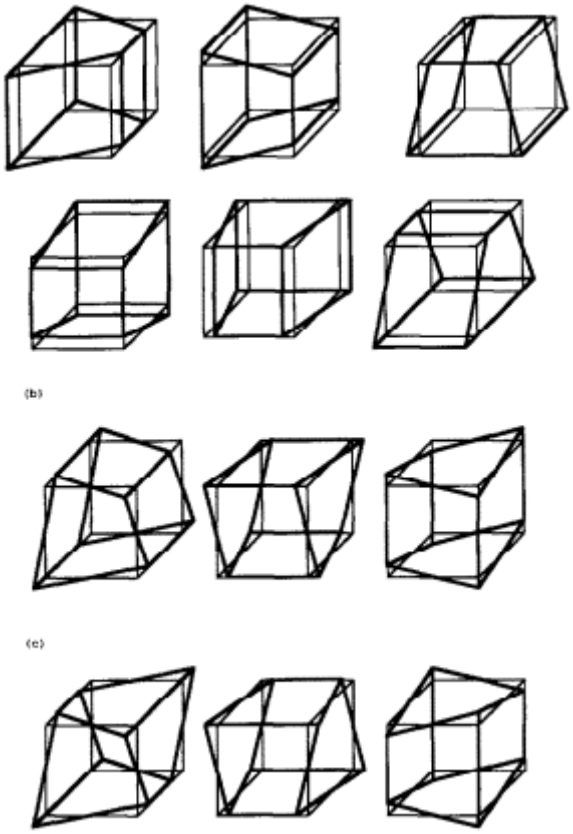

Figure 2.3: Hourglass modes for an eight-noded brick element [3]

HOURGLASS CONTROL

The stiffness hourglass control method is recommended for quasi-static and transient dynamic simulations. It is based on the pure stiffness form of the Kelvin viscoelastic approach. The relax stiffness hourglass control method is based on the integral viscoelastic approach. It generates more resistance to hourglass forces early in the analysis step. The enhanced hourglass control method is a refinement of the stiffness hourglass control method, based on the enhanced assumed strain method. More information on these hourglass control methods is found in the Abaqus Analysis User's Manual [4].

The hourglass control methods mentioned above are available eight-noded three dimensional solid elements and eight-noded continuum shell elements. No hourglass control methods are available for wedge elements in Abaqus.

Hourglass modes do not need any energy to occur, but hourglass control does need energy to work. This energy is can be found in the 'Artificial Strain Energy' output variable in Abaqus. A method for assessing the severity of hourglassing is to compare this artificial strain energy to the strain energy. The artificial strain energy should be negligible compared to the strain energy. This method combined with visual inspection of the output is sufficiently accurate to obtain meaningful results regarding hourglass behaviour. Because no hourglass control methods are available for wedge elements, this method cannot be used for assessing hourglass behaviour in models with wedge elements. These models can be assessed through visual inspection.

2.2. ABAQUS/STANDARD VS. ABAQUS/EXPLICIT SOLVERS

For modelling of experiments with static loading, Abaqus offers two solvers, Abaqus/Standard and Abaqus/Explicit. Both these solvers will be explained in this section.

2.2.1. ABAQUS/STANDARD

Abaqus/Standard can be used for static stress/displacement analyses. It can be used for linear and nonlinear analyses. A step time is defined in static stress/displacement analyses with Abaqus/Standard, but this step time does not have any physical meaning since no natural time scale is present in the analyses in this thesis.

2.2.2. ABAQUS/EXPLICIT

An explicit dynamic analysis can, amongst other things, be used to perform quasi-static analyses with complicated contact conditions. An advantage of Abaqus/Explicit is that for large models, it is faster than Abaqus/Standard. This is visualised in figure 2.4.

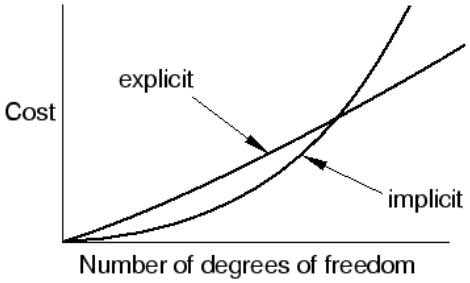

Figure 2.4: Computational cost [4]

TIME INTEGRATION

This explicit dynamic procedure Abaqus/Explicit uses, is an explicit central-difference time integration rule. The result of this is that each increment is relatively inexpensive. The explicit central-difference operator satisfies the dynamic equilibrium equations at the beginning of the increment, t; the accelerations calculated at time t are used to advance the velocity solution to time $t + \Delta t/2$ and the displacement solution to time $t + \Delta t$.

The central-difference operator is stable under the condition that:

$$\Delta t \leq \frac{2}{\omega_{max}}$$

Where ω_{max} denotes the highest frequency of the system.
This stability limit can be approximated in terms of the smallest element dimension in the mesh and the dilatational wave speed.

$$\Delta t \approx \frac{L_{min}}{c_d}$$

The dilatational wave speed is a function of the effective Lamé's constants, $\hat{\lambda}$ and $\hat{\mu}$, and the density of the material.

$$c_d = \sqrt{\frac{\hat{\lambda} + 2\hat{\mu}}{\rho}}$$

The stability limit of the central-difference operator must be satisfied, otherwise the solution will become unstable. In non-linear problems the highest frequency of the model will continually change, leading to a continuously changing stability limit. To cope with this changing stability limit, Abaqus/Explicit offers fully automatic time incrementation,

where the time increments are continuously adapted to the stability limit.[4] The stable time increment depends on the dilatational wave speed, which depends on the density of the material. This means that the stable time increment can be increased by scaling the density of the materials. Abaqus/Explicit uses this mass scaling to increase the stable time increment, this can significantly reduce the computational cost of the models. It is possible to specify a target stable time increment, Abaqus/explicit will determine mass scaling factors for the element in such a way that this specified time increment in stable.

2.3. COHESIVE ZONE MODELLING

The bond between the steel and FRP is modelled using a Cohesive Zone Model (CZM). The cohesive zone model has three main input parameters, the stiffness of the bond, the strength of the bond and the fracture energy of the bond. These parameter have to be specified in normal direction and in both shear directions.

2.3.1. TRACTION-SEPARATION BEHAVIOUR

Figure 2.5 shows typical traction-separation behaviour. t_n^t represents the strength of the bond, δ_n^0 represents the displacement (separation) at which the stress (traction) reaches the strength and δ_n^t represents the displacement at which the bond completely fails.

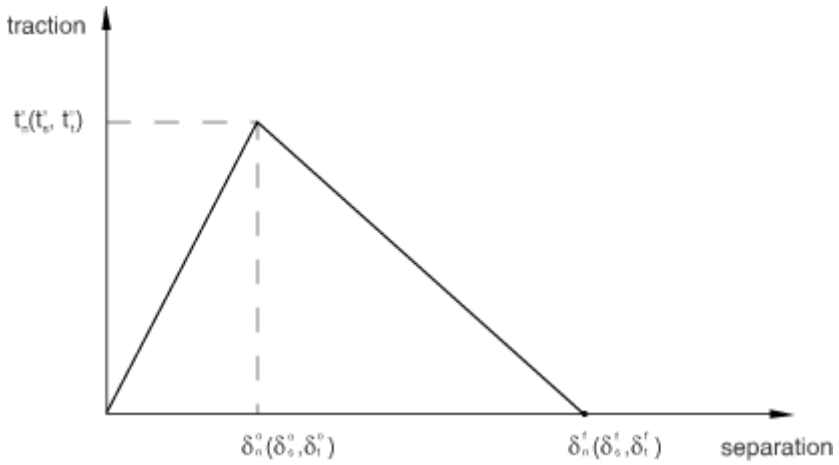

Figure 2.5: Typical traction separation behaviour[4]

DEFAULT STIFFNESS

Abaqus offers the option to use a default enforcement method to determine the initial stiffness of the traction-separation behaviour. This default stiffness is based on the stiffnesses of the surfaces in contact and is calculated by Abaqus.

2.3.2. INTERFACE DAMAGE

The damage initiation criterion that is used in this thesis is the quadratic traction criterion. This criterion is seen in equation 2.1. When the criterion reaches one, damage is initiated and starts evolving. The rate at which the damage evolves is governed by the fracture energy. The fracture energy is the area under the curve in figure 2.5. This means that when the fracture energy is very high, evolution of the damage is slow and vice versa.

$$\left\{\frac{\langle t_n \rangle}{t_n^o}\right\}^2 + \left\{\frac{t_s}{t_s^o}\right\}^2 + \left\{\frac{t_t}{t_t^o}\right\}^2 = 1 \tag{2.1}$$

2.4. FRP FAILURE MODEL

In this thesis, failure of the FRP wrap is modelled using the Hashin damage option. The Hashin damage model is designed to predict failure of unidirectional (UD) plies. The Hashin damage option consists of three parts, damage initiation, damage evolution and damage stabilization.

2.4.1. ELASTIC MATERIAL MODEL

2.4.2. HASHIN CRITERIA

The Hashin criteria[4] take four failure modes into account; fibre tension, fibre compression, matrix tension and matrix compression. The fibre tension damage initiation criterion is as follows:

$$F_f^t = \left(\frac{\hat{\sigma}_{11}}{X^T}\right)^2 + \alpha\left(\frac{\hat{\tau}_{12}}{S^L}\right)^2, \quad \hat{\sigma}_{11} \geq 0 \tag{2.2}$$

The fibre compression damage initiation criterion is as follows:

$$F_f^c = \left(\frac{\hat{\sigma}_{11}}{X^C}\right)^2, \quad \hat{\sigma}_{11} \leq 0 \tag{2.3}$$

The matrix tension damage initiation criterion is as follows

$$F_m^t = \left(\frac{\hat{\sigma}_{22}}{Y^T}\right)^2 + \left(\frac{\hat{\tau}_{12}}{S^L}\right)^2, \quad \hat{\sigma}_{22} \geq 0 \tag{2.4}$$

The matrix compression damage initiation criterion is as follows:

$$F_m^c = \left(\frac{\hat{\sigma}_{22}}{2S^T}\right)^2 + \left[\left(\frac{Y^C}{2S^T}\right)^2 - 1\right]\frac{\hat{\sigma}_{22}}{Y^C} + \left(\frac{\hat{\tau}_{12}}{S^L}\right)^2, \quad \hat{\sigma}_{22} \leq 0 \tag{2.5}$$

Where X^T is the longitudinal tensile strength, X^C is the longitudinal compressive strength, Y^T is the transverse tensile strength, Y^C is the transverse compressive strength, S^L is the longitudinal shear strength and S^T is the transverse shear strength. $\hat{\sigma}_{11}$ is the stress in longitudinal direction, $\hat{\sigma}_{22}$ is the stress in transverse direction, $\hat{\tau}_{12}$ is the shear stress and α is a coefficient that determines the contribution of the shear stress to the fibre tension initiation criterion.[4]

2.4.3. DAMAGE EVOLUTION

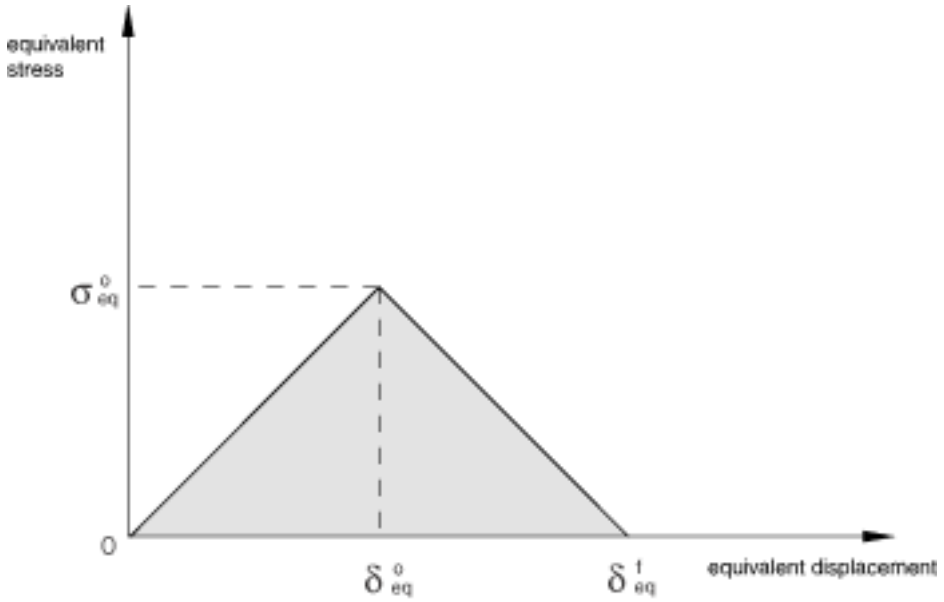

Figure 2.6: Evolution of Hashin damage, each failure mode has individual damage evolution.

The evolution of FRP damage is very similar to the evolution of cohesive damage. To describe the damage evolution of Hashin damage, Abaqus uses a characteristic element length to reduce mesh dependency in the evolution of damage. Damage is determined using, amongst other parameters, the equivalent stress and equivalent displacement. The equivalent displacement is a function of strain and the characteristic element length and the equivalent stress is a function of stress, strain and the characteristic element length.[4]

3

MODELLING APPROACH

In this chapter the approach that has been taken to modelling will be explained. The general concept is that complexity will be gradually added to the models. The choices regarding the areas where complexity was added will be explained in this chapter.

The starting point of modelling is the model made by M. Liatzouras[1]. In this model, the FRP wrap is modelled as one solid, linear elastic, isotropic piece of material and the input values for the CZM are based on tuning of the parameters to match a force-displacement curve. In order to improve this model, first the geometry will be improved and later on the FRP material model and the CZM will be to better mimic the actual behaviour of the bond.

3.1. FRP GEOMETRY

First, the FRP wrap will be kept as one solid piece with a linear elastic, isotropic material. The element types and shapes will be varied, as will the solver that is used to perform the analysis. Differences will be studied between Abaqus/Standard and Abaqus/Explicit. The geometry of these models is displayed in figure 3.1.

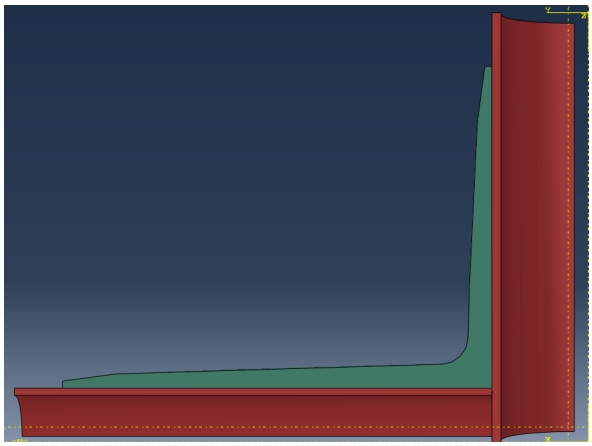

Figure 3.1: Geometry of the single layer models, the steel in colored red, the FRP green

After that, the geometry will be changed so that the FRP is divided into multiple layers, first four, then fourteen. Within these variations in geometry, the element types and solver will again be varied. From the variations mentioned previously, enough information is obtained to make a choice for the geometry, solver type and element type that will be used in future analyses. The geometries of the models with four and fourteen layers are shown in figure 3.2a and figure 3.2b.

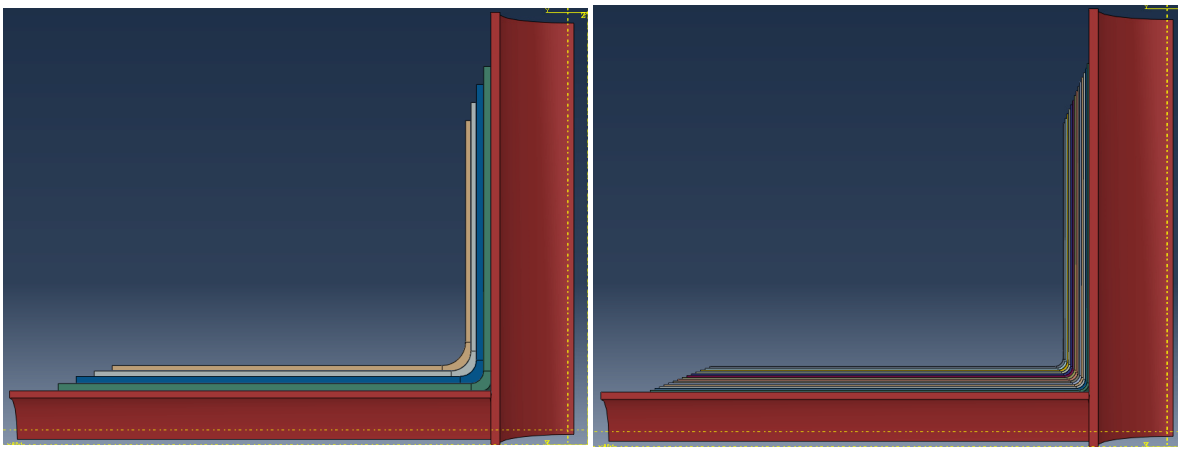

(a) Four layer geometry

(b) Fourteen layer geometry

Figure 3.2: Four and fourteen layer geometries

3.2. BOUNDARY CONDITIONS

As seen in figures 3.1 and 3.2 symmetry boundary conditions are implemented in all three directions. This is done to reduce computational cost. Loading of the model is done via a reference point. This point is connected to the end of the steel brace member through a kinematic coupling, this reference point is then subjected to a prescribed displacement. In the debonding models with three symmetry boundary conditions, only the FRP wrap is constrained by the symmetry boundary condition in the direction of the joint, since the brace member does not continue past the symmetry plane in reality.

3.3. DEBONDING

The CZM will be updated using the axial geometry of the joint. This is done because the debonding failure mode is more isolated in these models and therefore they are better suited to change the CZM. The first step is to make the the model suitable for Abaqus/Explicit. After that, key parameters such as bond shear strength and corresponding fracture energy will be changed to better match the results from the test specimens. Later the geometry will be improved in a similar manner as described in section 3.1. The geometry of the first models is shown in figure 3.3 and the updated geometry is shown in figure 3.4.

Figure 3.3: Geometry of Axial models, with a single layer of FRP

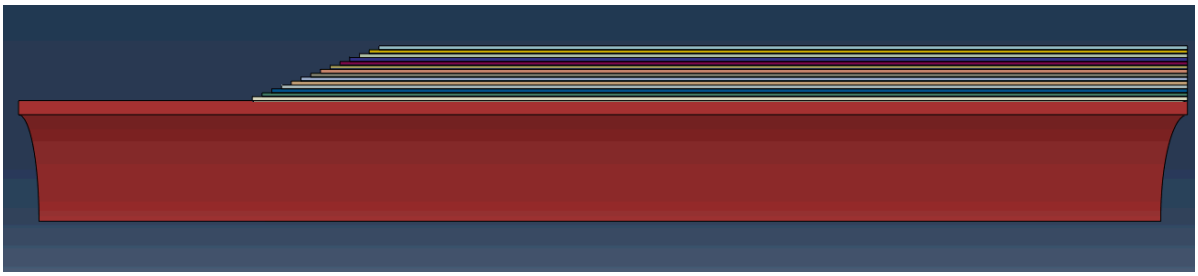

Figure 3.4: Geometry of Axial models, with 14 layers of FRP and symmetry conditions

3.4. FRP LAYUP

In order to model failure of the FRP wrap in a realistic way, it is important that the layup of the FRP is similar to reality. First, for simplicity and to check stability of the model around the moment of failure, the plies will be lumped into an equivalent ply. After that, the plies will be modelled in more detail by including the layup of the wrap. The first step in this is to divide each layer into a ply containing a Chopped Strand Mat (CSM) and a ply containing the bi-directional fabric. The bi-directional fabric is modelled, by lumping two unidirectional plies in a [0°/90°] layup into a single ply. The final step is to approximate the bi-directional fabric by modelling it as a $[0°/90°]_s$ layup. It is currently not possible to model a composite layup with solid elements in Abaqus/Explicit, therefore, these models will be modelled with shell elements.[6]

With this changing geometry and layup, the FRP material model needs to be changed in each step of adding complexity. It is mentioned that in the beginning the FRP is modelled as a linear elastic, isotropic material. This will stay the same until the first time that ply failure will be modelled. For modelling ply failure, Hashin damage will be used. As mentioned in section 2.4, the Hashin criteria are designed for use in UD plies. Therefore, the model with ply failure must be one using UD plies, for more accurate modelling of damage.

4

SOLVER AND ELEMENT TYPES

In this chapter the geometry of the model will gradually be made more complex by adding layers, this is done to mimic the layup of the wrap. In parallel to the process of adding layers, some critical parameters will be determined, such as what element types to use and which solver is most appropriate for these kind of models. First, element types and solvers will be compared to eachother on the original, most simple geometry. This will be repeated for models with a four layer geometry and a fourteen layer geometry.

4.1. SINGLE LAYER OF FRP

4.1.1. IMPLICIT

Three element types have been tried on the single layer geometry, which is shown in figure 4.1. They give very similar results, continuum shell elements and hexahedral solid elements produced exactly the same results. All models fail by debonding failure, this is the only possible failure mode in these models. The force displacement curves of these models can be seen in figure 4.2. Alongside, results from lab tests are plotted. The initial stiffness of the models is slightly lower than the initial stiffness from the lab tests. From the curves from the lab tests, two distinct load drops can be seen before failure of the samples. The models show only gradual stiffness degradation before final failure is initiated. This degradation occurs at a comparable displacement to the displacement at which the second load drop from the lab tests occurs. The load at this moment is higher in the models than in the lab test. This is because the first load drop does not happen in the models. It is also observed that the stiffness of the models after the moments of degradation is similar to the stiffness of the samples. The models show slightly more ductility at final failure than the samples. The model with continuum shell elements suffers convergence issues, it aborts at 5.04 mm displacement.

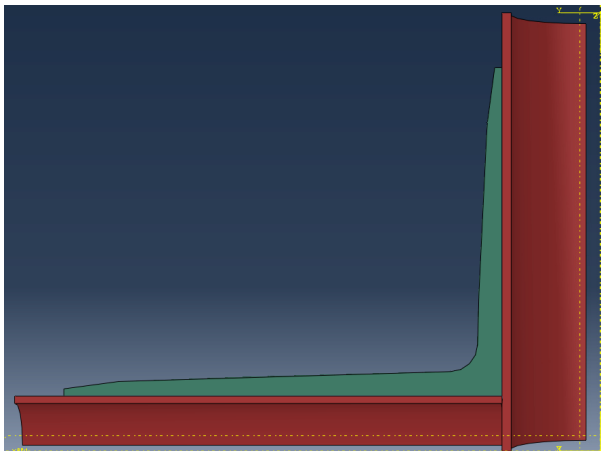

Figure 4.1: Geometry of the single layer models, the steel is colored red, the FRP green

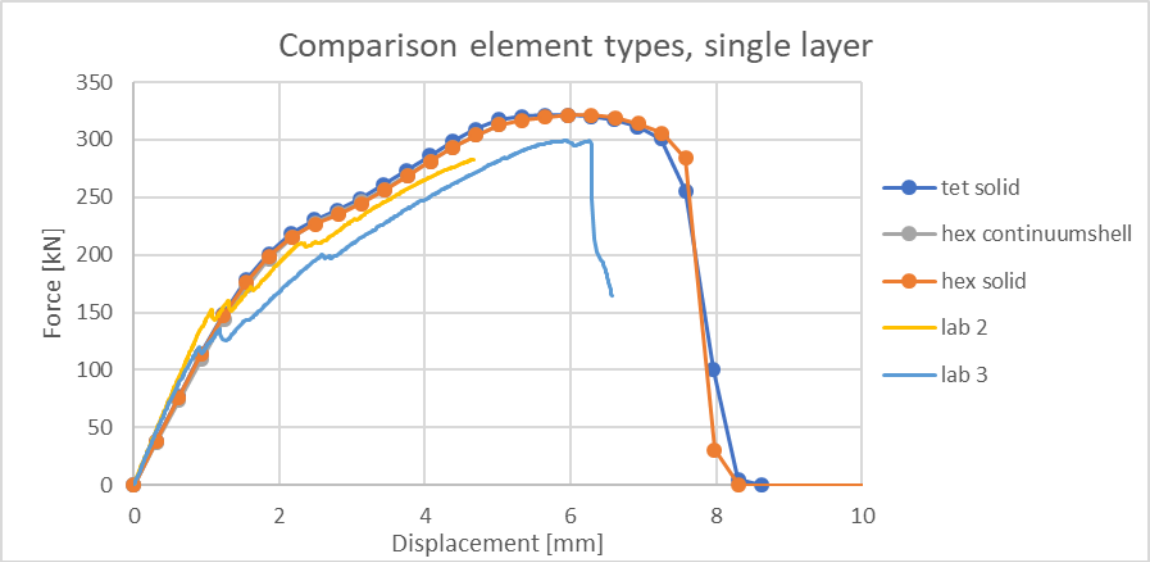

Figure 4.2: Implicit model, single layer of FRP, starting point of modelling

4.1.2. EXPLICIT

Since in the implicit models, the same results where obtained when either solid tetrahedral, solid hexahedral or continuum shell elements where used, only tetrahedral solid elements will be used to make the first explicit models. The geometry that has been used is the same as the one for implicit models.

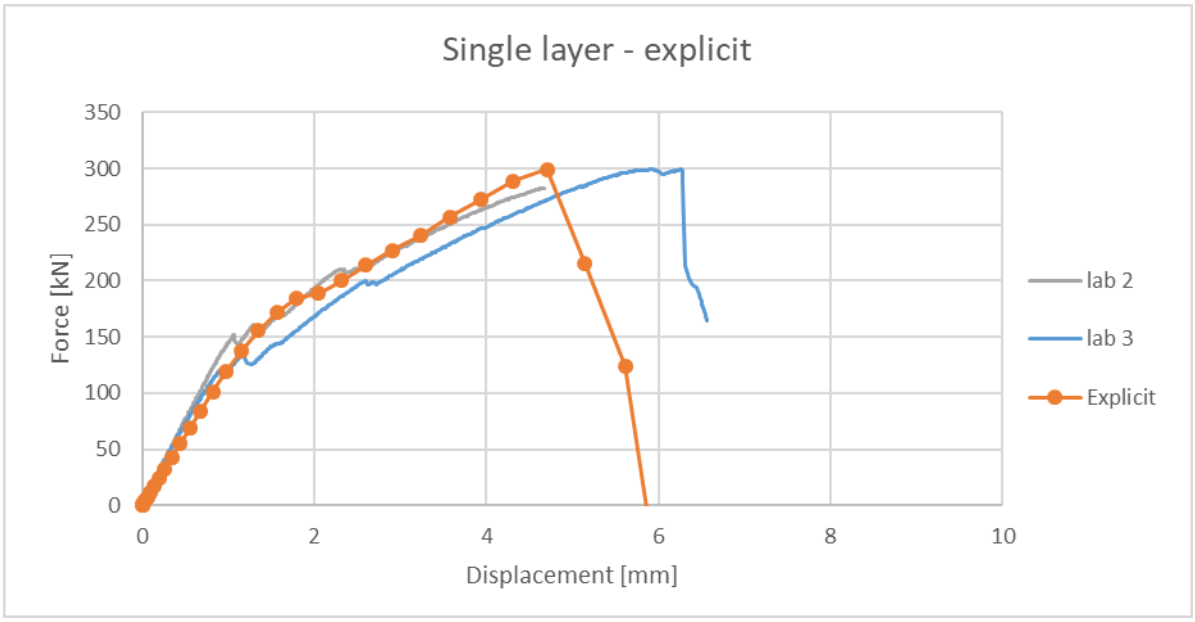

Figure 4.3: Explicit model, single layer of FRP

In figure 4.3 the force-displacement curve of the first explicit model is shown, again combined with the results from the lab tests. It is observed that the initial stiffness of the model is slightly lower than the stiffness of the samples. Similar to the implicit models, there is only gradual stiffness degradation. The curve of the model stays close to the curve of one

of the samples, failing at the same displacement. The ultimate load is the same as for the other sample.

MASTER/SLAVE SURFACE ASSIGNMENTS

To see the influence of the master/slave surface assignment, the master and slave surfaces have been swapped. The results of this are shown in figure 4.4.

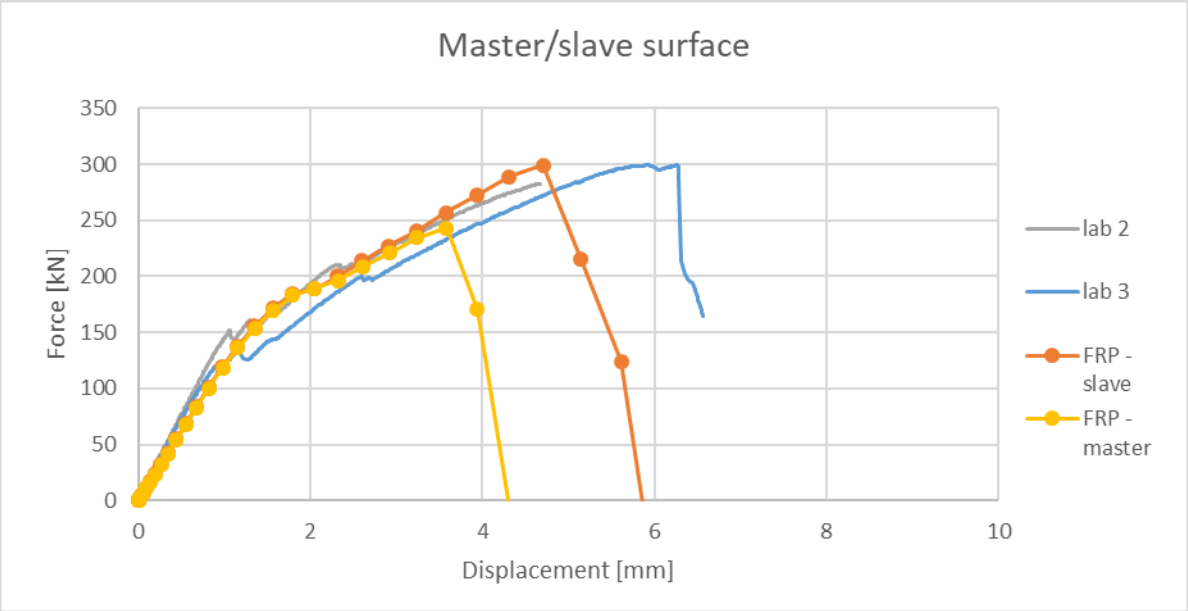

Figure 4.4: Explicit model, the influence of swapping slave and master surfaces

There is no difference until approximately 3 mm displacement, after this moment, failure starts to initiate in the model where the FRP is the master surface. This leads to an underestimation of both the failure load and the ultimate displacement. According to the Abaqus Analysis User's Manual[4] the stiffer structure should be the master surface, which in all models is the steel parts. The results shown in figure 4.4 support this claim.

4.1.3. COMPARISON IMPLICIT EXPLICIT

In figure 4.5 the force displacement curves of the implicit and explicit analysis of the reference model are shown. It can be seen that the curves coincide up to a force level of around 175 kN. At this point, the stiffness of the explicit model decreases, while the implicit model keeps roughly the same stiffness. At a load of approximately 200 kN, the implicit model also loses some stiffness. The explicit model fails in a rather brittle manner at a displacement between 4.5 and 5mm, while the implicit model fails in a more ductile manner with an ultimate displacement of 7.2mm

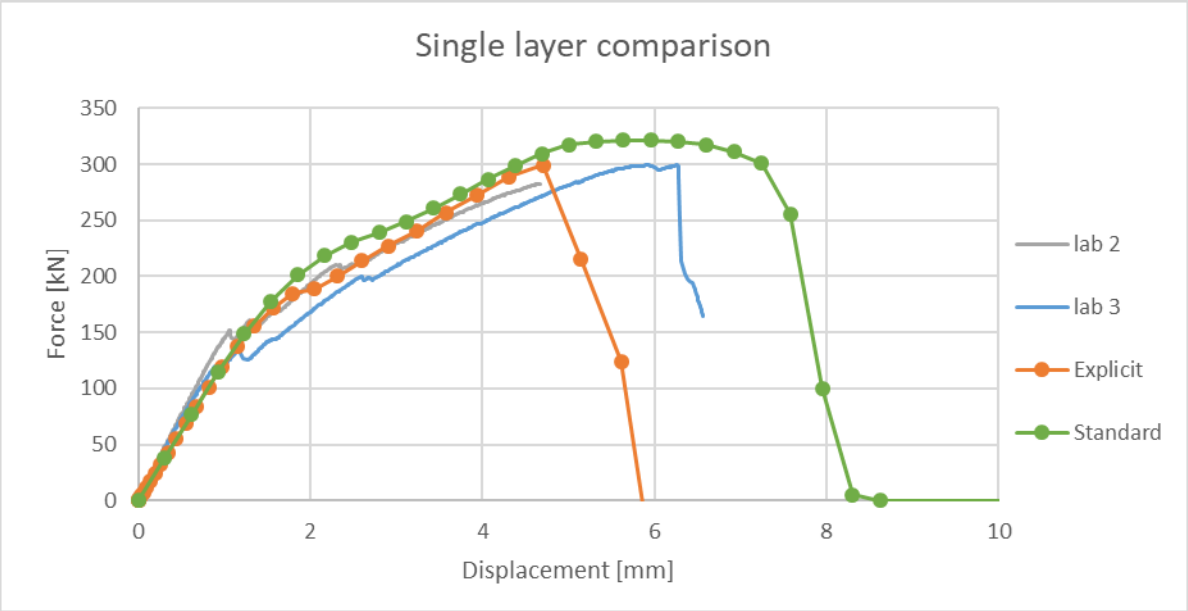

Figure 4.5: Force-displacement curves of implicit and explicit analyses

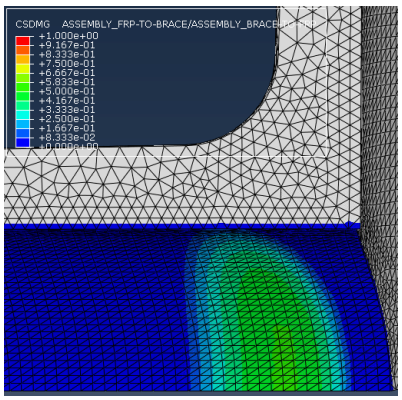

(a) Implicit 1.9 mm

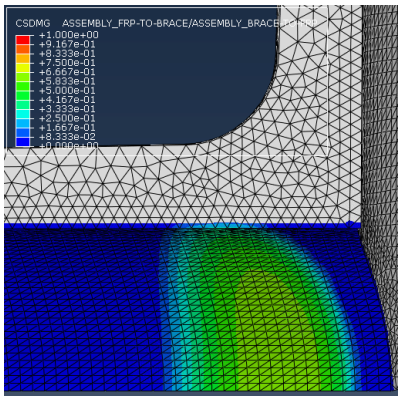

(b) Implicit 2.2 mm

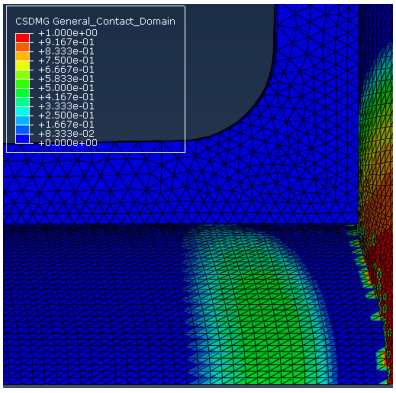

(c) Explicit 1.9 mm

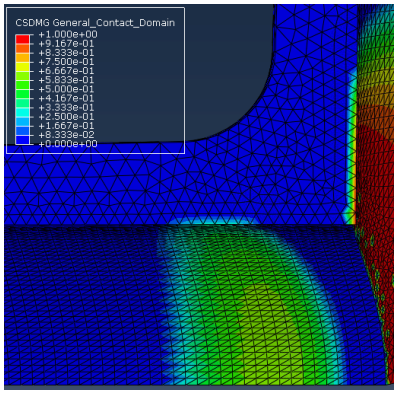

(d) Explicit 2.1 mm

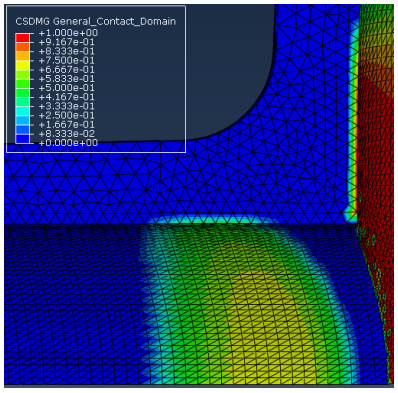

(e) Explicit 2.3 mm

Figure 4.6: Contour plot of the interface damage at the moment where the force-displacement curves (fig. 4.5) start to separate.

In figure 4.6 contour plots of the damage parameter for interface damages are shown. The plots show that some damage has initiated near the root of the joint. From the contour

plots, no clear difference can be observed. In figure 4.7a the value of the damage parameter is plotted along a path at 1.92 mm displacement, running from the root of the joint towards the end of the brace. In this plot, we can observe that there is slightly more damage in the explicit model. Figure 4.7b the value of the damage parameter is plotted along the same path. The same observation is made, there is slightly more damage in the explicit model. This slight difference does not fully explain the difference between the force-displacement curve from figure 4.5. This suggests that there is some other cause. This cause has not yet been found

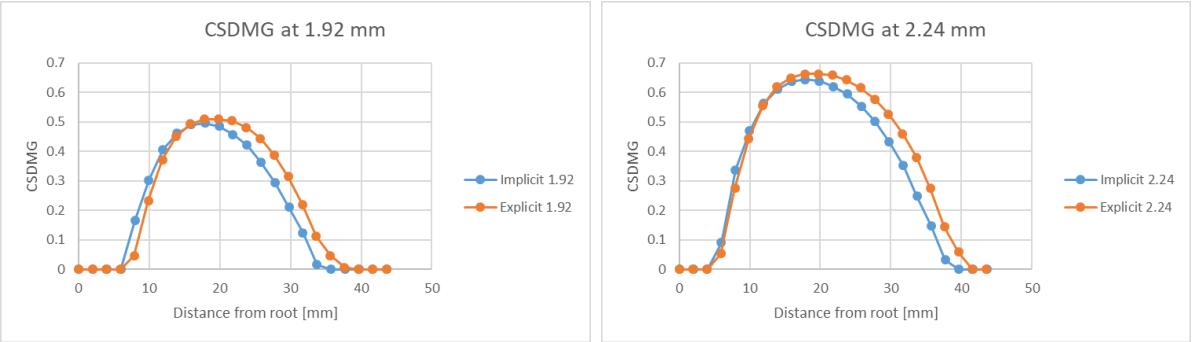

(a) CSDMG at 1.92 mm displacement

(b) CSDMG at 2.24 mm displacement

Figure 4.7: Value of CSDMG plotted along a path running from the root of the joint towards the end of the brace. Values of the explicit model have been interpolated

4.1.4. CONCLUSIONS

From this section it can be concluded that on the geometry with only a single layer of FRP, the difference between using tetrahedral solid, hexahedral solid or hexahedral continuum shell elements. There is a difference in using Abaqus/Standard and Abaqus/Explicit. While the initial stiffness is the same, the strength and displacement at failure are lower when Abaqus/Explicit is used.

4.2. FOUR LAYERS OF FRP

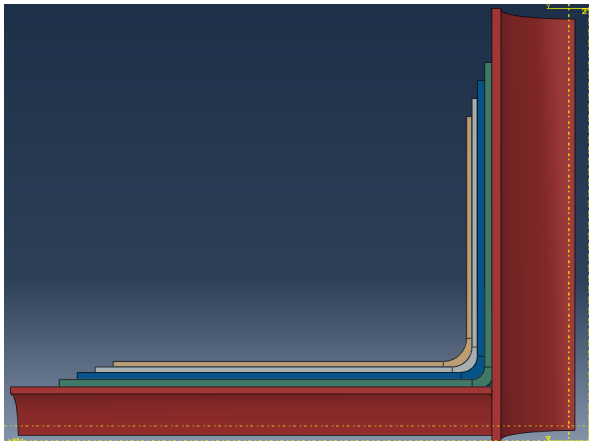

Figure 4.8: Four-layer geometry

For both continuum shell elements and solid elements four meshes have been tested on the four-layer geometry. 2x1, 2x2, 4x1 and 4x2, where the first number represents the approximate in-plane dimensions and the second number the approximate thickness of the element. The four-layer geometry can be seen in figure 4.8. The force-displacement curves of the models with continuum shell elements are shown in figure 4.9. It is observed that the 2x1, 2x2 and the 4x2 yield very similar results. The 4x1 model gives a higher initial stiffness, and later converges to the other models. The initial stiffness of all models is lower than the initial stiffness from the lab tests and stiffness degradation starts at a later moment. After the stiffness degradation, the curves from the models, with exception of the 4x1 model, coincide with the curve of one of the samples. The ultimate load and the ultimate displacement are approximately the same in all models, but both are overestimated, compared to the lab tests. A possible explanation for the lower stiffness of the models is that for the stiffness of the inter-ply interaction, values have been assumed, these may be too low. A better alternative might be to use the default stiffness option for these stiffnesses.

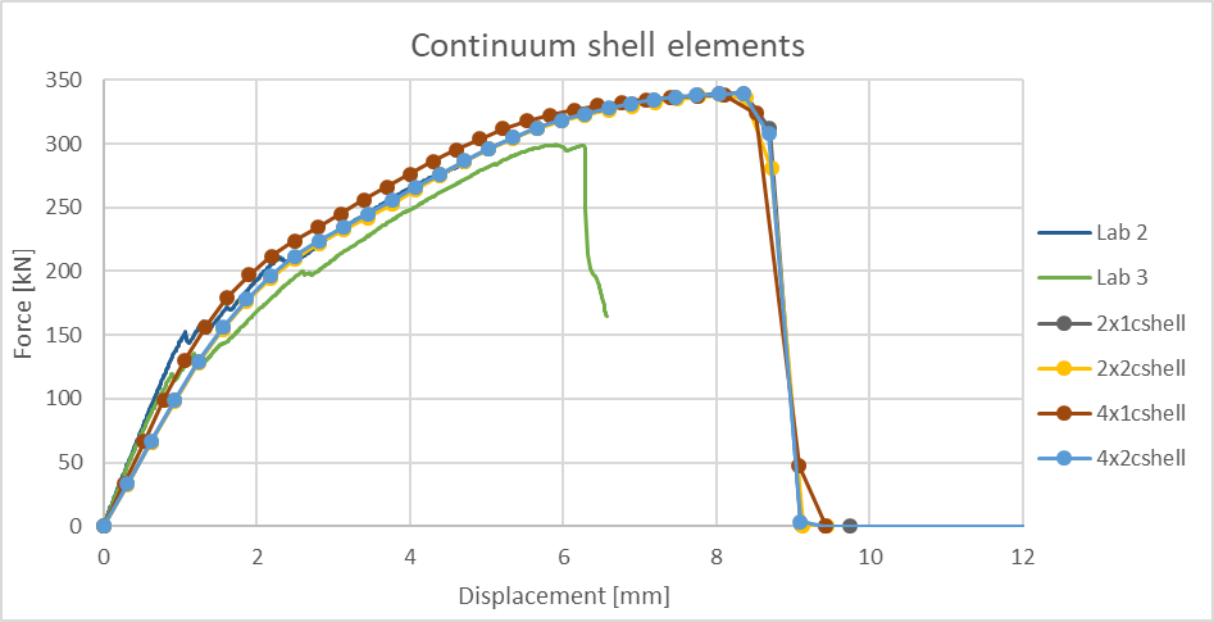

Figure 4.9: Four layers of FRP, using continuum shell elements

The force-displacement curves of the models with solid elements can be seen in figure 4.10. All four meshes give approximately the same results when solid elements are used. The initial stiffness is lower than that of the samples and has one distinct moment of stiffness

degradation before the onset of final failure. After this degradation, the curves of the models coincide with the curve of one of the samples.

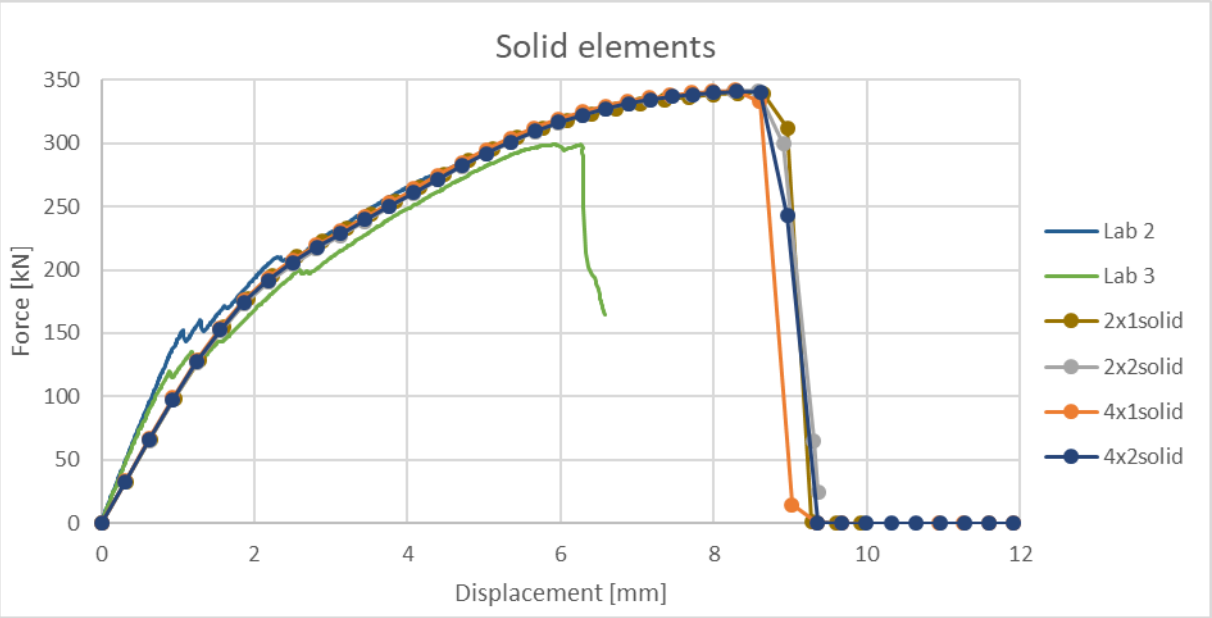

Figure 4.10: Four layers of FRP, using solid elements

In figure 4.11, a comparison is made between the models with solid elements and the models using continuum shell elements. Only the force-displacement curves of the 2x2 models are displayed, this is done to limit the number of curves is a single figure and both curves are representative for the other meshes as well. It is observed that the curves are very similar.

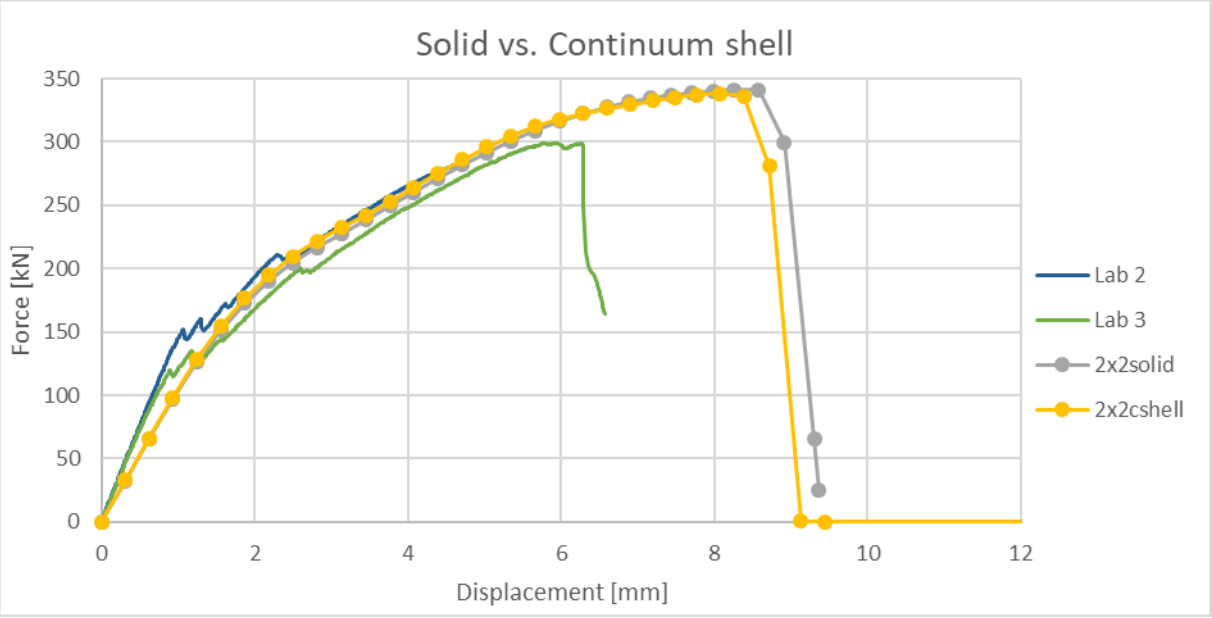

Figure 4.11: comparison solid vs continuum shell elements, four layers of FRP

4.2.1. EXPLICIT

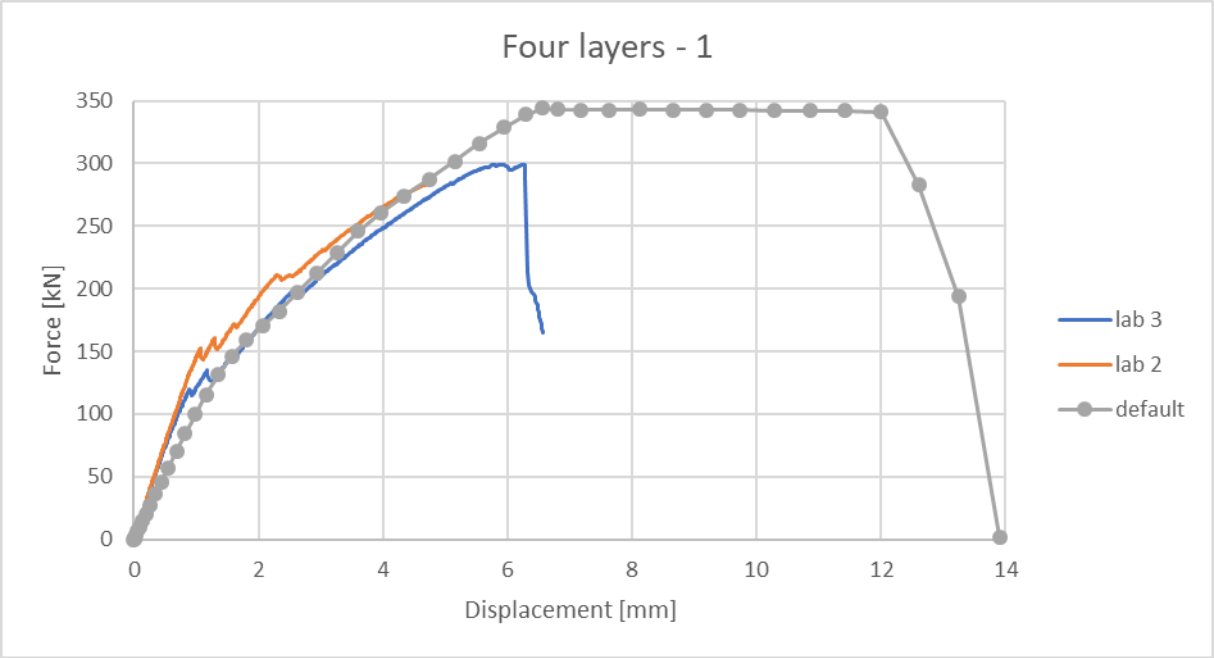

Figure 4.12: explicit model, four layers, a plateau is observed

In figure 4.12 the force-displacement curve of the first explicit model of the four-layer geometry is shown. What immediately draws attention is the plateau at a load of around 340 kN. After inspection of the output database, remarkable displacement fields were observed where the FRP touches the steel. These displacements are shown in figure 4.13, a zoomed view is included. The displacement of the elements looks like an hourglass mode of an 8-node brick element. This problem can solved by using stiffness or enhanced hourglass control. The results of this can be seen in figure 4.14. This is further elaborated in chapter 7.

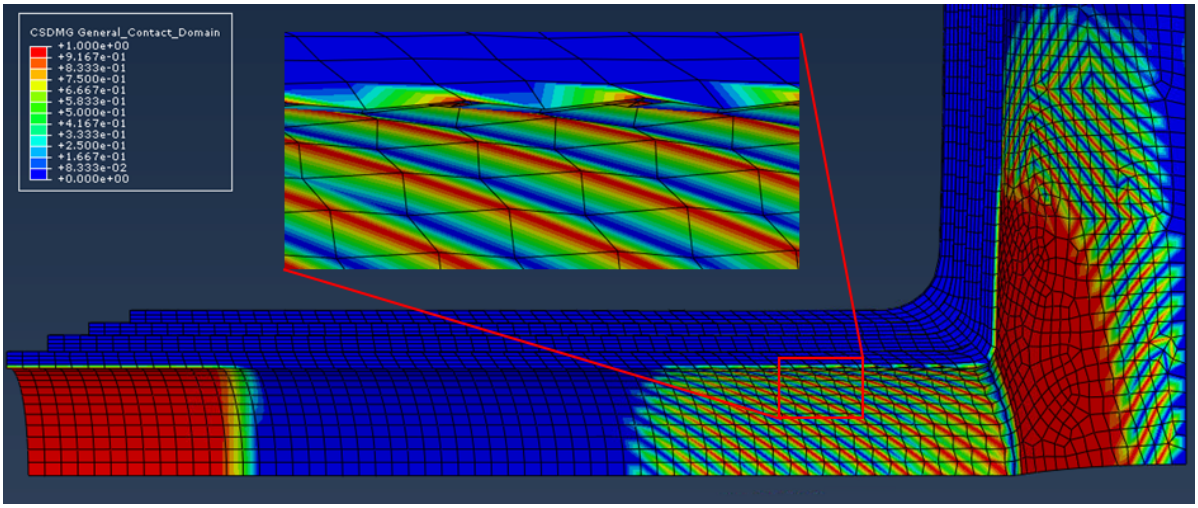

Figure 4.13: Hourglass mode on inside layer of FRP. The contour plot is for the damage parameter of the bond between steel and FRP

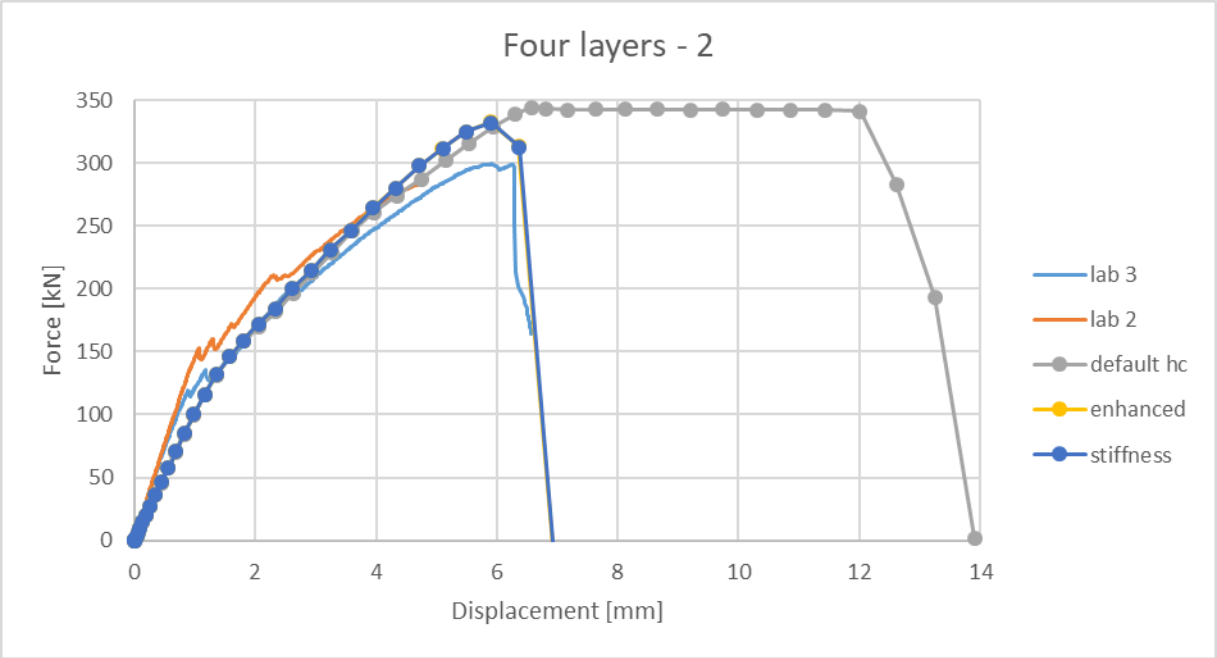

Figure 4.14: Different methods of hourglass control

4.2.2. COMPARISON IMPLICIT AND EXPLICIT

A comparison between implicit and explicit models of the four-layer geometry is shown in figure 4.15. It is observed that the initial stiffness of the models are the same. The explicit model experiences stiffness degradation earlier than the implicit models, but retains more stiffness after degradation. Final failure happens at a similar load level, but at significantly less displacement in the explicit model. The ultimate displacement of the explicit model is similar to that observed in the lab test and the ultimate load is overestimated.

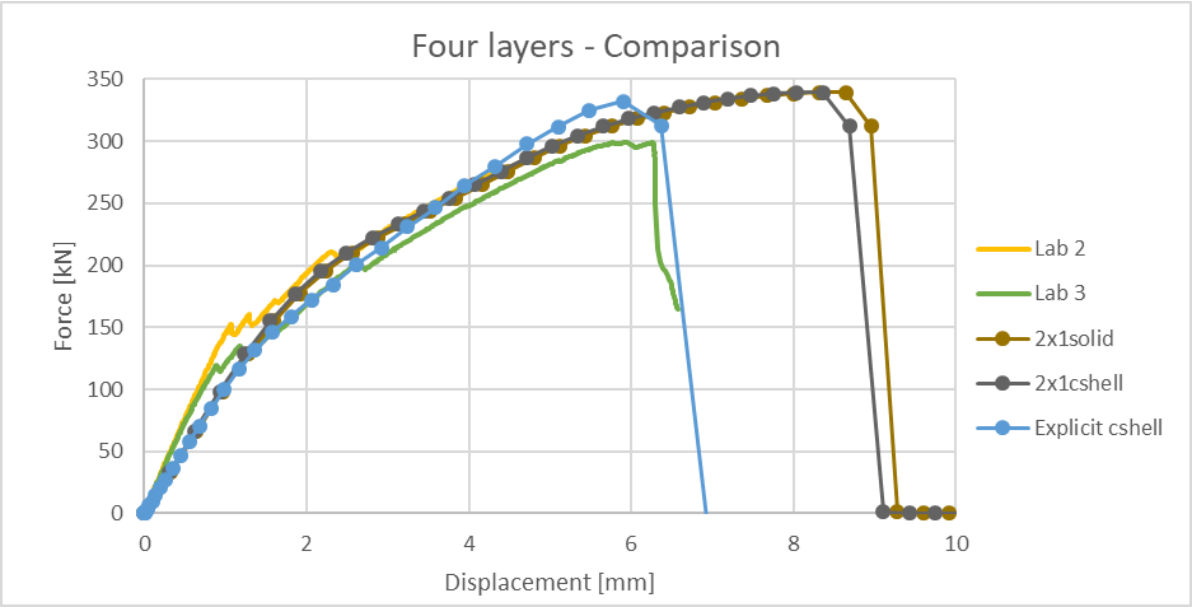

Figure 4.15: Comparison of implicit and explicit models of the four layer geometry

4.2.3. CONCLUSIONS

No significant differences were found between using solid or continuum shell elements in Abaqus/Standard. Various mesh densities were tried on this geometries, all gave the same results. Again, the model run in Abaqus/Explicit has a lower failure load and a lower displacement at failure than the model run in Abaqus/Standard.

4.3. FOURTEEN LAYERS OF FRP

Figure 4.16 displays the geometry on which the 14-layer models are based. Each layer has a thickness of 1mm and from the inside to the outside, the length of the layers decreases to from a tapered end. The layers are connected to each other using a CZM, with which it is possible to model delamination.

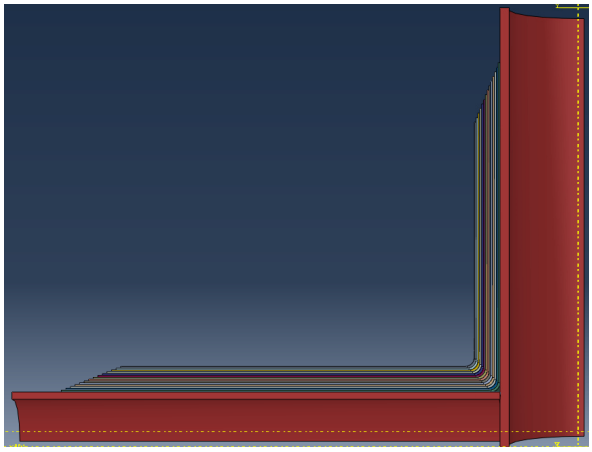

Figure 4.16: 14-layer geometry

4.3.1. IMPLICIT

In figure 4.17, the force-displacement curves of the models with 14 layers are shown. It is observed that the initial stiffness of the models is lower than the stiffness of the samples. When stiffness degradation occurs, the curves from the models are similar to the curves of one of the samples. Both the strength and the displacement at failure are overestimated by the models. It is also observed that the model with solid elements suffers from convergences issues, the model aborts.

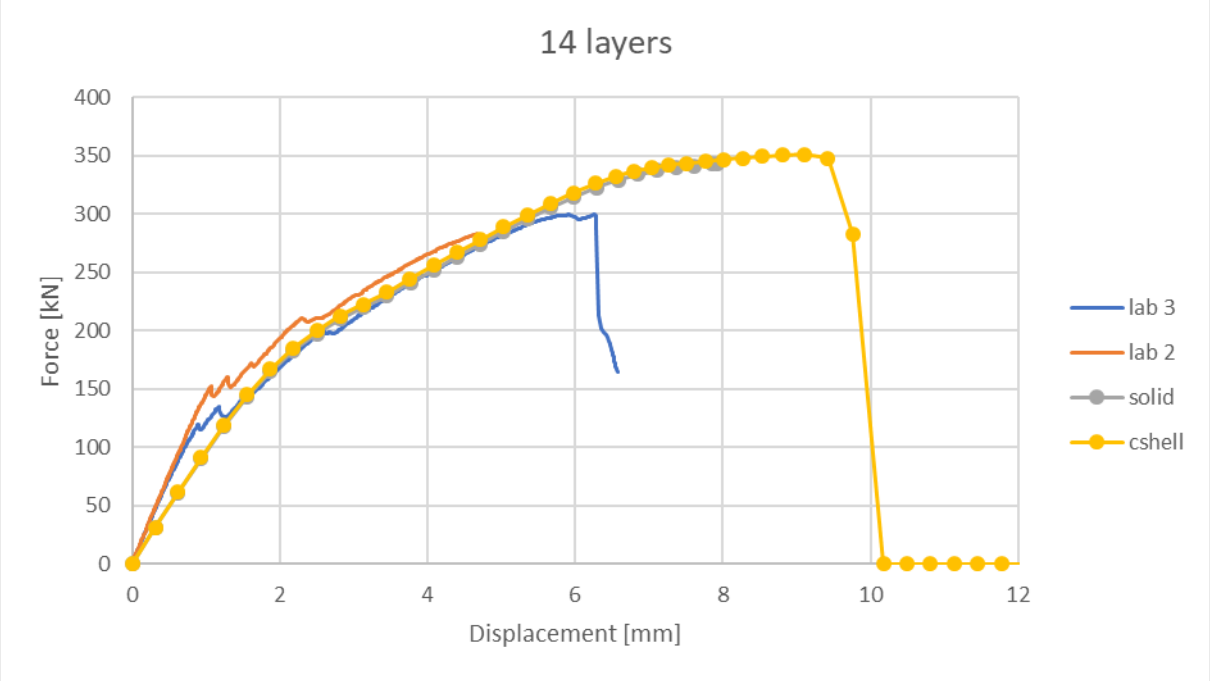

Figure 4.17: Implicit model, 14 layers of FRP. Force-displacement curves are shown for both solid elements and continuum shell elements

4.3.2. EXPLICIT

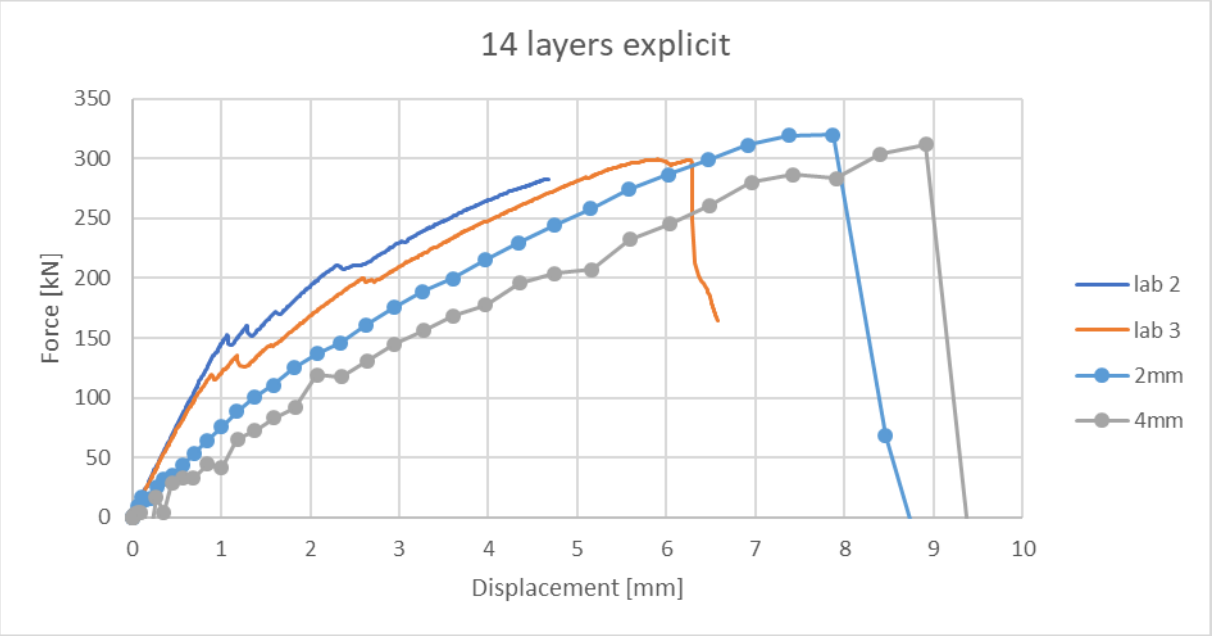

Figure 4.18: First 14-layer explicit models, with a 2mm mesh and a 4 mm mesh.

In figure 4.18 the force-displacement curves of the first 14-layer explicit models are shown. One model has an element size of approximately 2mm, the other has an element size of approximately 4mm. It draws attention that the curve of the model with 4mm elements has a lot of kinks in it. After inspection of the output database, it seems like this is caused by hourglassing of the elements. More information on how this hourglassing problem is solved, can be found in chapter 7.

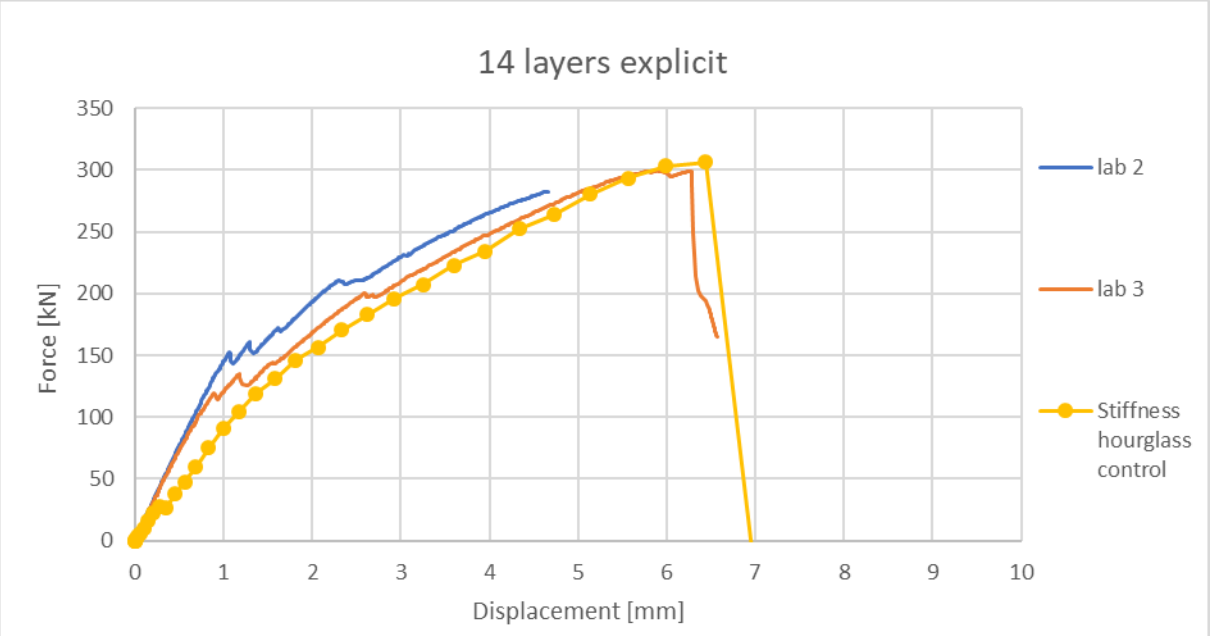

Figure 4.19: 14 layer explicit model

Figure 4.19 shows the force-displacement curve of the fourteen layer explicit model with improved hourglassing behaviour. The hourglass modes have not completely been resolved, however, useful observations can still be made. The ultimate load and displacement are approximated rather well. The initial stiffness up to the kink is slightly lower than the that found in the experiments and a stiffness degradation is present at a similar load level as has been found in the experiments.

4.3.3. TIME SENSITIVITY ANALYSIS

In order to find an appropriate step time for the analysis, a time sensitivity analysis has been done. The step time has been varied from 10 to 1000 seconds.

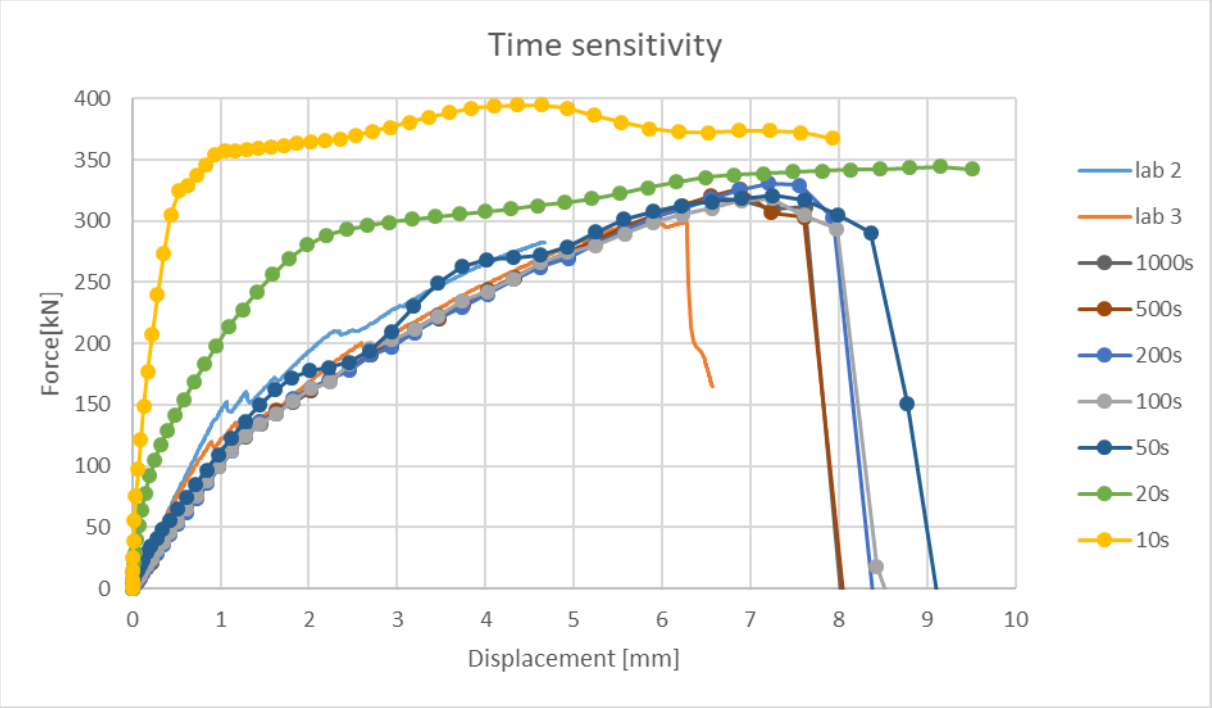

Figure 4.20: Time sensitivity analysis 14-layer model

In figure 4.20 the results of the time sensitivity analysis are shown. Step times from 10 seconds to 1000 seconds are included. It is observed that the models with step times of 10 and 20 seconds have a very high initial stiffness, this is most caused by the high loading speed and the inertia of the model. Step times of 10 and 20 seconds are too short to give any useful results for this model. Considering the model with a step time of 50 seconds, it is observed that the stiffness is initially quite high but decreases almost immediately. This is more easily visible in figure 4.21, where a zoomed view of figure 4.20 is offered. Starting at 2mm displacement, the curve starts to undulate, possibly as a result of a too high loading speed. A step time of 50 seconds is therefore too short to give any useful results for this model The curves of the models with step times of 100, 200, 500 and 1000 seconds approximately coincide up to 6 mm displacement. Figure 4.21 is used to inspect the initial stiffnesses of these models.

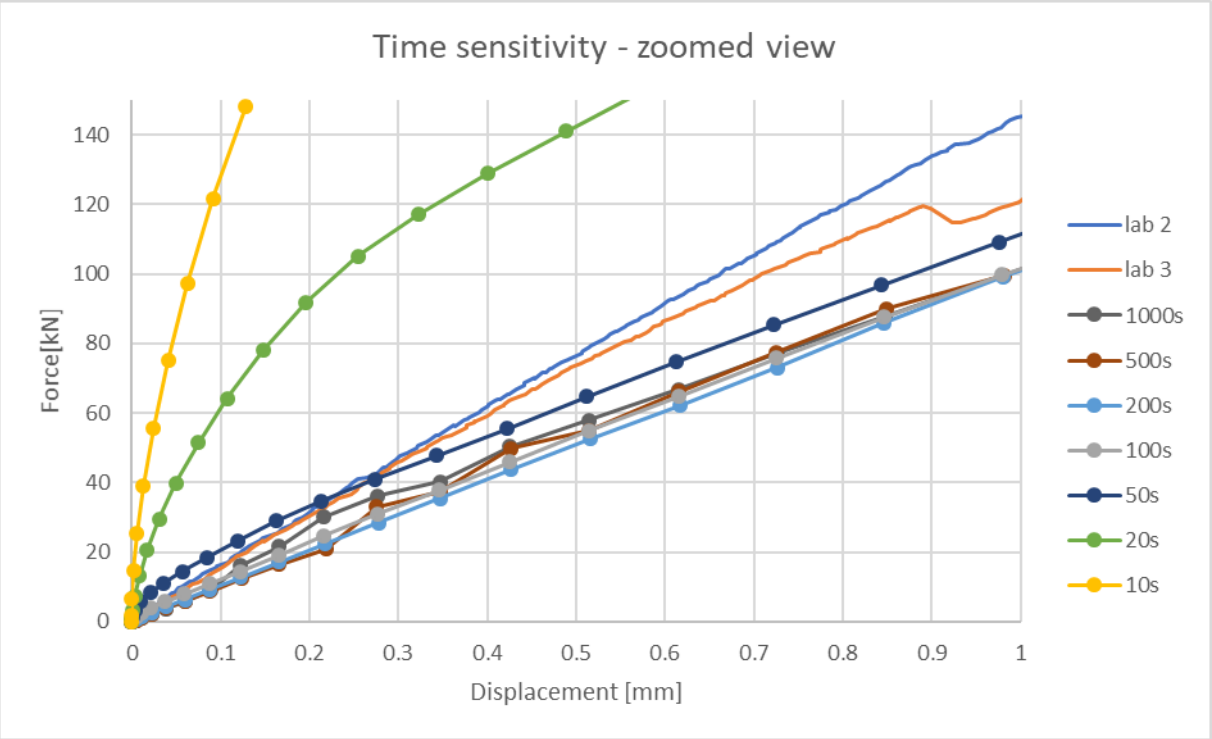

Figure 4.21: Zoomed view of the results of the time sensitivity analysis near the origin

It is observed that for a step time of 100 seconds some minor inertia effects occur at the start of loading. For a step time of 200 seconds, these inertia effects are visible anymore, the stiffness remains linear for the first millimetre of displacement. The model with a step time of 500s starts off in a similar manner as the model with 200 seconds, but after 0.2mm displacement a wobble is observed. This wobble stops at 0.5mm displacement and from 1 mm displacement onward the curve follows the curve from the model with 200 seconds step time. A similar wobble is observed in the model with a step time of 1000 seconds, it starts at 0.1mm displacement and stops after 0.5mm displacement. These wobbles are caused by hourglassing elements. Further differences are seen around the moment of failure, a zoomed view of this is given in figure 4.22.

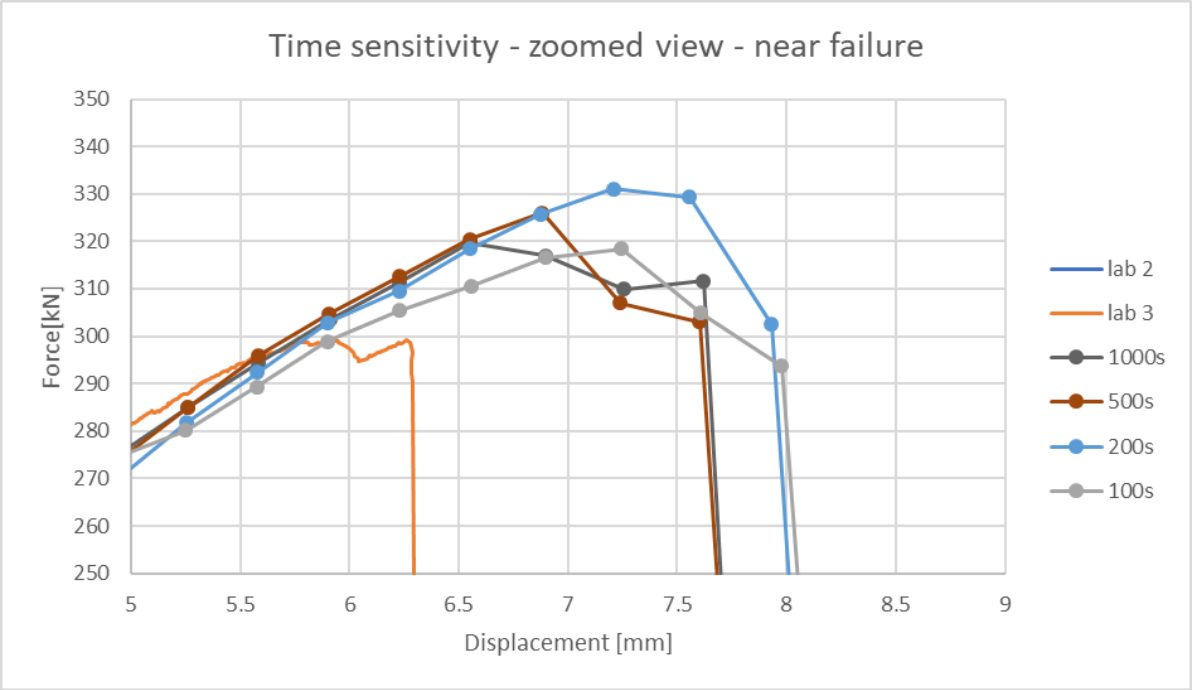

Figure 4.22: Zoomed view of the results of the time sensitivity analysis around the moment of failure

In figure 4.22 it is observed that the behaviour around the moment of failure shows some differences between the models. The models with 200, 500 and 100 seconds follow the same path, while the model with 100 seconds takes a slightly lower load at the same displacement.

From this time sensitivity study it can be concluded that for modelling the elastic behaviour of these joints a total step time of 200 seconds suffices. However, it must be noted that this might need to be increased to be able to accurately model failure of the joints.

4.3.4. COMPARISON IMPLICIT EXPLICIT

A comparison between implicit and explicit models of the 14-layer geometry is shown in figure 4.23. It is observed that the initial stiffness of the models are the same. The gradual stiffness degradation starts earlier in the explicit models. Final failure happens at a lower load level and at significantly less displacement in the explicit model. Both the displacement at failure and the ultimate load are approximated accurately by the explicit model. However, the results of the explicit model starting at a load level of approximately 25 kN are influenced by hourglassing. Furthermore, it must be noted that running these models in Abaqus/Standard is computationally very expensive, the time needed to run these models is in exceedance of one week while Abaqus/Explicit needs only around five hours.

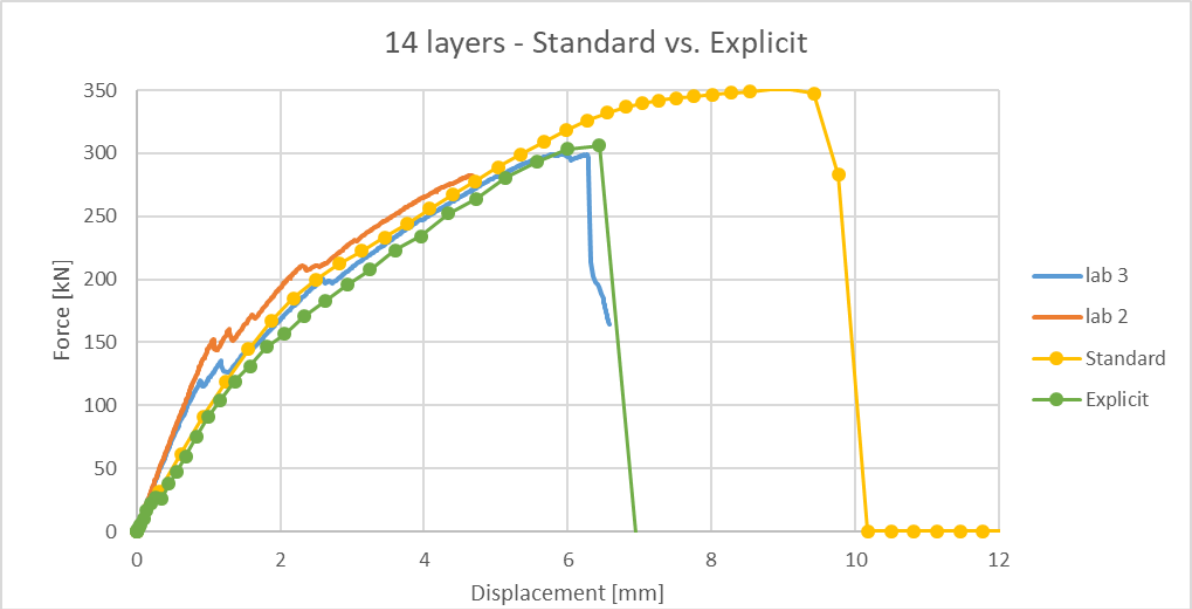

Figure 4.23: Comparison of implicit and explicit models of the fourteen layer geometry

4.4. OVERVIEW

In figure 4.24 all implicit models are compared, for each geometry, a force-displacement curve of a representative model is shown. A trend is observed, when the number of layers of FRP increases, the stiffness of the model decreases. The most probable cause for this is that the stiffness of the interaction that defines the inter-ply behaviour is too low. A good option to solve this problem, while still being able to model delamination is to use the default stiffness option for the interaction that governs the inter-ply behaviour.

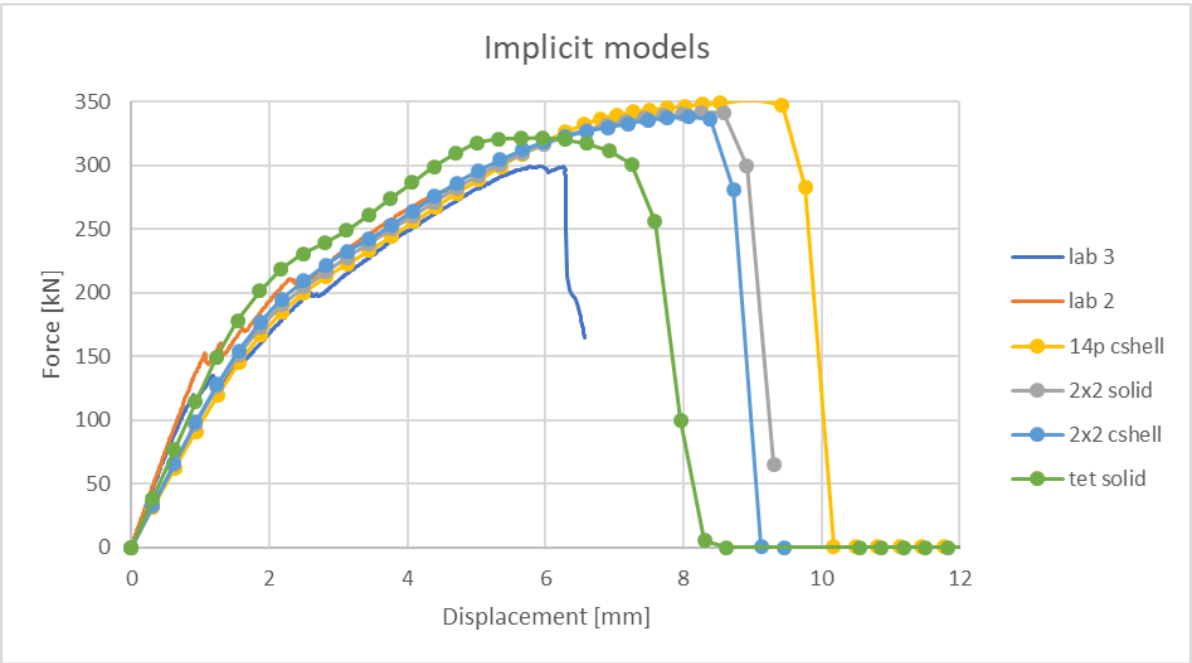

Figure 4.24: Comparison of implicit models

In figure 4.25 the explicit models are compared. The same trend regarding the stiffness of the models is observed as in figure 4.24.

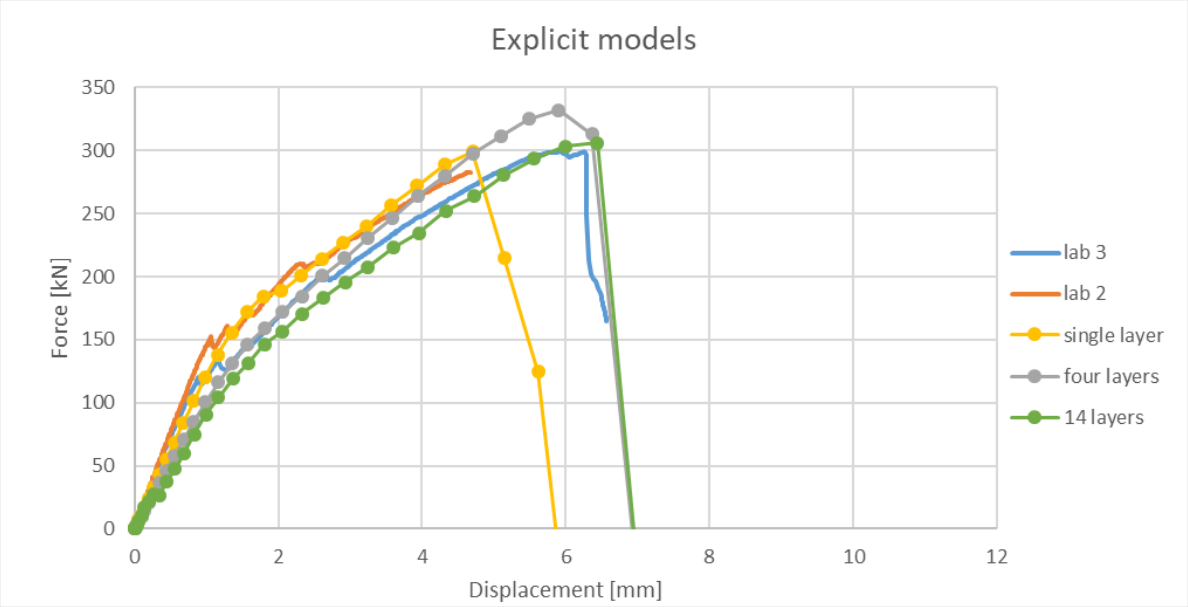

Figure 4.25: Comparison of explicit models

Observing figure 4.24 and 4.25, it seems that the explicit models make a better approximation than the implicit models. Furthermore, Abaqus/Explicit is computationally a lot more efficient for these models. Therefore, the models in the rest of this thesis will all be explicit.

As mentioned in section 3.4 it is not possible to model a composite layup with solid elements in Abaqus/Explicit. No difference was found in the implicit models between using solid element and continuum shell elements. Therefore continuum shell elements will be used in the remainder of the models in this thesis.

5

DEBONDING

In this chapter, improving the Cohesive Zone Model (CZM) for the debonding failure mode will be the main point of focus. The CZM needs improvement, because the failure mode of the models of the axial joint differ from the failure modes observed in the lab in the axial joints. In the lab, it was observed that final failure of the samples was induced by yielding of the steel section. The steel section contracts when it yields and this contraction causes the debonding. The models of the axial joints fail by shear failure of the interface between the steel and FRP, and not by normal failure caused by contraction of the steel cross-section. Only the axial geometry will be considered in this chapter, in attempt to isolate the debonding failure. First, a more simple geometry containing only a single layer of FRP will be modelled, later on, more layers will be added. At the end of the chapter a sensitivity study is included.

5.1. SINGLE LAYER OF FRP

In figure 5.1 the geometry containing a single layer of FRP is displayed. In this model, the FRP is assumed to be linear elastic and isotropic. Only half of the geometry is shown, no use of symmetry is made in the longitudinal direction. In both transverse directions, symmetry boundary conditions have been applied.

Figure 5.1: Geometry of Axial models, with a single layer of FRP

The original model that served as a starting point is an implicit model. An explicit model was made using the same parameters for the strengths and fracture energies to describe the debonding behaviour. These values can be found in table 5.1.

Direction	Normal	Shear-1	Shear-2
Strength [MPa]	11	22	22
Fracture Energy [N/mm]	0.5	4.8	4.8
Stiffness [MPa/mm]	500	500	500

Table 5.1: Strengths and fracture energies used in the original model, a starting point.

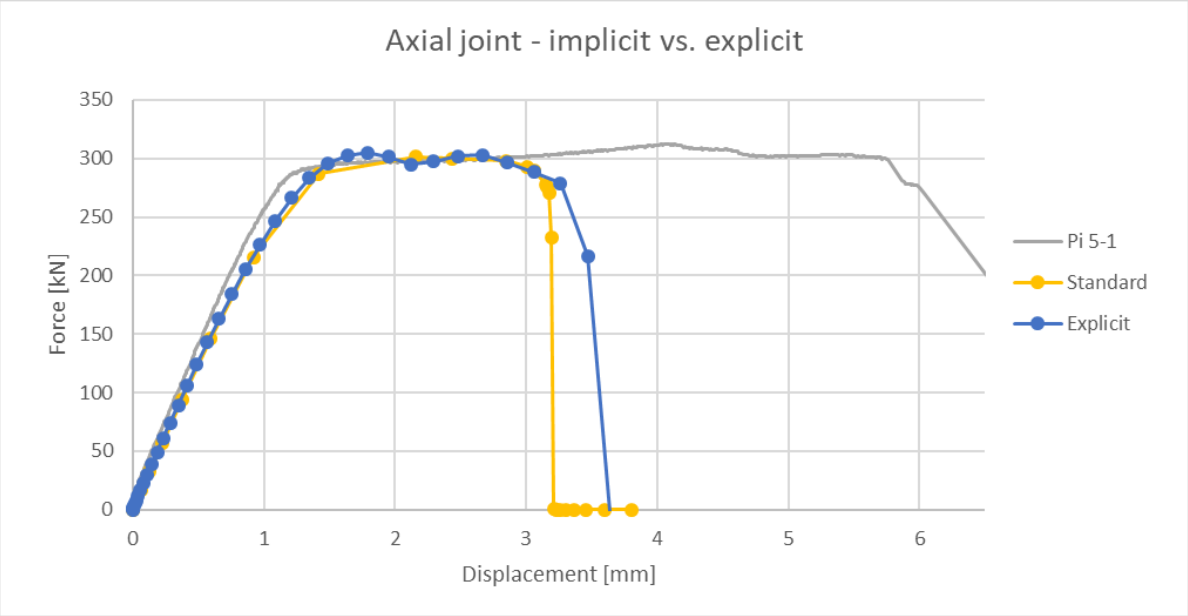

Figure 5.2: Comparison of implicit and explicit results with the strength and fracture energy from the original models

In figure 5.2 the force-displacement curves of the original implicit model, the explicit model and a sample from the lab are compared. Very little differences are observed between the implicit model and the explicit model. The stiffness of both models is the same and the ultimate load is very similar. The curve from the explicit model shows an undulation where the curve from the implicit model shows a plateau. This undulation is caused by the step time of the explicit model being too short. Using a larger step time will result in a plateau instead of an undulation. This will be shown later in this chapter.
The initial stiffness of the models is the same as the initial stiffness of the sample and the ultimate load of the models is very similar to that of the sample. However, the displacement at failure is much lower in the models, the sample shows twice the ductility as the models. It is observed that at around 125 kN, the models start to loose some stiffness. This load level corresponds to the load level at which debonding damage starts to propagate from the centre of the joint towards the ends. This is shown in figure 5.3.

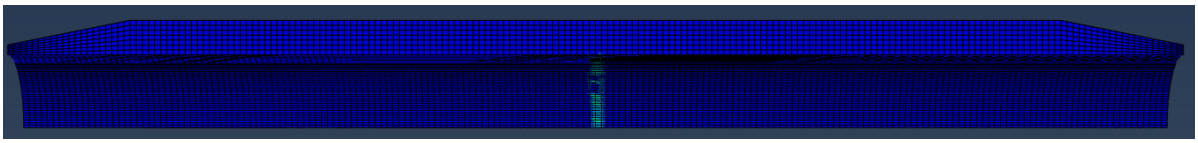

(a) Debonding damage at 124 kN of load

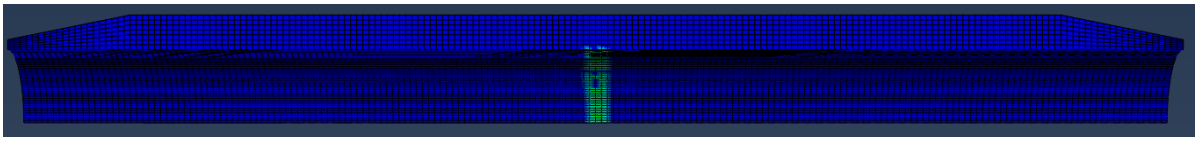

(b) Debonding damage at 142 kN of load

Figure 5.3: Initiation of debonding damage occurs at around 125 kN of load

The force-displacement curve from the sample does not have this loss of stiffness observed in figure 5.2. This suggest the bond strength used in the models is lower than the actual bond strength. Therefore the bond strength was increased. The fracture energy was scaled with the same factor squared to keep the same ductility of the bond. The results of the models with increased strength and fracture energy are shown in figure 5.4.

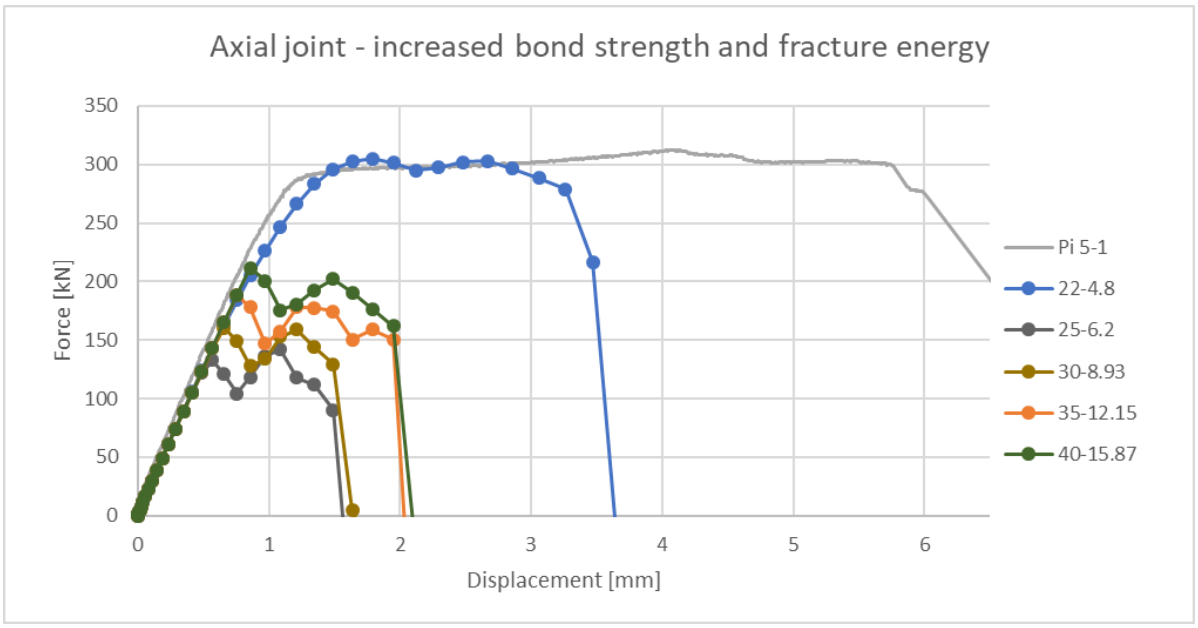

Figure 5.4: Increasing the bond strength above 22 MPa leads to brittle failure of the bond, regardless of the fracture energy

Unexpectedly, the strengths of the models with a higher bond strength are lower than the strength of the original explicit model. It is observed that for bond shear strengths higher than 22 MPa, the failure of the bond becomes rather brittle and happens at a lower load than for lower bond shear strengths. This is opposed to the expectation that increasing the bond shear strength increases the strength of the model. Figures 5.5 and 5.6 show that the first damage in the model with a bond shear strength of 25 MPa occurs slightly later than in the model with a bond shear strength of 22 MPa, but that in the model with higher bond shear strength the damage evolves a lot faster than in the model with lower bond shear strength.

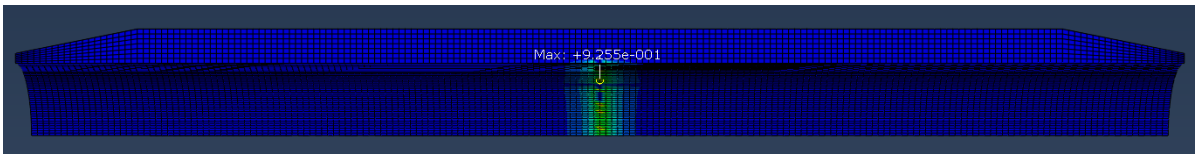

(a) Damage initiation criterion for the 22-4.8 model at 0.286 mm displacement

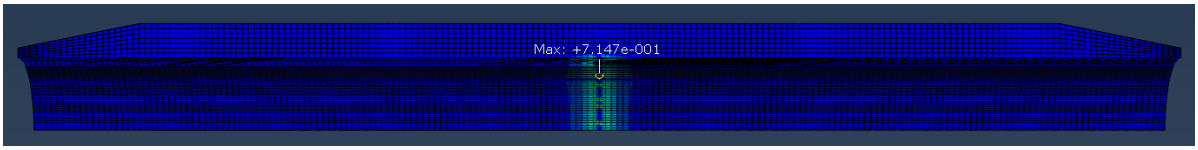

(b) Damage initiation criterion for the 25-6.2 model at 0.286 mm displacement

Figure 5.5: Difference in damage initiation between 22 MPa strength and 25 MPa

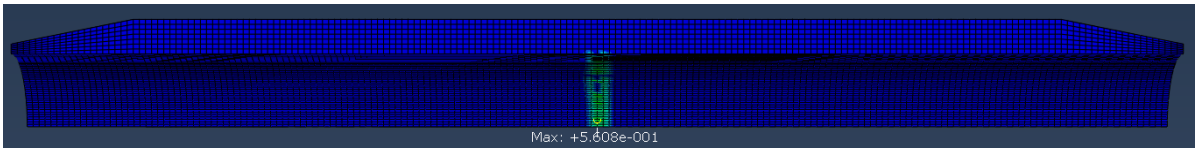

(a) Debonding damage for the 22-4.8 model at 0.568 mm displacement

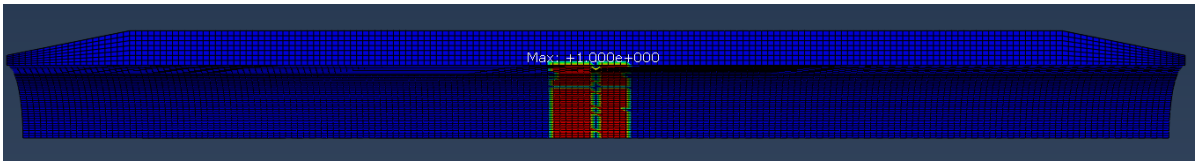

(b) Debonding damage for the 25-6.2 model at 0.568 mm displacement

Figure 5.6: Difference in damage evolution between 22 MPa strength and 25 MPa

Comparing figure 5.5a and figure 5.5b it is observed that in the 22-4.8 model, the damage initiation criterion has a higher value in a larger region than in the 25-6.2 model. This is as expected since the strength of the 25-6.2 model is higher. Figure 5.6 shows the difference in damage evolution between the model with lower bond shear strength and higher bond shear strength. It shows that when the bond shear strength is 22 MPa, the damage variable gradually increases from zero to one, while for higher bond shear strengths, the damage increases from zero to one instantly. The damage in the 25-6.2 model has fully evolved and has started to propagate towards the ends of the joints while the damage in the 22-4.8 model has not fully evolved and has not started to propagate. This is the reason for the lower strength and ductility of the models with a higher bond strength than 22 MPa.

Some research has been done into the influence of the fracture energy on the behaviour of the axial joint in tension. The results of the research is shown in figure 5.7. It is observed that increasing the fracture energy increases the ultimate load and displacement.The increase in displacement is too large to be caused solely by the increase in fracture energy, a large part of this displacement is caused by yielding of the steel. This does explain the difference. Still, the slight loss of stiffness at a load level of 125 kN is present. This suggest that the bond strength needs to be increased.

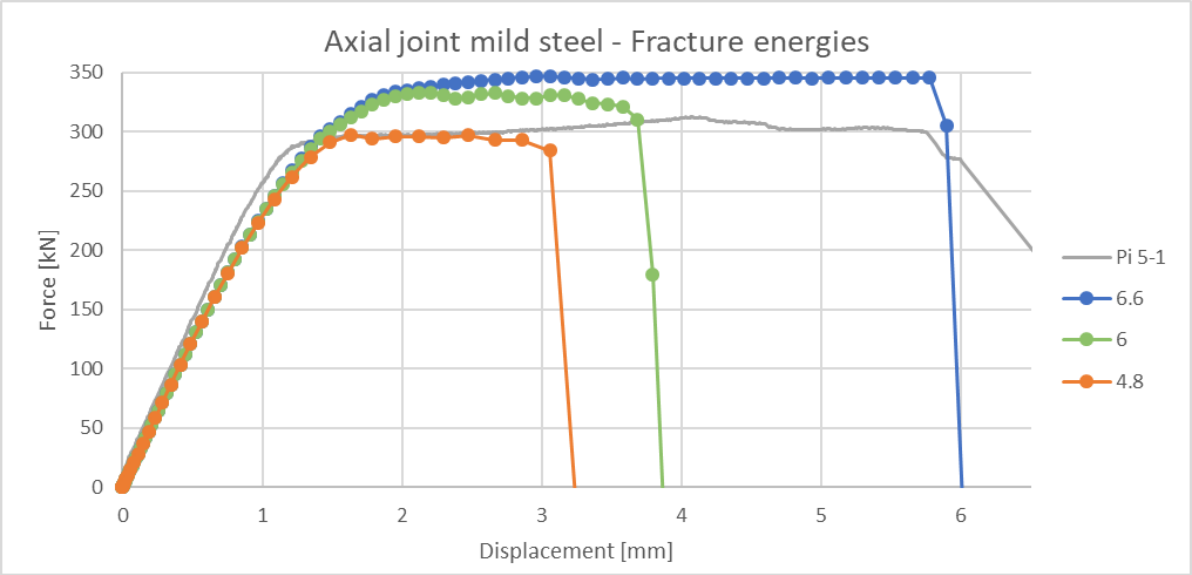

Figure 5.7: Results of increasing the fracture energy

The default stiffness option might make it possible to increase the bond strength. From figure 5.8 it appears that using the default stiffness option has very little effect on the force displacement curve.

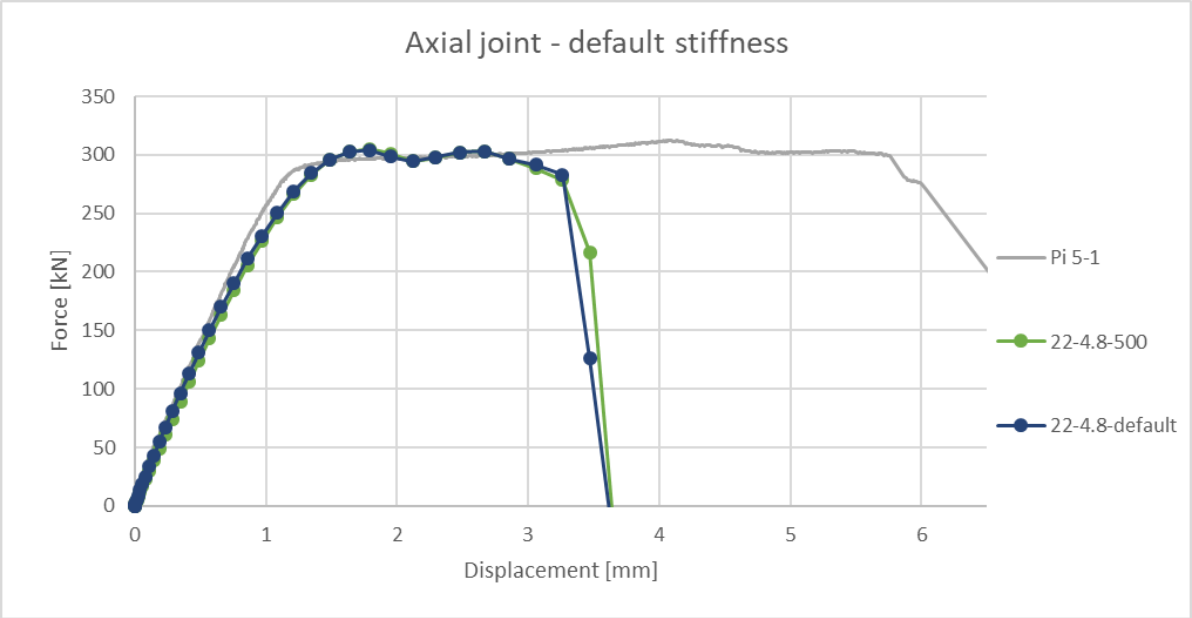

Figure 5.8: Force-displacement curve of model using the default stiffness option

Figures 5.9 and 5.10 provide some insight in what happens on the interface between steel and FRP. Comparing figure 5.9a and 5.9b it is observed that in the model with default stiffness, the damage initiation criterion is met at lower displacement than in the model with an interface stiffness of 500 MPa/mm. Since the strength is the same in both models, this suggests that the default stiffness is higher than 500 MPa/mm.

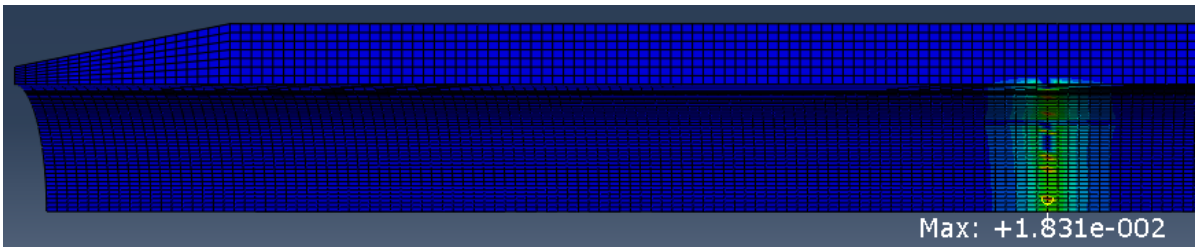

(a) Damage initiation criterion for the model with 500 MPa/mm stiffness at 0.040 mm displacement

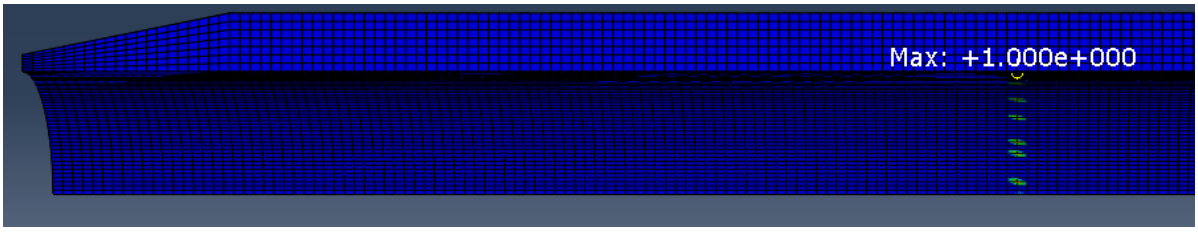

(b) Damage initiation criterion for the model with default stiffness at 0.040 mm displacement

Figure 5.9: Difference in damage initiation between 500 MPa/mm stiffness and default stiffness

Comparing figure 5.10a and 5.10b it is observed that in the model with default stiffness, the damage evolution and propagation starts faster than in the model with an interface stiffness of 500MPa/mm. The moment at which damage has fully evolved for the first time is the same in both models. This moment should be the same, since the bond strength and fracture energy are the same in the models. The speed at which the damage propagates is different between the two models, but the damage reached the end of the FRP at the same displacement in both models.

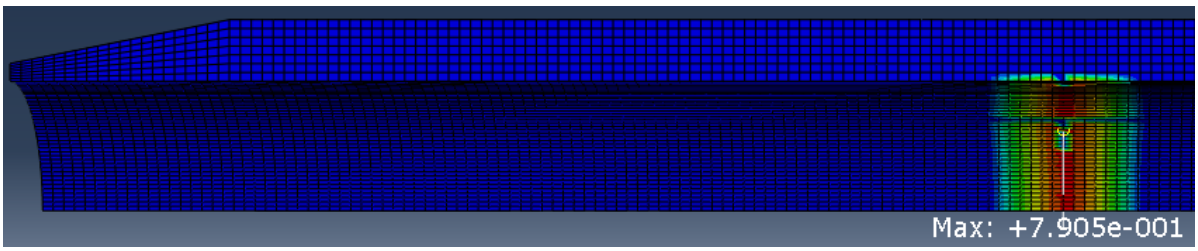

(a) Debonding damage for the model with 500 MPa/mm stiffness at 0.857 mm displacement

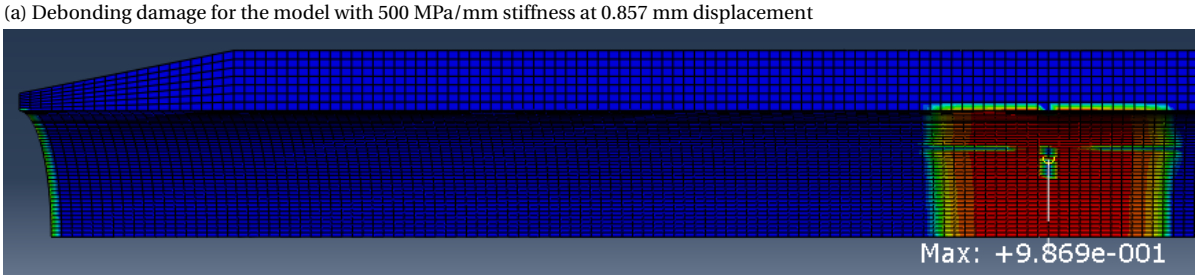

(b) Debonding damage for the model with default stiffness at 0.857 mm displacement

Figure 5.10: Difference in damage evolution between 500 MPa/mm stiffness and default stiffness

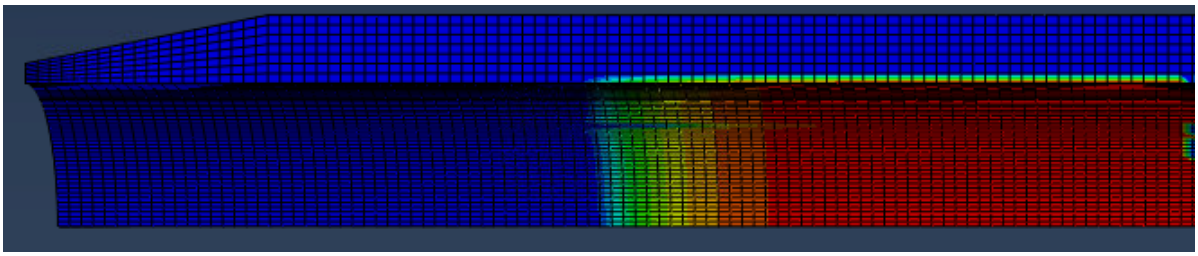

(a) Debonding damage for the model with 500 MPa/mm stiffness at 2.48 mm displacement

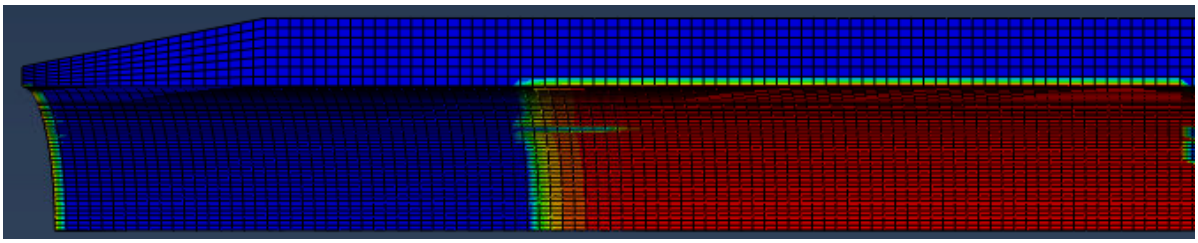

(b) Debonding damage for the model with default stiffness at 2.48 mm displacement

Figure 5.11: Difference in damage evolution between 500 MPa/mm stiffness and default stiffness

A similar comparison is made at a displacement of 2.48 mm. It is observed that contact damage has propagated further in the model with default stiffness.

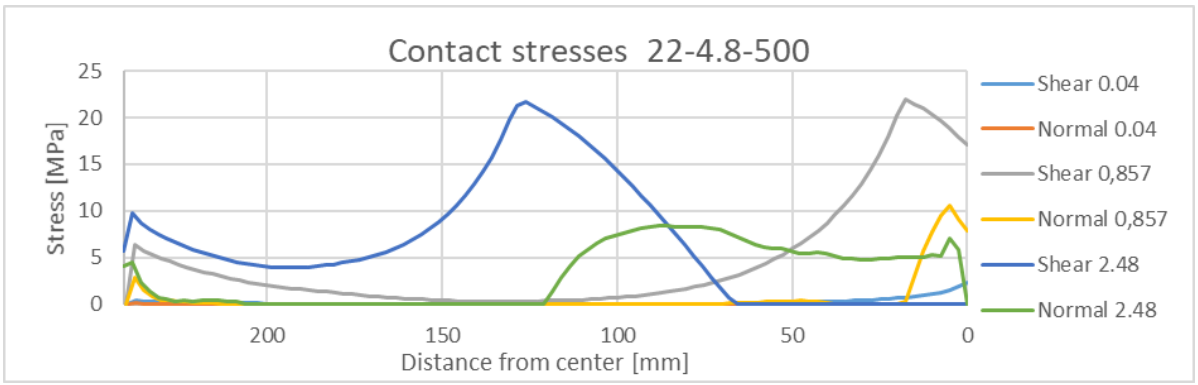

(a) 500 MPa/mm

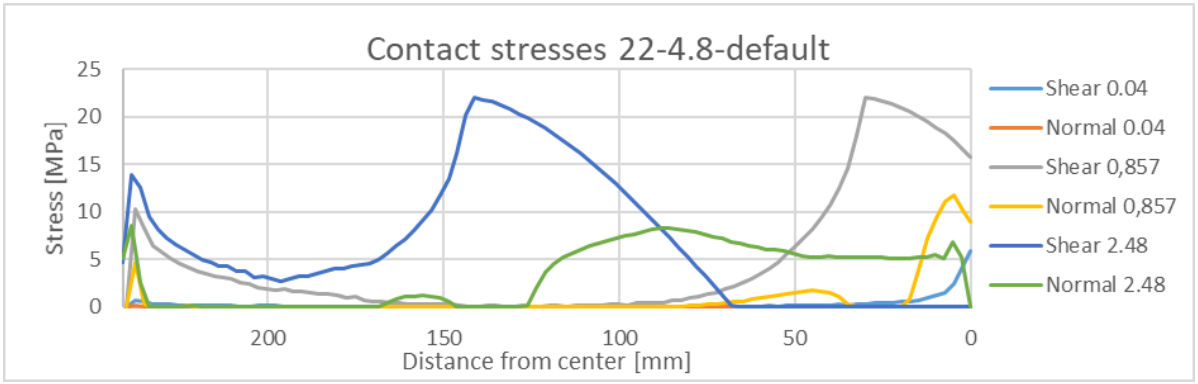

(b) Default stiffness

Figure 5.12: Absolute values of contact stresses on the steel-FRP interface for the 22-4.8 models at three different displacements.

Figure 5.12 shows the contact stresses in the models. In both models the shear strength

of the bond is reached at the peak and after this peak, the shear stresses decrease to zero in the areas where the damage is complete. Despite the peaks not being in the same location at 2.48 mm displacement, the locations when the shear stresses are zero, are the same. These locations should be the same, because only the stiffness of the bond has changed, the strength and fracture energy are the same, and with that, the displacement at which damage is complete is also the same. It is observed that after the peak in shear stress has passed, normal stresses start to develop in the interface. These normal stresses are compressive and caused by the fact that the steel in this part is not loaded anymore, but the FRP is. The FRP contracts due to the tensile loading, and the steel does not. This causes some compressive stresses in the interface.
From previous figures it can be concluded that the default stiffness option can be used for modelling the stiffness of the interface.

In order to keep the ductility of the bond the same, the fracture energy will be scaled quadractically with the bond strength. Figure 5.13 the result of increasing the strength and fracture energy is shown. The strength ranges from 22MPa to 50 MPa and the fracture energy from 4.8N/mm to 24.8N/mm. The models with a strength of 30MPa or higher and fracture energy of 8.93N/mm and higher do not fail before specified the displacement is reached and the load is overestimated significantly. The strength of the models does not increase significantly as the bond shear strength is increased, but the displacement at failure does. This suggests that the bond shear strength should be increased but that the fracture energy should not be scaled quadratically, it should be something around 4.8-6.2N/mm.

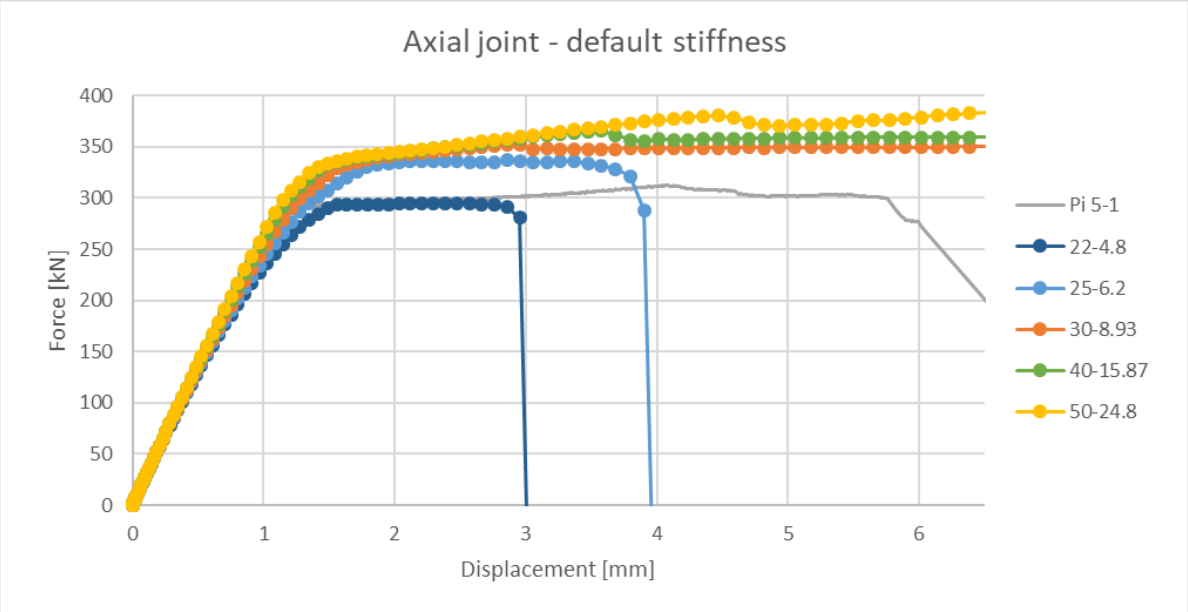

Figure 5.13: Strength and fracture energy have been scaled accordingly

Some lower values for the fracture energy were investigated, the results of this are shown in figure 5.14. Three different values for the fracture energy have been tried, they are compared to the results from the lab and the model that is the starting point. As observed earlier in this chapter, a lower fracture energy leads to a lower failure load and a lower displacement at failure. The observation is made that the model that has the same fracture energy

as the model that is the starting point, but with a higher strength, yields a similar force-displacement curve, but with the following difference; the moment of stiffness degradation is at a higher load and displacement.

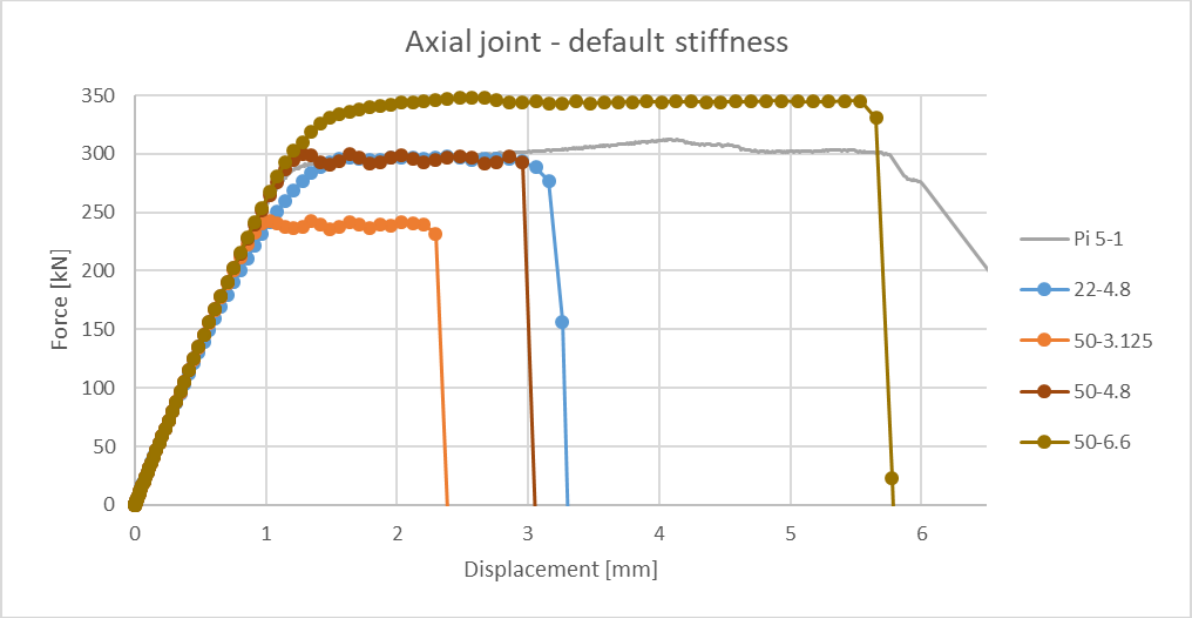

Figure 5.14: Changing fracture energies

5.2. 14 LAYERS OF FRP

Figure 5.15 shows the layer geometry of the axial joint, with symmetry conditions. This geometry will be used in the remainder of this section.

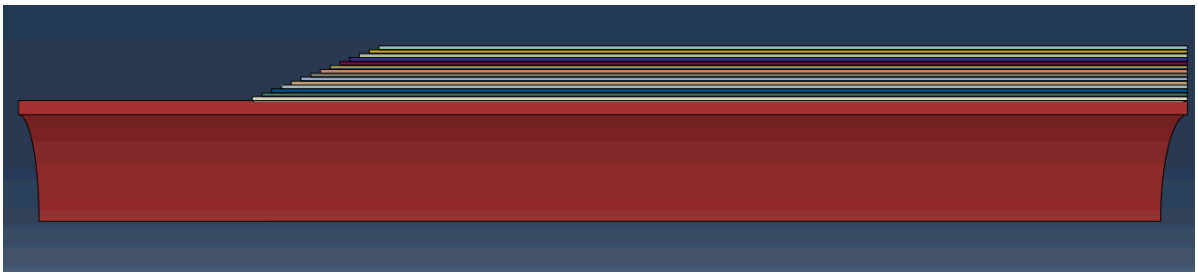

Figure 5.15: Geometry of Axial models, with 14 layers of FRP and symmetry conditions

The results of the first model with 14 layers is shown in figure 5.16. The yield plateau from the model is at a higher load level than than the yield plateau observed in test specimen. Combined with the fact that final failure is induced by yielding and contracting of the steel cross-section, the higher yield plateau suggest that the steel material model that was used has a higher yield strength than the steel used in the tests.

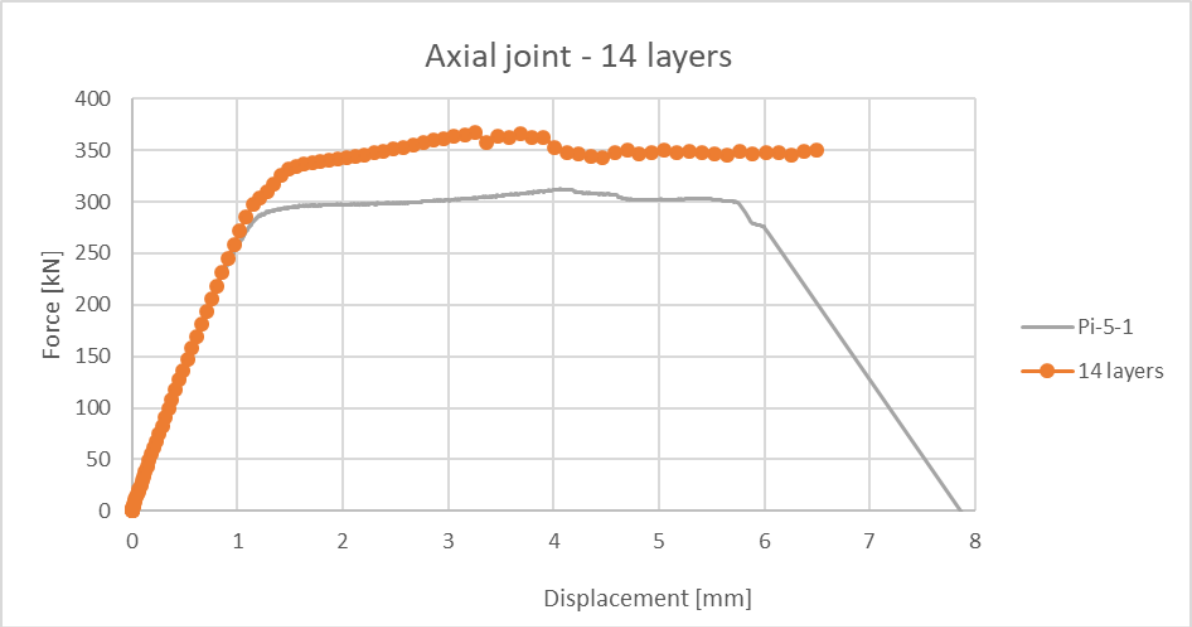

Figure 5.16: The yield plateau is a lot higher in the model, this is caused by the steel material model.

To solve this, the yield strengt of the steel material model has been lowered to have a better fit with the results from the lab. The force-displacement curve of the model with the new steel material model can be seen in figure 5.17. It is observed that the yield plateau now is at the same load level. Another thing that is observed, is the wobble at around 3.5mm displacement. This wobble looks like a damped vibration. This suggest that the loading speed may be to high. This can be solved by increasing the total time step.

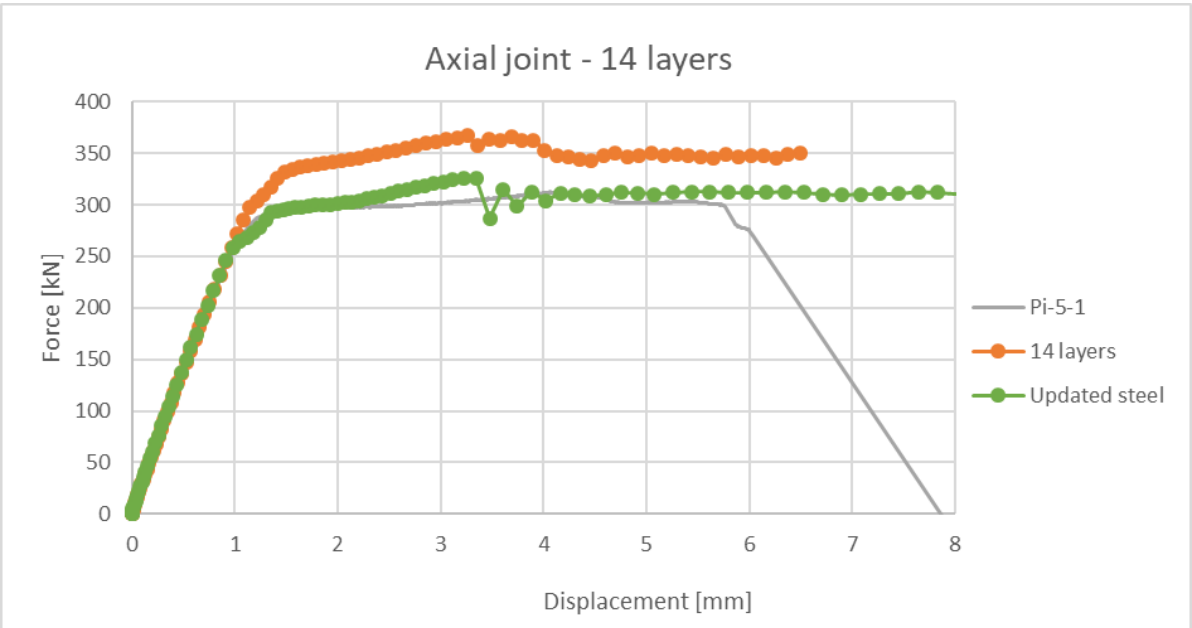

Figure 5.17: The update in steel material model causes the yield plateau to be at the same load level.

5.2.1. SENSITIVITY ANALYSIS

In order to find the smallest appropriate time step and largest appropriate time increment, a small sensitivity study has been carried out. First, the time step was varied, in figure 5.18, it can be seen that the smallest step time for which the force-displacement curves are converging, is 500s. Therefore the appropriate step time is 500 seconds.

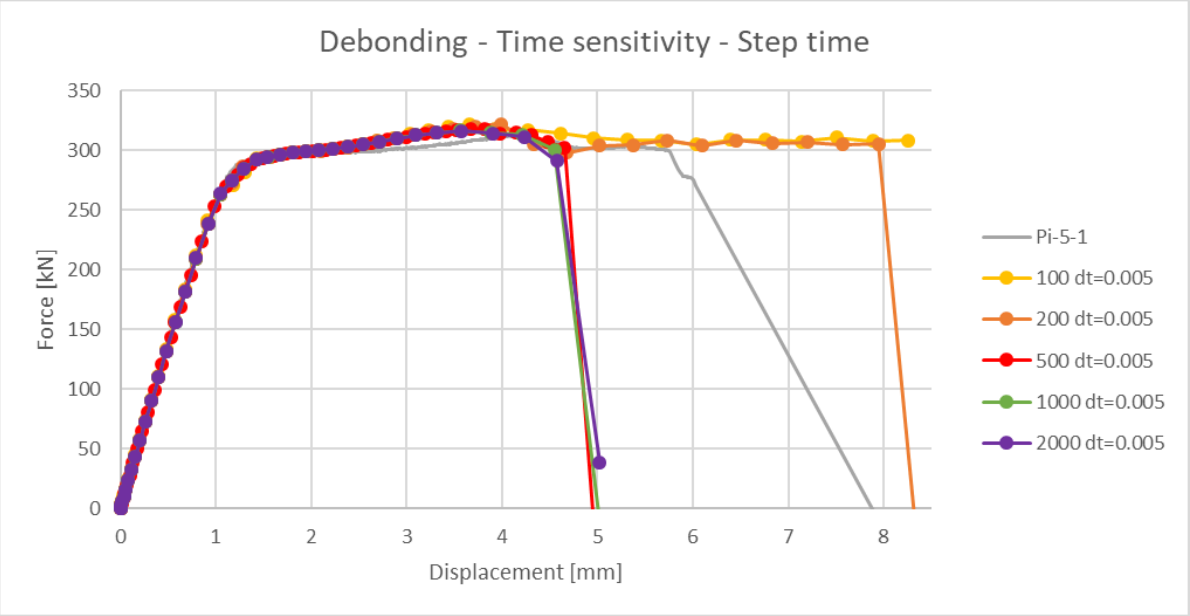

Figure 5.18: Step times have been varied, the curves converge starting at a step time of 500 seconds

A similar procedure was used for finding the appropriate increments size. In figure 5.19 the force-displacement curves are shown for models with an increment size varying from 0.05s to 0.001s. It is observed that for increments of 0.005s and smaller, the force-displacement curves converge. Therefore the appropriate increment size when using a step time of 500s, is 0.005s. Using this combination of step time and increment size causes the damped vibration at around 3.5mm displacement to disappear.

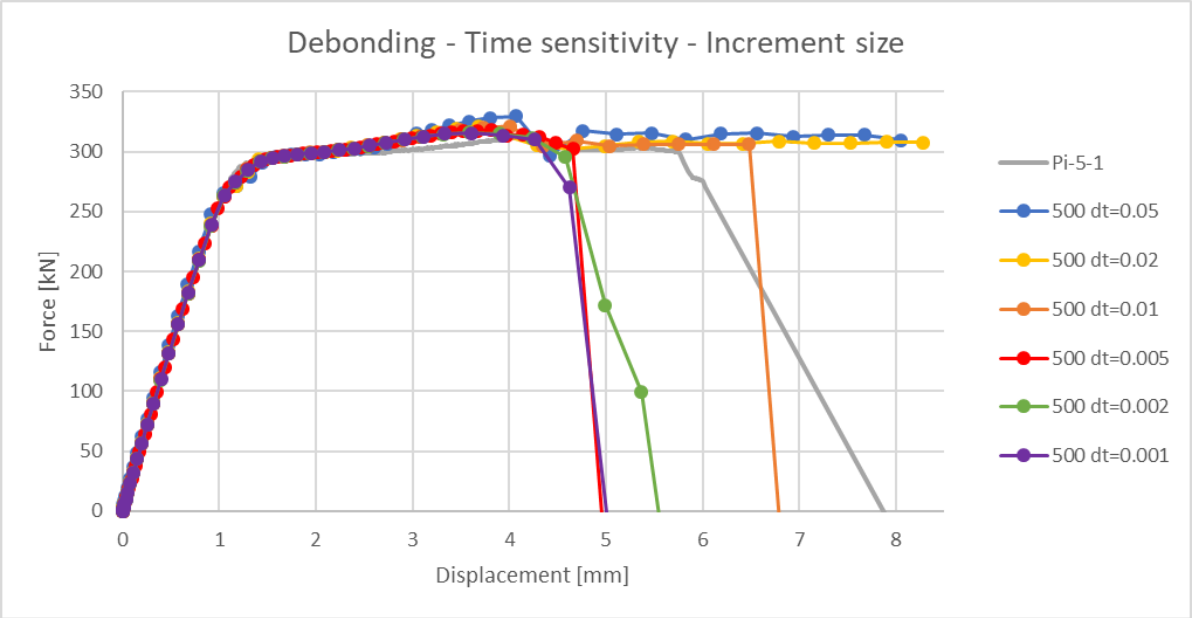

Figure 5.19: Varying increment times with a step time of 500 seconds

In figure 5.20 force-displacement curves are shown for models with a small variation in fracture energy. In the model with a fracture energy of 4.6 N/mm no failure is reached before the end of the analysis, while for a fracture energy of 4.5 N/mm failure occurs at around 4.7 mm displacement, this means that the models are very sensitive to changes in fracture energy, especially when the failure load is close to the strength of the steel section. For fracture energies lower than 4.5 N/mm, the difference is not as large as for fracture energy higher than 4.6 N/mm. Furthermore, it is observed that using the value of 50 MPa as the bond shear strength and 4.5 N/mm for the corresponding fracture energy, gives very good results.

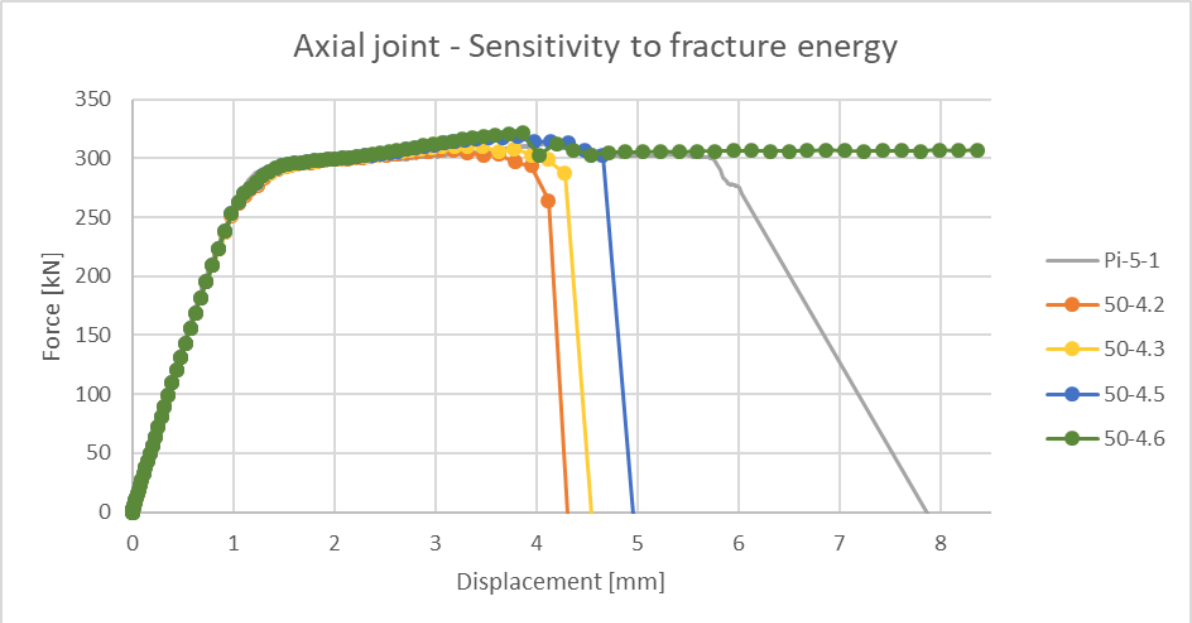

Figure 5.20: The model is very sensitive to changes in fracture energy of the bond.

In figure 5.21 the evolution of interface damage is shown for the models with a fracture energy of 4.5 N/mm and 4.6 N/mm. Figures 5.21a and 5.21c show contour plots of the interface damage at a displacement of 2.2mm. The contour plots look very similar, the only difference is that the damage in the model with a fracture energy of 4.5 N/mm has propagated slightly further from the root of the joint.

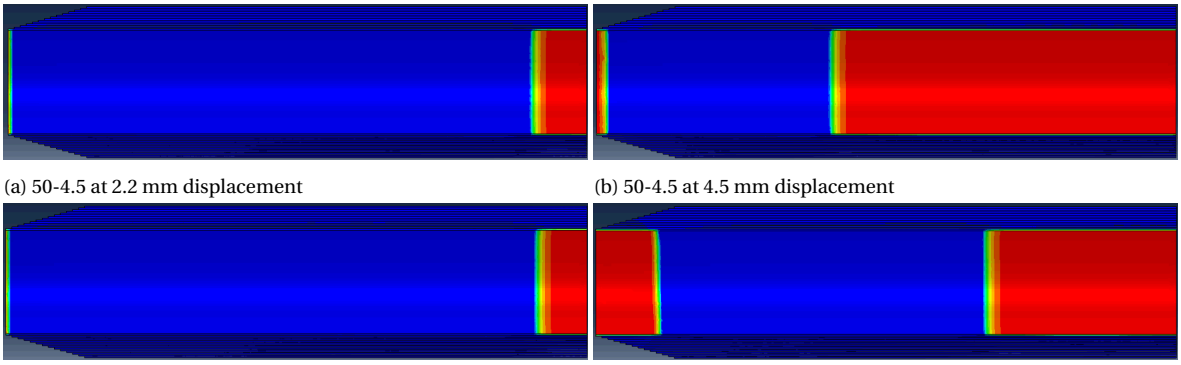

(a) 50-4.5 at 2.2 mm displacement

(b) 50-4.5 at 4.5 mm displacement

(c) 50-4.6 at 2.2 mm displacement

(d) 50-4.6 at 4.5 mm displacement

Figure 5.21: Interface damage evolution comparison between fracture energies of 4.5 N/mm and 4.6 N/mm. Damage propagating from the left side of the figures is caused by yielding of the steel

Figures 5.21b and 5.21d show the same comparison, but at a displacement of 4.5mm, just before failure of the model with a fracture energy of 4.5 N/mm. In the model with a fracture energy of 4.5 N/mm, the interface damage has propagated a lot further from the root of the joint than in the model with 4.6 N/mm fracture energy. From the end of the joint, the opposite is true. The interface damage that propagates from the end of the joint is caused by yielding of the steel section. This damage caused by yielding of the steel is present in both models.

(a) 50-4.5 at 4.5 mm displacement

(b) 50-4.6 at 4.5 mm displacement

Figure 5.22: Contour plot of plastic strain, the steel yields inside the FRP wrap.

The difference in yielding of the steel is displayed in figure 5.22. In both models the steel yields, but only in the model with 4.6 N/mm fracture energy, the yielding of the steel propagates towards the center of the joint. This difference is of this magnitude because the total

strength of the bond and the strength of the steel section are very close to each other. When the steel section is stronger, a failure mode as seen in figures 5.21a and 5.21b will occur, but when the total bond strength is higher, a failure mode as seen in figures 5.21a and 5.21d will occur. This also explains the sensitivity seen in figure 5.20.

Figure 5.23 shows the development of contact stresses in the 50-4.5 and 50-4.6 models. At a displacement of 2.2 mm, the normal and shear contact stresses in the models are very similar. This corresponds to the similarity of figures 5.21a and 5.21c. The locations of the peaks of the shear stress at 4.5 mm displacement correspond to the front of the damage propagation from the center to the end of the joint in figures 5.21b and 5.21d.In the 50-4.6 model, the peak shear stress at 4.5mm displacement is lower than the shear strength of the bond. This suggest that the damage near this peak is not propagating. This is confirmed in figure 5.21d, where all damage propagation is from the end to the center and is caused by yielding of the steel. This propagation also seen in figure 5.23b, the contact stresses in the 50-4.6 model at a displacement of 4.5 mm are zero at locations further than 220 mm from center.

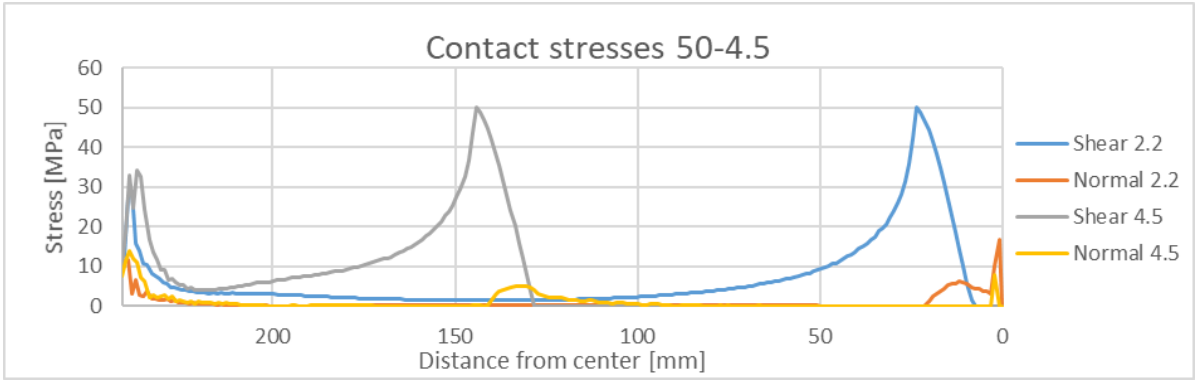

(a) 50-4.5

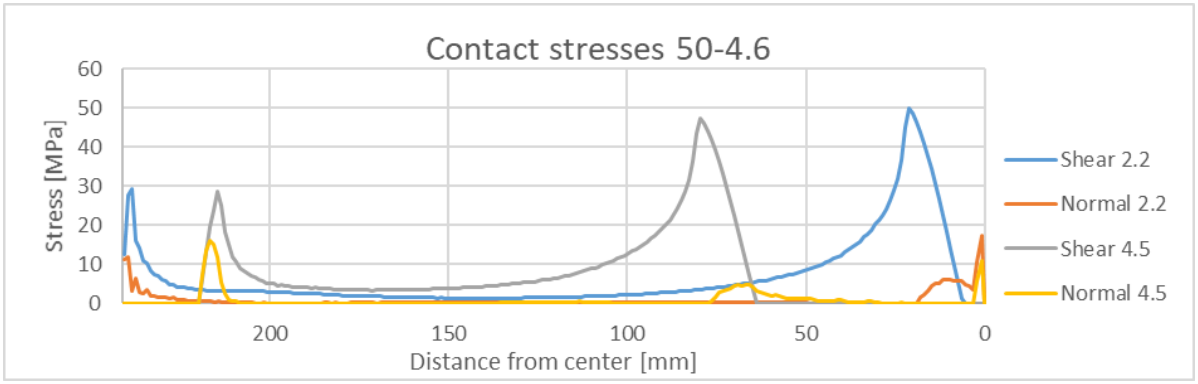

(b) 50-4.6

Figure 5.23: Absolute values of contact stresses

Figure 5.24 shows the force-displacement curve of a model where the bond shear strength is increased to 65MPa and the fracture energy is kept the same. It is observed that the results of this model are extremely similar to the results of the model with bond shear strength of 50MPa. This suggests that the ultimate load of this joint is governed by the fracture energy of the bond, and not the strength. More on increasing the strength of the bond is found in Appendix C.

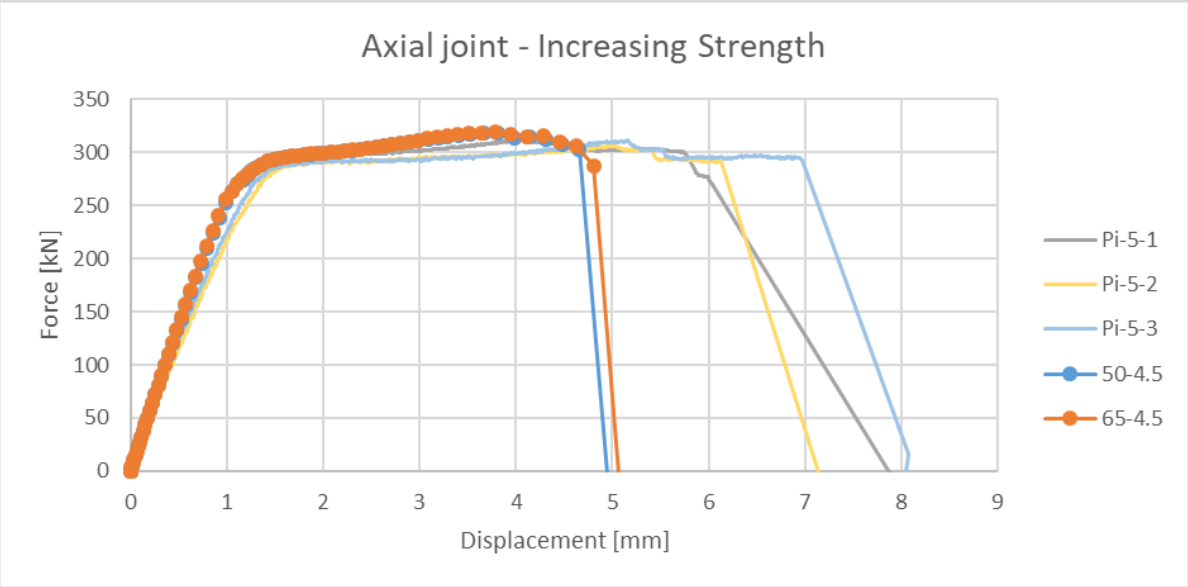

Figure 5.24: Increasing the bond strength has a very limited effect on the force-displacement curve of the axial joint.

5.3. CONCLUSIONS

Although the predictions of the models regarding the force-displacement curve and the failure modes are very good, no unique set of values for the bond shear strength and the fracture energy could be found. It is shown that the fracture energy is the governing parameter for the behaviour of the model. The models are very sensitive to changes in fracture energy, this is because yielding of the steel section occurs simultaneously to the propagation of shear damage in the bond. Default stiffness should be used in the CZM to model the evolution of damage in an accurate way. A sensitivity study shows that for an increment size of 0.005 seconds, the step time should be at least 500 seconds. Also, for a step time of 500 seconds, the largest increment should be 0.005 seconds.

6

FRP FAILURE

In this chapter the process of developing an accurate model for failure of the FRP wrap is described. This will be done according to the approach described in section 3.4. For each model, a force-displacement curve will be shown, as well as an analysis of the failure mode of the model. In figure 6.1 the complete joint is shown and locations A and B are indicated. These locations are defined to describe the failure modes more clearly.

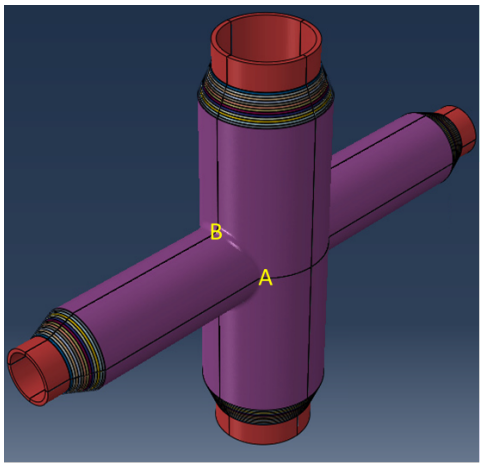

Figure 6.1: Locations A and B

6.1. PLY FAILURE

The first models that include failure of the wrap have the fourteen layer geometry, each layer consists of a few plies, of which one is a bidirectional fabric. This bidirectional ply is lumped into a single ply for simplicity in the next models. The initial values for the strength and the fracture energy as derived from the JRC guideline[5] are shown in table 6.1.

Table 6.1: Strengths and fracture energies of the FRP, based on indicative stiffnesses and strain limits from [5]

	Bidirectional ply	
	Strength [N/mm^2]	Fracture energy [N/mm]
X^T	211.68	2.032
X^C	211.68	3.81
Y^T	211.68	2.032
Y^C	211.68	3.81
S^L	25.2	
S^T	30.24	

The results of the model that uses the parameters from table 6.1 can be seen in figure 6.2. The stiffness of the model is slightly lower than that of the test specimens. The strength and displacement at failure are clearly underestimated. Failure of the model occurs at the same

load level as the first stiffness degradation in the model.

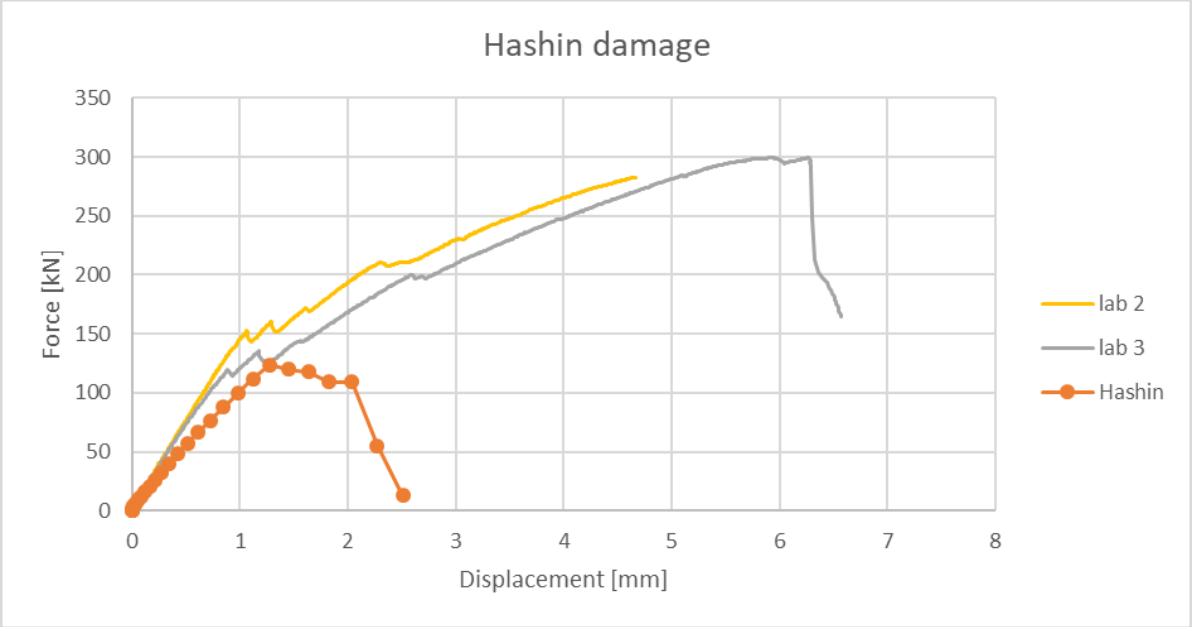

Figure 6.2: The strength and displacement at failure are greatly underestimated

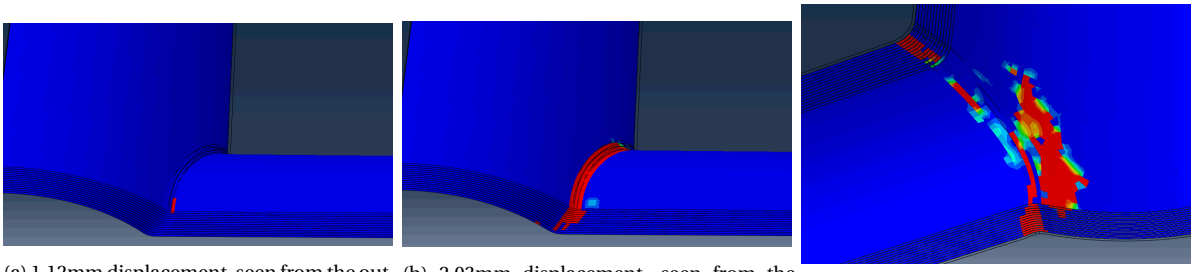

(a) 1.12mm displacement, seen from the outside of the wrap

(b) 2.03mm displacement, seen from the outside of the wrap

(c) 2.50mm displacement, seen from the inside of the wrap

Figure 6.3: Propagation of fibre tensile failure in the root of the joint

In this model the failure mode was failure of the wrap, instead of debonding between steel and FRP. Figure 6.3 shows the evolution of fibre tensile damage in the root of the joint. The damage starts at location A from figure 6.1, figure 6.3a, then it starts propagating in two directions, along the root on the outside of the wrap and inwards towards the steel, figure 6.3b. The damage propagates in these directions until it has completely propagated and the wrap breaks completely, figure 6.3c. Debonding does not play a role in failure of this model, in figure 6.4 it can be seen that there is very little contact damage at the displacement at which the failure load is reached.

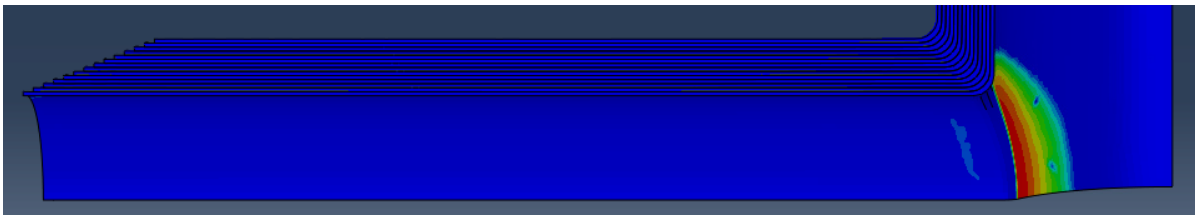

Figure 6.4: Contact damage at 1.28 mm displacement

The strength of the FRP has been doubled and fracture energy has been kept the same in the next model with this geometry. This does improve the results, the propagation of damage occurs in a similar manner as in figure 6.3, but at a higher force and displacement. The force-displacement curves of this model are shown in figure 6.5.

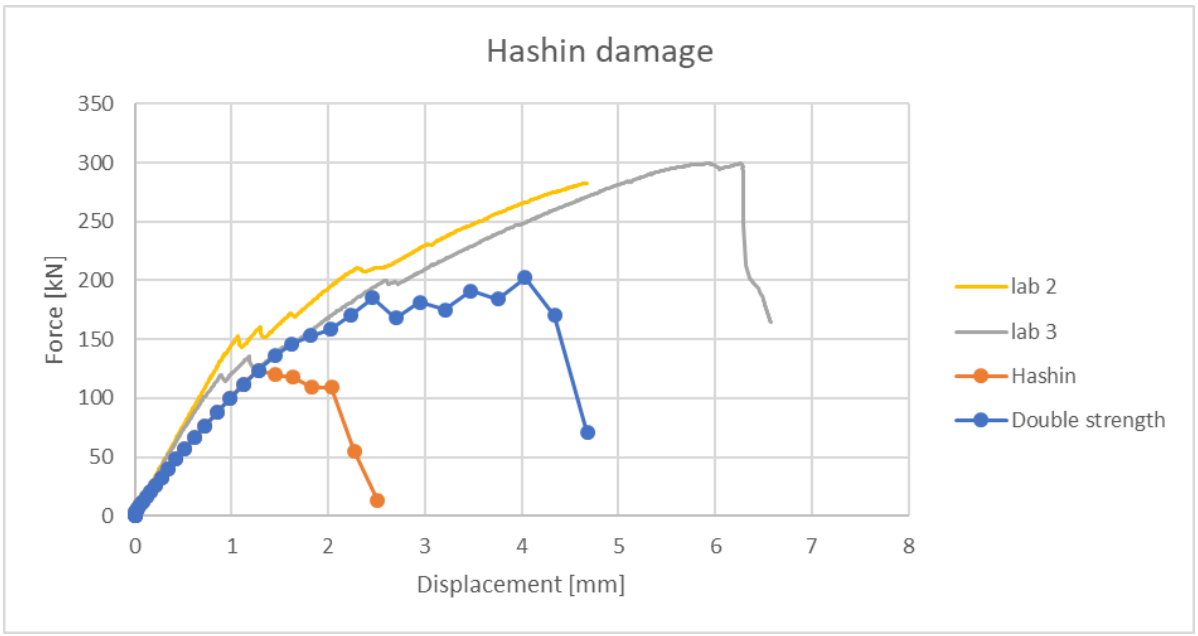

Figure 6.5: Increasing the strength and fracture energy of the FRP leads to a better match of force-displacement curves, however, the values are unrealistically high.

In order to model the failure of the FRP wrap with more accuracy and to be able to distinguish between the different failure modes incorporated in the hashin failure model, the bidirectional ply will be replaced by a layup of UD plies. The values for the strength and fracture energy are displayed in table 6.2. These values where determined following the method described in the JRC guideline, this method can be found in Appendix A.[5]

Table 6.2: Strengths and fracture energies of the FRP, based on stiffnesses from hand calculations and indicative strain limit from [5]

	Unidirectional ply	
	Strength [N/mm^2]	Fracture energy [N/mm]
X^T	536.36	11.53
X^C	351.07	8.78
Y^T	82.82	2.07
Y^C	89.31	2.23
S^L	200	
S^T	200	

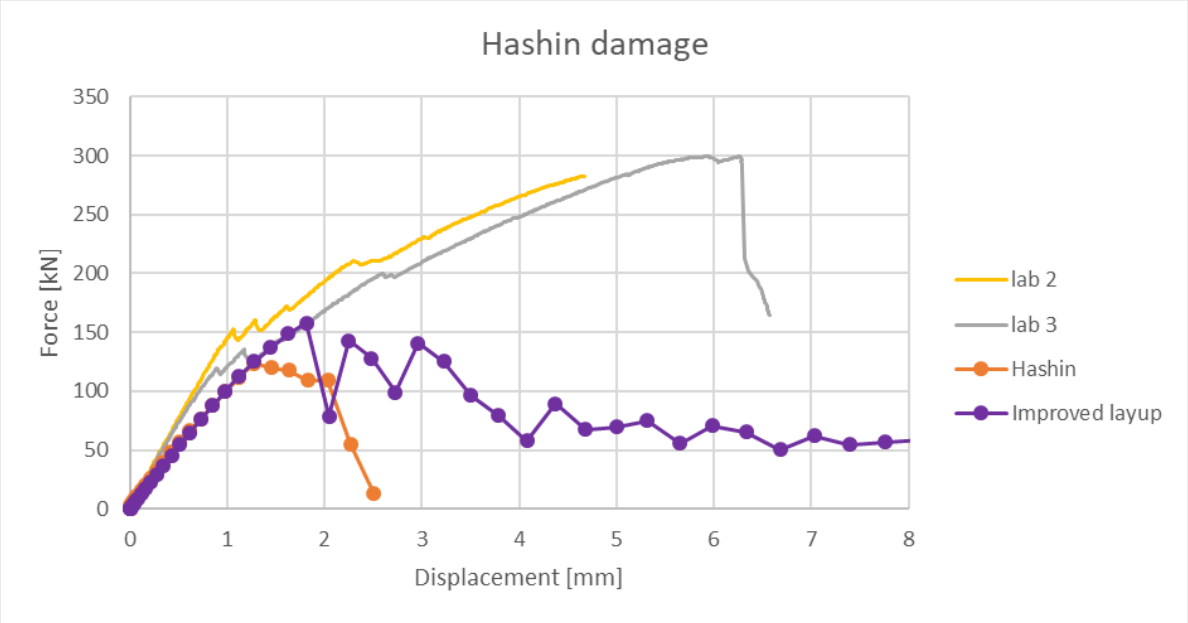

Figure 6.6: The improved layup yields better results, but still fails prematurely.

Figure 6.6 shows the force-displacement curve of the model with the improved layup and new material properties from table 6.2. The stiffness of the model is similar to that of the previous model with the lumped bidirectional plies. The failure load is higher, but still only half as high as the failure load observed in the test specimens. The failure mode of the model is shown in figure 6.7. At 1.82 mm displacement, shear damage is initiated in the root of the joint, figure 6.7a shows that this happens on the outside of the wrap. This damage propagates in a similar manner as in figure 6.3 until the entire cross-section of the wrap is damaged at 3.79 mm displacement, as seen in figure 6.7b. As seen in figure 6.7c, some interface damage occurs, but it does not propagate and is not the final failure mode.

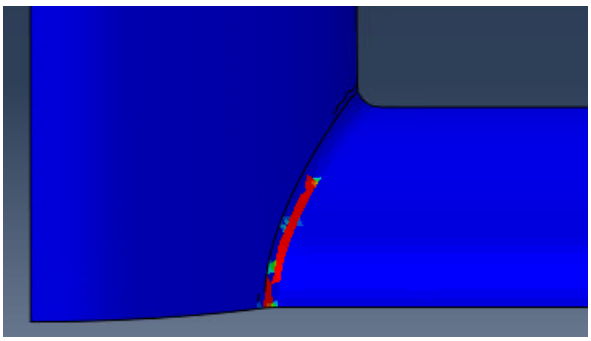

(a) Shear damage at 1.82 mm displacement on outside of wrap

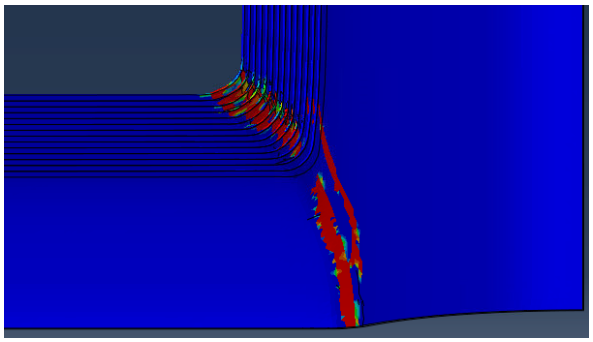

(b) Shear damage at 3.79 mm displacement on inside of wrap

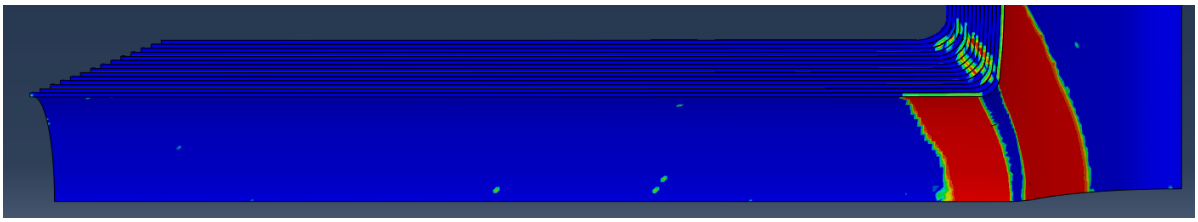

(c) Contact damage on inside of wrap at 3.79 mm displacement

Figure 6.7: Overview of damage in model with improved layup.

A reason for the premature failure might be that the fibre tensile failure mode is too brittle, therefore the corresponding fracture energy was increased to 17.7 N/mm. The results of this model are shown in figure 6.8 and figure 6.10.

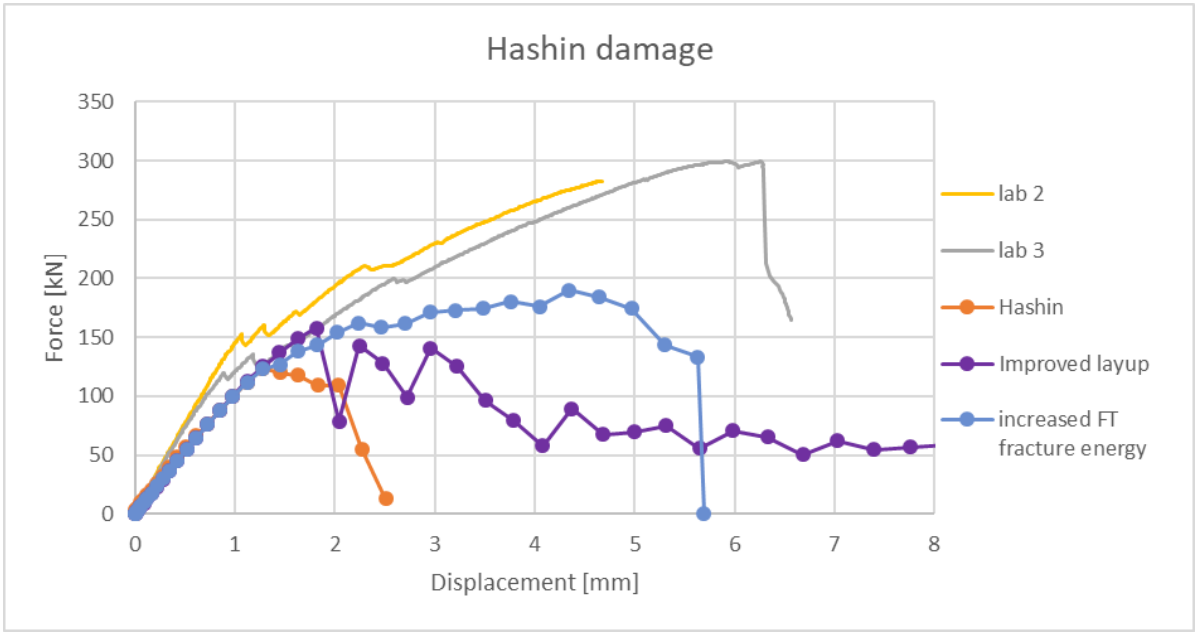

Figure 6.8: Increasing the fibre tensile fracture energy leads to earlier stiffness degradation, contrary to the expectation.

Figure 6.8 shows the force displacement curve of the model with the increased fracture energy. It has the same stiffness until 1.28 mm displacement, after that, a stiffness degradation occurs. At this moment, a lot of debonding occurs on the chord member, this debonding

can explain the sudden loss of stiffness. This debonding is illustrated in figure 6.9. This debonding is caused by the presence of hourglass modes in the model.

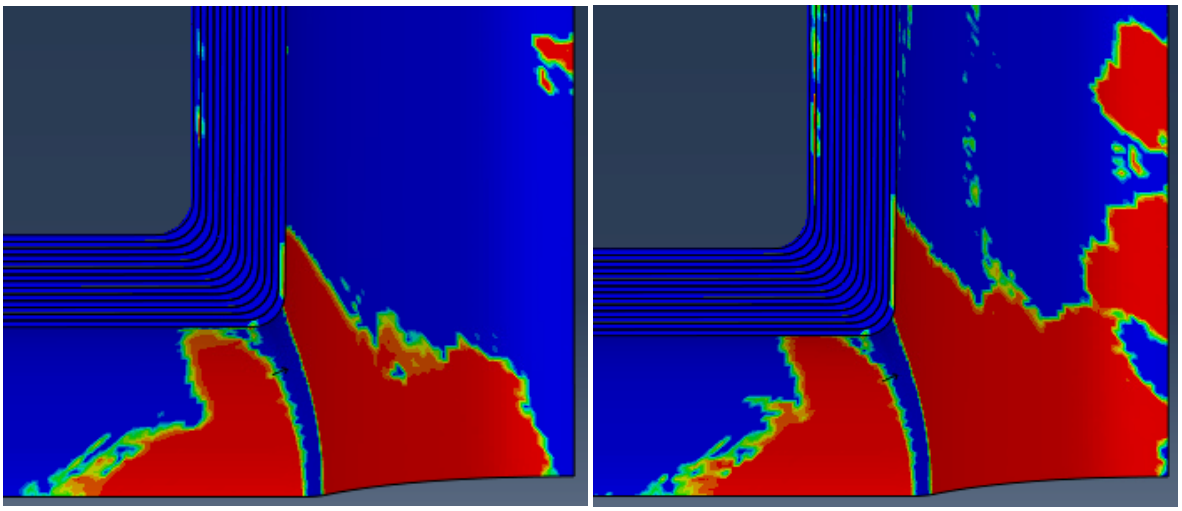

(a) Contact damage at 1.28 mm displacement on outside of wrap (b) Contact damage at 1.45 mm displacement on inside of wrap

Figure 6.9: Propagation of contact damage on the chord member, a possible cause for the unexpected stiffness degradation.

The failure modes of the model with increased fibre tensile fracture energy is shown in figure 6.10. A similar pattern of propagation of shear damage as in figure 6.7 is observed, but at a larger displacement. The propagation of shear damage should happen at a larger displacement, because the fracture energy is higher. Also, in figure 6.10a several small damaged areas are present, this damage is caused by hourglass modes. Hourglass modes where also observed on the steel-FRP interface, as seen in figure 6.10c. More on these hourglass modes and how they are dealt with, are described in chapter 7.

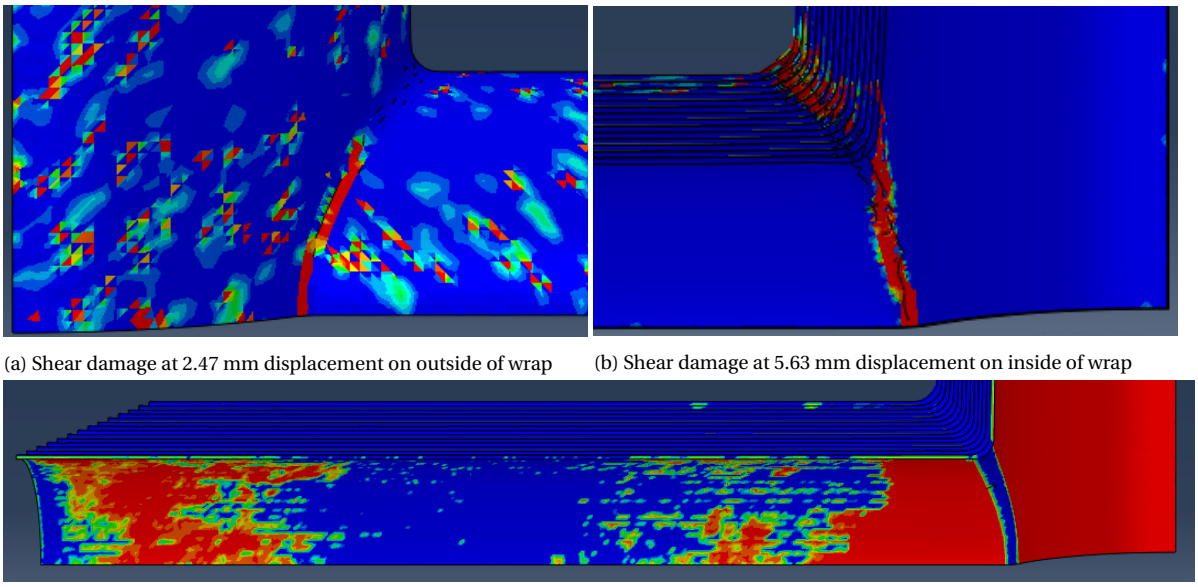

(a) Shear damage at 2.47 mm displacement on outside of wrap (b) Shear damage at 5.63 mm displacement on inside of wrap

(c) Contact damage on inside of wrap at 2.47 mm displacement

Figure 6.10: Overview of damage in model with increased fibre tensile fracture energy.

Another reason for the premature failure of the models is that the geometry of the models is slightly different than that of the specimens in the region where failure of the wrap occurs. Due to the wrapping procedure in the test specimens, more material is present at location A than in the models. As a result of this, the FRP is more in a straight line at location A in the test specimens. Also the radius of the corner at location B is larger in the test specimens. Therefore the geometry was updated, the radius of the corners in locations A and B was increased.

Figure 6.11 shows the force-displacement curve of the model with the improved geometry. It is observed that the stiffness of the model with the improved geometry is slightly higher than the previous model. This increase in stiffness is explained by the change in shape, the increase in corner radius in location A makes it more stiff.

Figure 6.12 shows the failure mode of the model with the updated geometry. It is similar to that observed in figure 6.3, the difference being that the initiation of damage occurs at a larger load and displacement. In figure 6.12a small areas with damage which are not in the root of the joint are observed. The damage in these areas is caused by hourglass modes. The same is valid for some of the damaged areas in figure 6.12c. All damage on the left side of this figure is caused by hourglass modes.

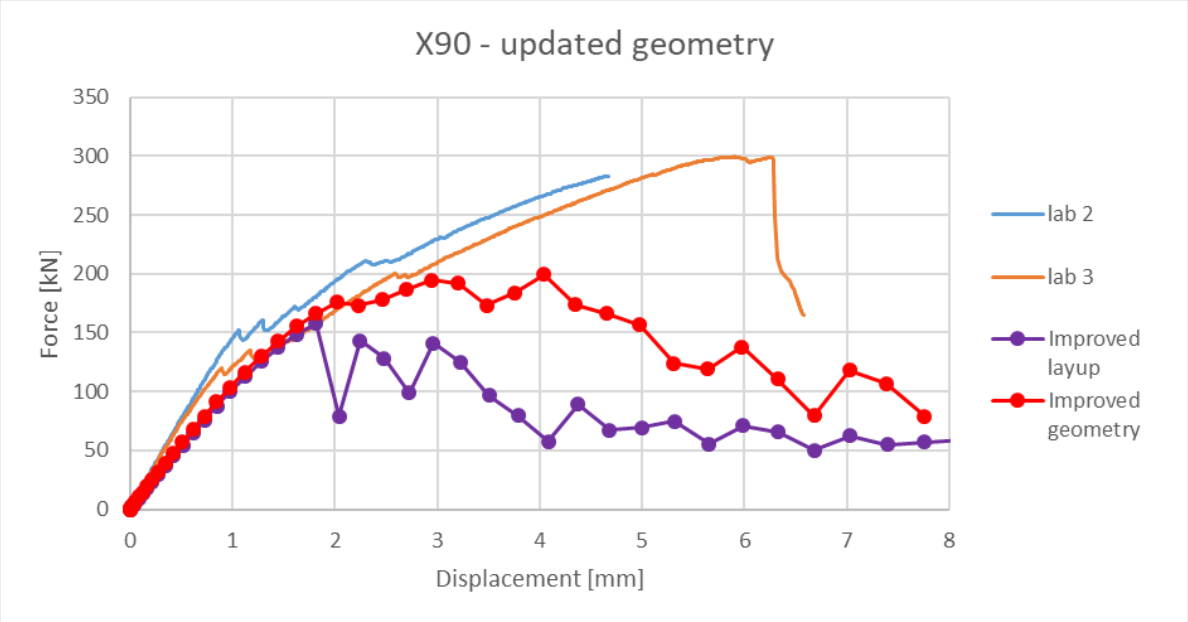

Figure 6.11: The geometry of the joint is slightly changed to be more similar to the actual joint

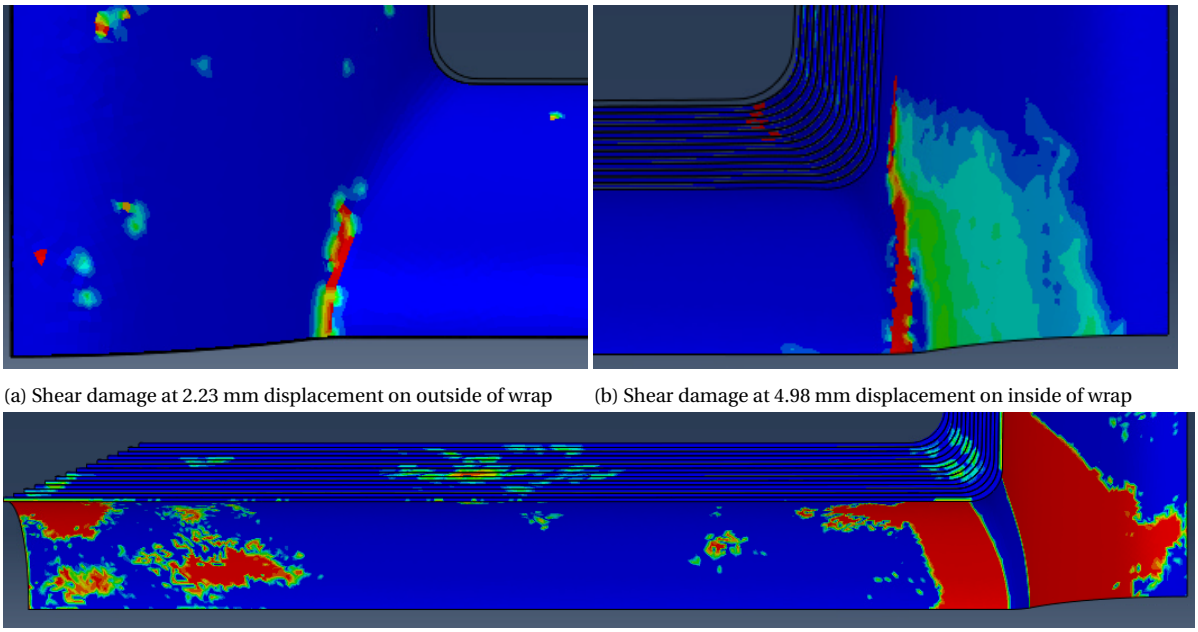

(a) Shear damage at 2.23 mm displacement on outside of wrap

(b) Shear damage at 4.98 mm displacement on inside of wrap

(c) Contact damage on inside of wrap at 2.23 mm displacement

Figure 6.12: Overview of damage in model with the improved geometry.

6.2. CONCLUSIONS

Although the results have improved because of the measures taken in this chapter, the model does not accurately predict the failure load, displacement at failure and failure mode. This can be attributed to two main causes, the geometry of the model is not accurate enough and hourglass modes in critical regions influence the results.

It is possible that the material properties used in the models are not in correspondence with the actual material properties, but they are sufficiently realistic to be used when the models will be improved. The first step in improving the models will be to model the geometry more accurately. This can be done by doing a 'forming' simulation, in which the plies are first positioned near the steel pieces and then are squeezed against the steel. This will result in a more accurate representation of the geometry of the joint, and will cause more material to be at location A, which will further reduce stress concentrations in this region. This should lead to a higher, more realistic failure load of the models.

7

HOURGLASS MODES

In this chapter the hourglass modes that were encountered and the actions taken to mitigate them are described. First, the models with an isotropic FRP material model will be discussed, then the models with an orthotropic FRP material model will be discussed.

7.1. HOURGLASS MODES IN REGULAR MESHES

The first occurrence of hourglass modes in research leading up to this thesis is described in section 4.2.1. The hourglass modes occurred in the models with the four layer geometry. As described in the section mentioned previously, this was solved by using the stiffness hourglass control method. The effect of using the stiffness hourglass control method is illustrated in figure 7.1. In this figure two contour plots of the contact damage parameter are shown. In figure 7.1a the pattern of stripes indicates the presence of hourglass modes, this pattern is absent in figure 7.1b, where stiffness hourglass control was used. It was found that using the enhanced hourglass control method gave the same result as using the stiffness hourglass control method. This is visible when comparing the force-displacement curves in figure 4.14 and confirmed through inspection of the contour plots from the output database.

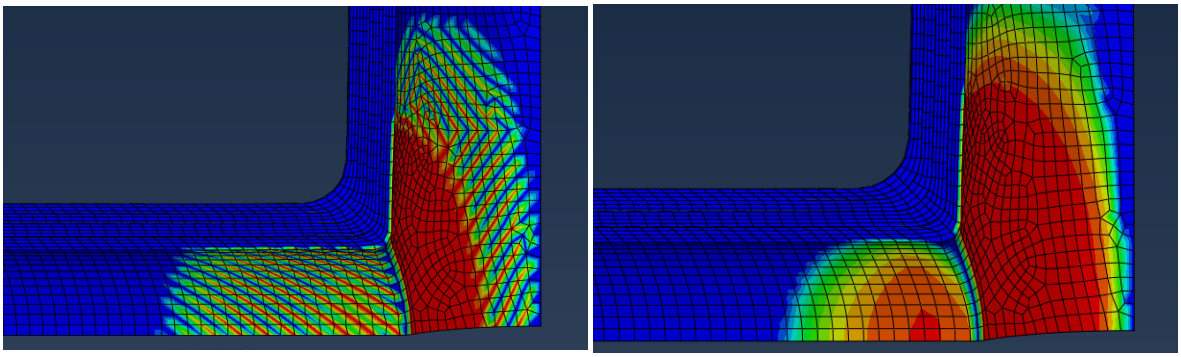

(a) Default hourglass control at 5.1 mm displacement

(b) Stiffness hourglass control at 5.1 mm displacement

Figure 7.1: Using the stiffness hourglass control option solves the hourglassing of elements in the 4 layer geometry. The contact damage parameter is plotted in these contour plots

As mentioned in section 2.1.3 hourglassing can be assessed by a combination of visual inspection and the ratio of artificial strain energy and strain energy. The artificial energy

should be negligible compared to the strain energy. Figure 7.2 shows the ratio between artificial strain energy and strain energy of the model with default hourglass control. Up to 5 mm displacement, the ratio is less than 5%, for displacements from 5 mm to approximately 13 mm the ratio is around 5% and for larger displacements, the ratio grows strongly. However, the large ratio for large displacements can be disregarded because this is after the model has failed. A ratio of 5% is generally on the edge of being acceptable. Visual inspection of the model in figure 7.1a suggest that hourglassing only occurs in the FRP in the elements adjacent to the steel. Since the energy ratio takes into account the entire model, the hourglass modes can be called severe.

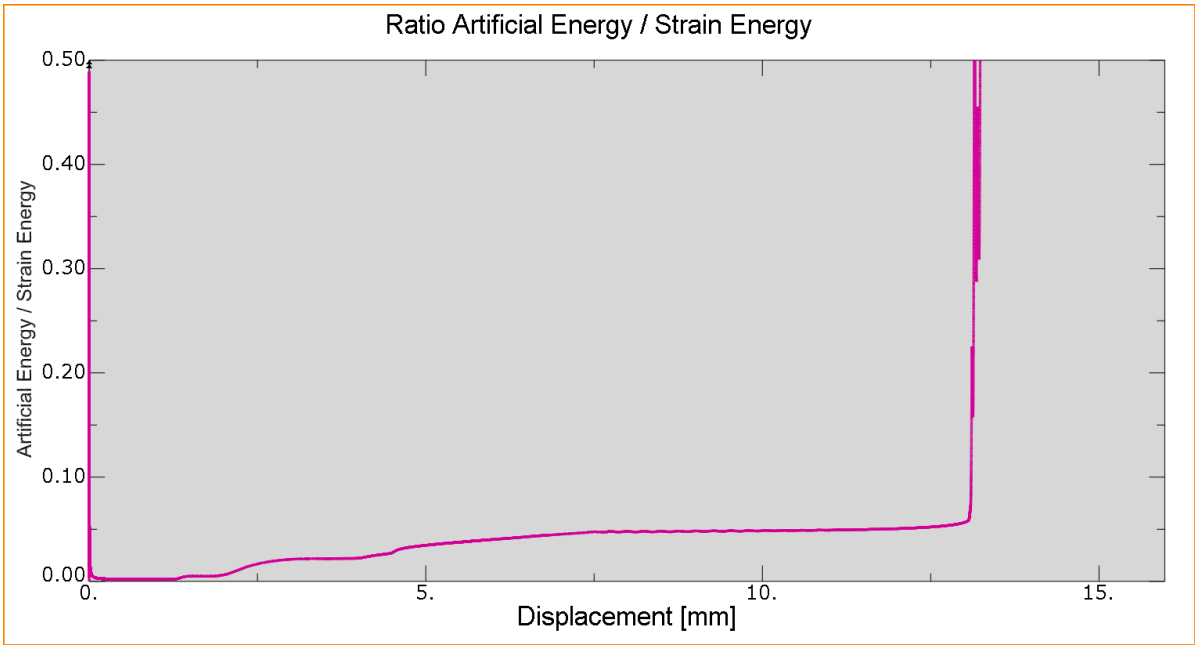

Figure 7.2: Ratio of hourglass energies four layers with default hourglass control

Figure 7.3 shows the energy ratio of the model with stiffness hourglass control. Up to a displacement of 7 mm, the energy ratio is smaller than 1%. For displacements larger than 7 mm, the ratio increase rapidly. The model fails at a displacement of 7mm, so this can be disregarded. Since the artificial strain energy is negligible compared to the strain energy, up to failure no influence of hourglassing is expected in the model. Visual inspection of figure 7.1b confirms this.

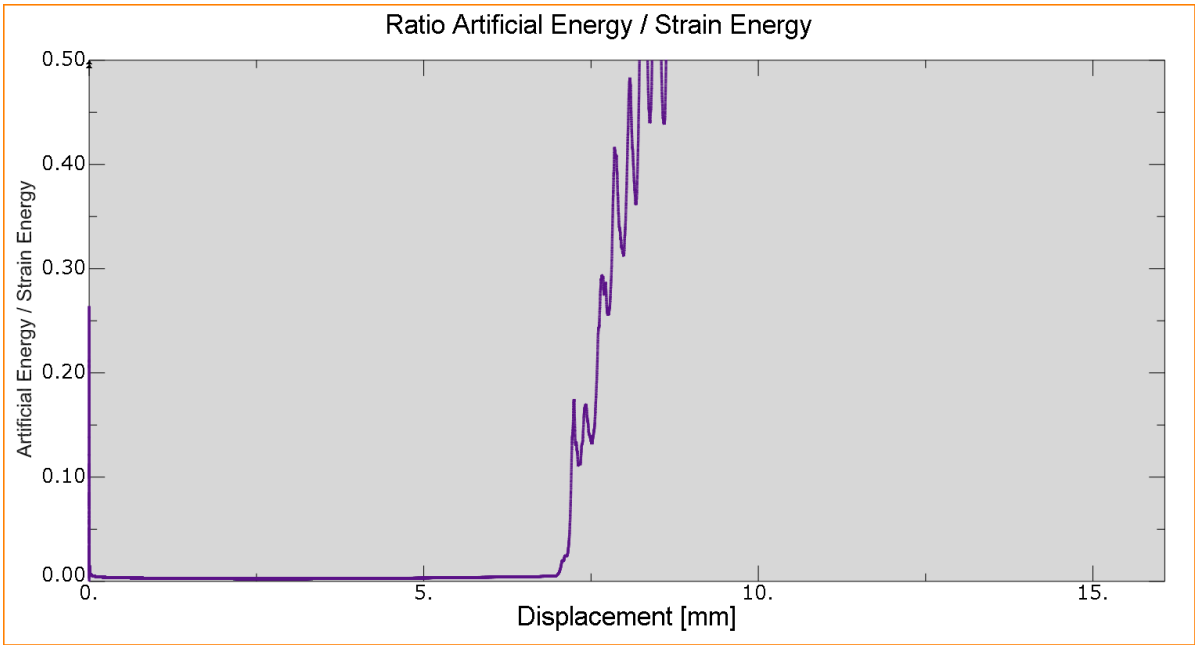

Figure 7.3: Ratio of hourglass energies four layers with stiffness hourglass control

As stated in section 4.3.2, in the models with the fourteen layer geometry hourglass modes occurred. The hourglass modes first occurred early in the analysis step, after only 0.1mm displacement. In figure 7.4 contour plots of the contact damage output parameter are compared. Figure 7.4a shows the output for a model with an approximate element size of 4mm and figure 7.4b for a model with an approximate element size of 2mm. More damage was observed in the model with the larger elements than when smaller elements are used. This suggests that the element size influences the hourglass behaviour.

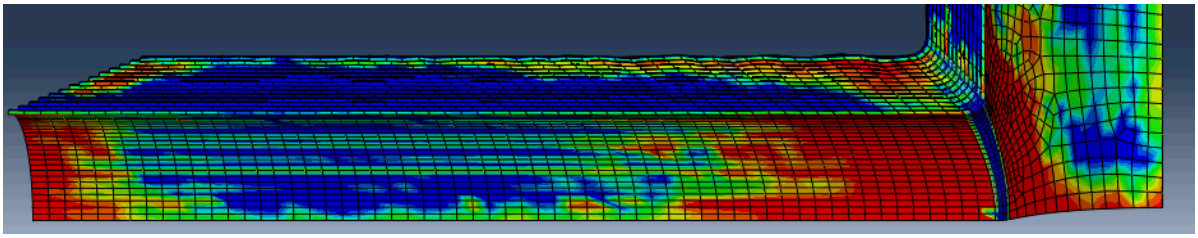

(a) Approximate element size is 4mm

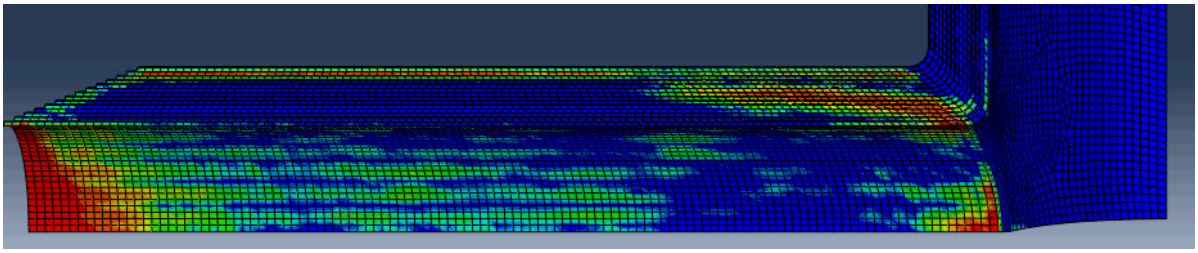

(b) Approximate element size is 2mm

Figure 7.4: Hourglassing made visible by the contact damage output parameter. Smaller elements seem to be affected less by hourglass modes, but still severely. Contact damage is not expected at a displacement of 0.1mm.

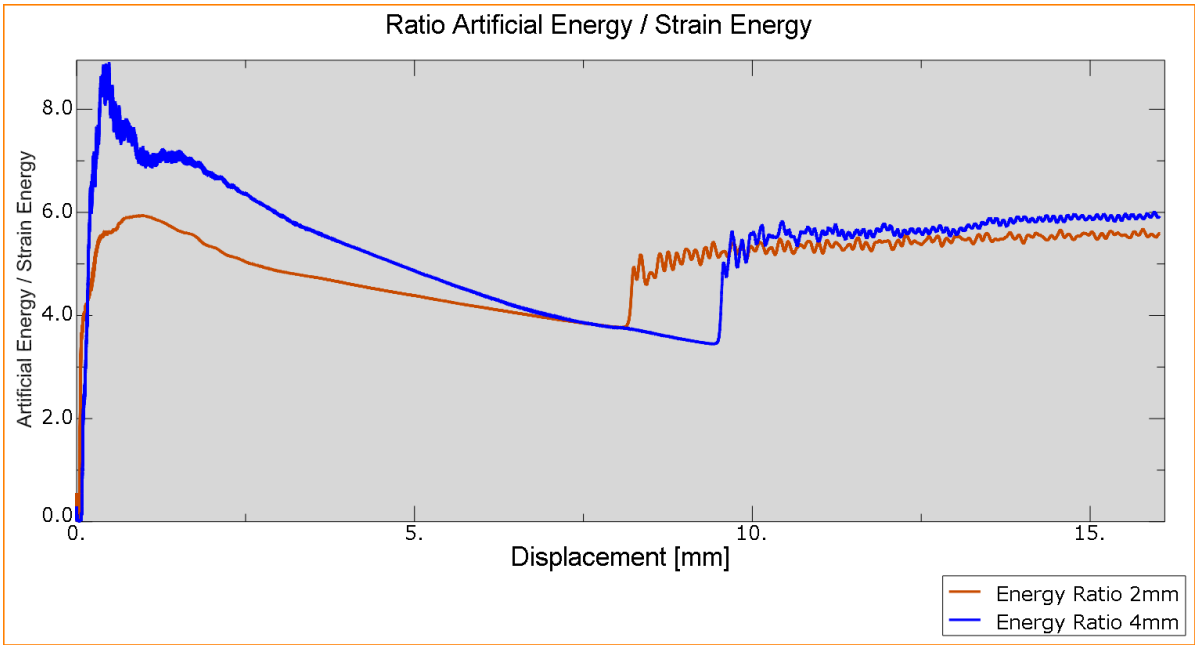

Figure 7.5: Ratio of hourglass energy in model with 4mm elements

Figure 7.5 shows the energy ratios of the models with 4mm and 2mm elements, the energy ratio is higher than one for all displacements in both models. Both models suffer severely from hourglass modes. The energy ratio of the model with 4mm elements is higher than the ratio of the model with 2mm elements. It is observed that, similar to previous curves of energy ratios, the energy ratio increases after failure of the model.
In figure 7.6 it is clearly visible that the displacements caused by hourglass modes are a lot smaller in the model with smaller elements. This supports the suggestion that models with smaller elements are less affected by hourglass modes.

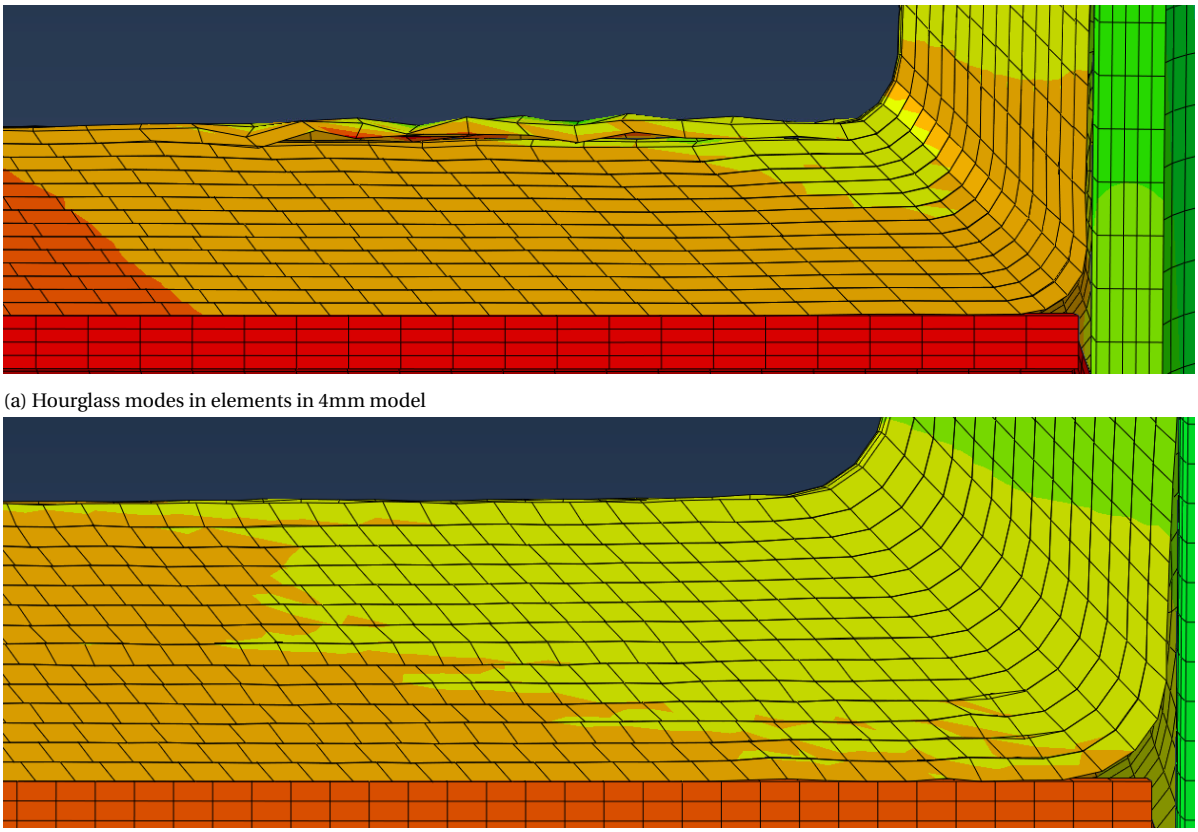

(a) Hourglass modes in elements in 4mm model

(b) Hourglass modes in elements in 2mm model

Figure 7.6: Displacements caused by hourglass modes are clearly visible. The model with smaller elements seems less affected by the hourglass modes.

The force-displacement curves in figure 7.7 confirm that the model with 2mm elements is affected less by the hourglass modes than the model with 4mm elements. The wobble at the beginning of the force-displacement curve of the model with 2mm elements seems to be caused by the hourglass modes, which means that the hourglass modes are present in this model. This is supported by figure 7.5 and figure 7.4b, where contact damage is visible at the same displacement as the wobble in the force-displacement curve.

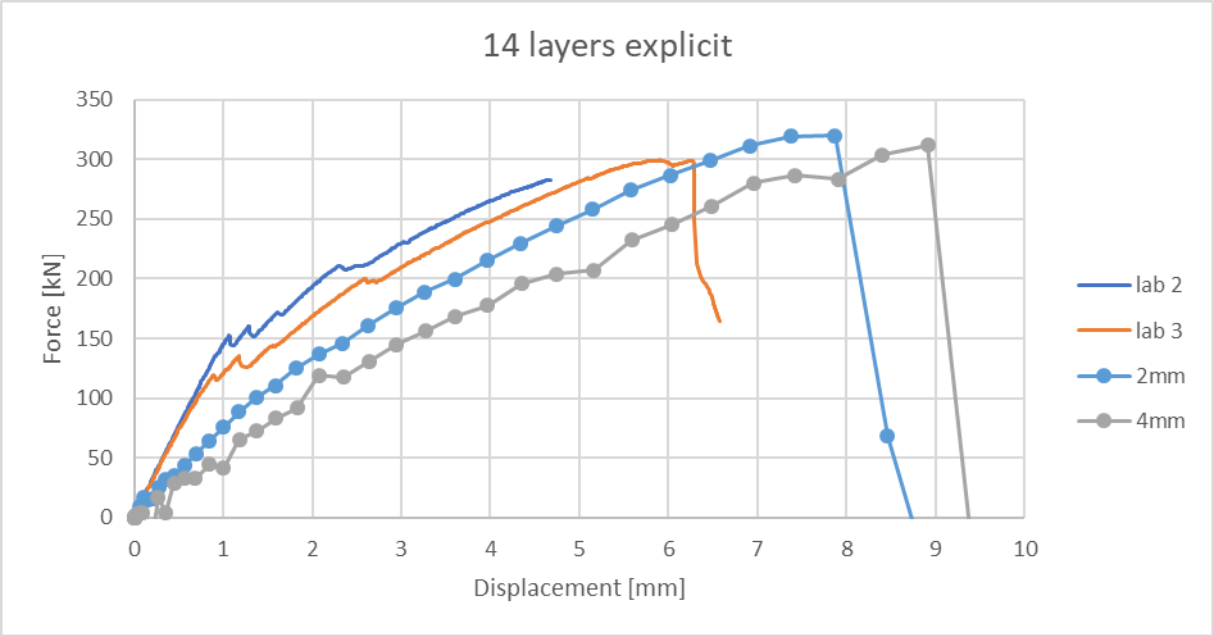

Figure 7.7: Wobbles in force-displacement curves are caused by hourglass modes.

To reduce the effects of hourglass modes, Abaqus/Explicit offers a number of hourglass control options, which are described in chapter 2. All these hourglass control options have been applied to the model with 2mm elements and their force-displacement curves were plotted, this is shown in figure 7.8.

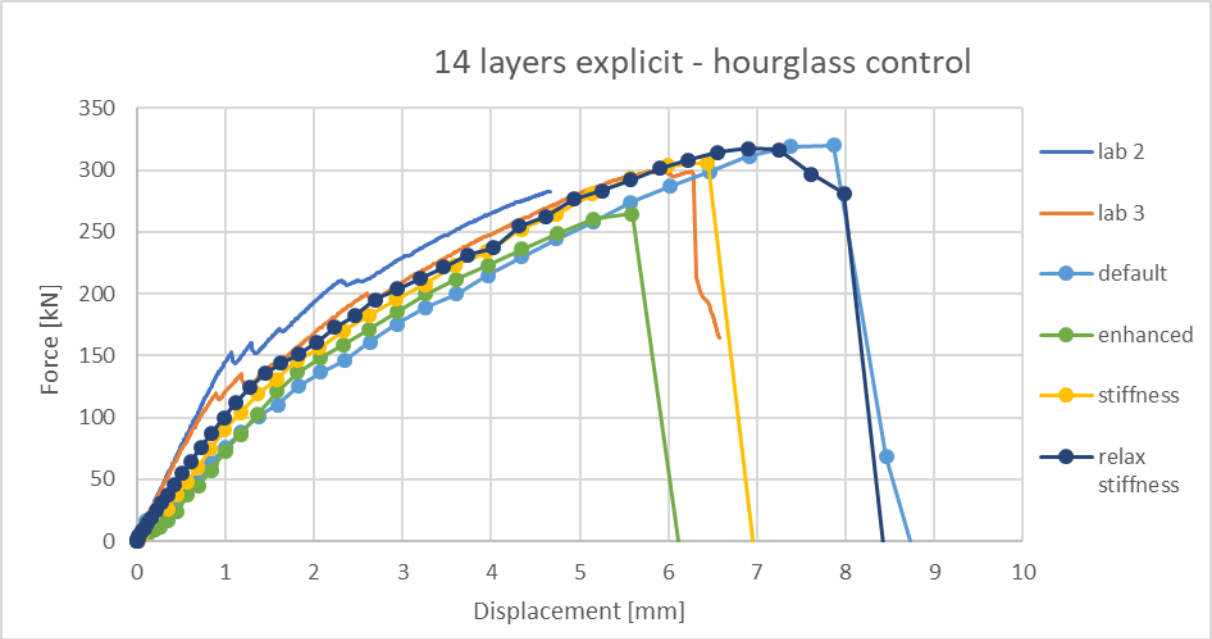

Figure 7.8: Different hourglass control options

In figure 7.9 contour plots of the moments that hourglass modes first occur in the models are shown. The hourglass control option for which hourglass modes occur first at the smallest displacement, is the default hourglass control option. Hourglassing starts at 0.06mm

displacement and it propagates through the wrap around the brace member almost instantly. A contour plot is shown in figure 7.9a and the effect of this severe hourglassing is seen in figure 7.7, where a stiffness degradation and a wobble are observed at 0.06mm displacement.

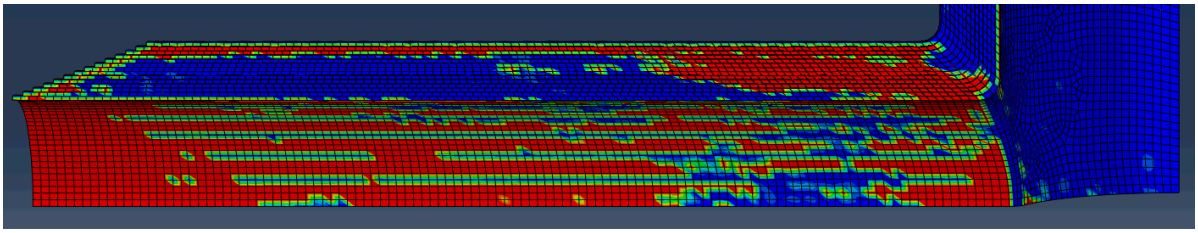

(a) Default hourglass control at 0.06mm displacement

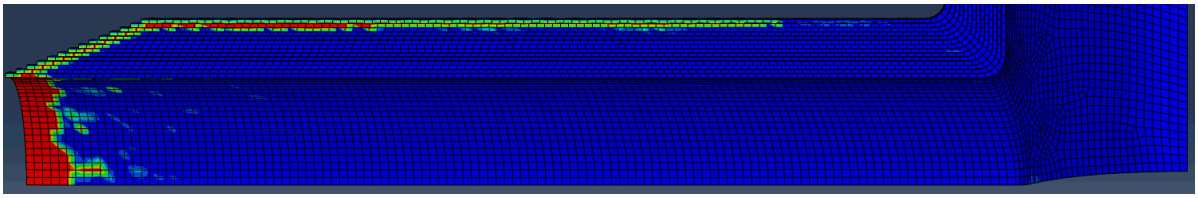

(b) Enhanced hourglass control at 0.10mm displacement

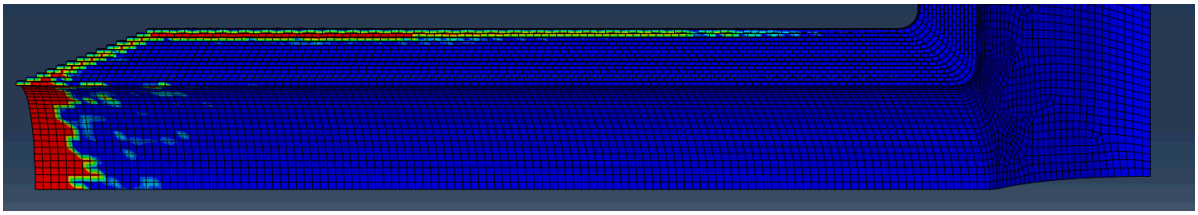

(c) Stiffness hourglass control at 0.10mm displacement

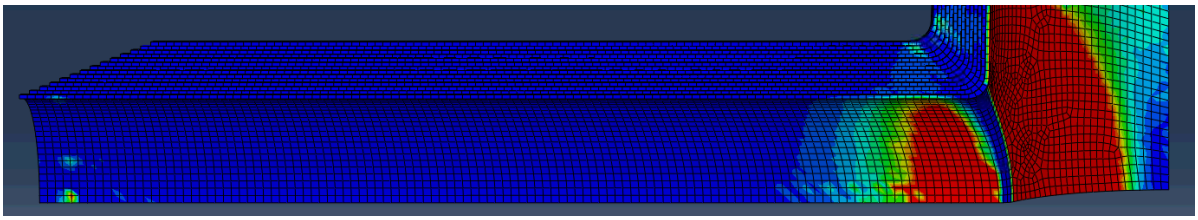

(d) Relax stiffness hourglass control at 2.02mm displacement

Figure 7.9: Hourglass modes made visible by the contact damage initiation parameter. The figures show the contour plots at the displacement where hourglass modes first occur.

Figures 7.9b and 7.9c show that little difference exists between the enhanced hourglass control method and the stiffness hourglass control method at the displacement where hourglassing is initiated. However, comparing the force-displacement curves of these models in figure 7.8, a difference is observed at very low displacement. After initiation of the hourglass modes, the model with enhanced hourglass control lose a lot of stiffness, while the model with stiffness hourglass control has the same stiffness as before the hourglass modes were initiated. After about 1mm displacement, the model with enhanced hourglass control regains its stiffness.

The relax stiffness hourglass control option delays the initiation of hourglassing significantly compared to the other hourglass control methods. Figure 7.9d show that hourglass-

ing is initiated at 2.02mm opposed to 0.1mm for the other hourglass control methods. This also reflects on the force-displacement curve of this model, seen in figure 7.8. It is linear until approximately 1.2mm, where some stiffness degradation occurs. This stiffness degradation is expected at this displacement. From approximately 1.4mm the curve starts undulating slightly, which corresponds to the initiation of hourglass modes.

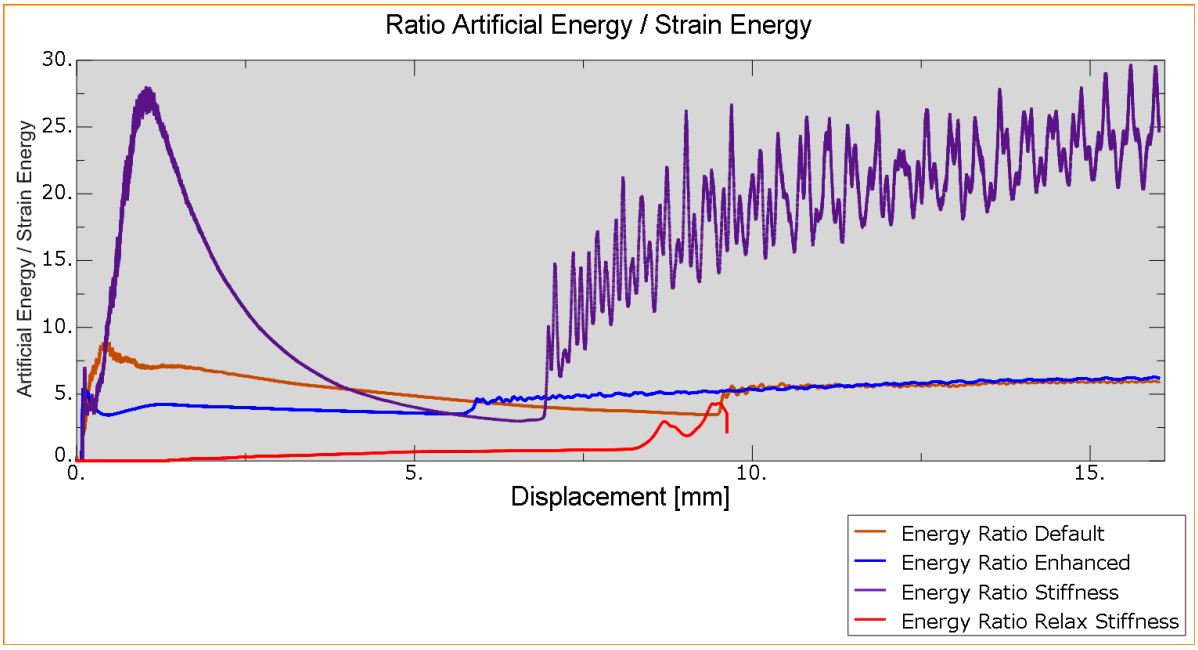

Figure 7.10: Ratios of hourglass energy in models with varying hourglass control methods.

Figure 7.10 shows the energy ratios of the models with different hourglass control options. The ratios of the models with default, enhanced and stiffness hourglass control are very high for all displacements while the energy ratio of the model with relax stiffness hourglass control gradually increases to a value of approximately one at 8 mm displacement. The rapid increase of the energy ratios of the models with default, enhanced and stiffness hourglass control corresponds to the appearance of hourglass modes at low displacements in figures 7.9a, 7.9b and 7.9c.

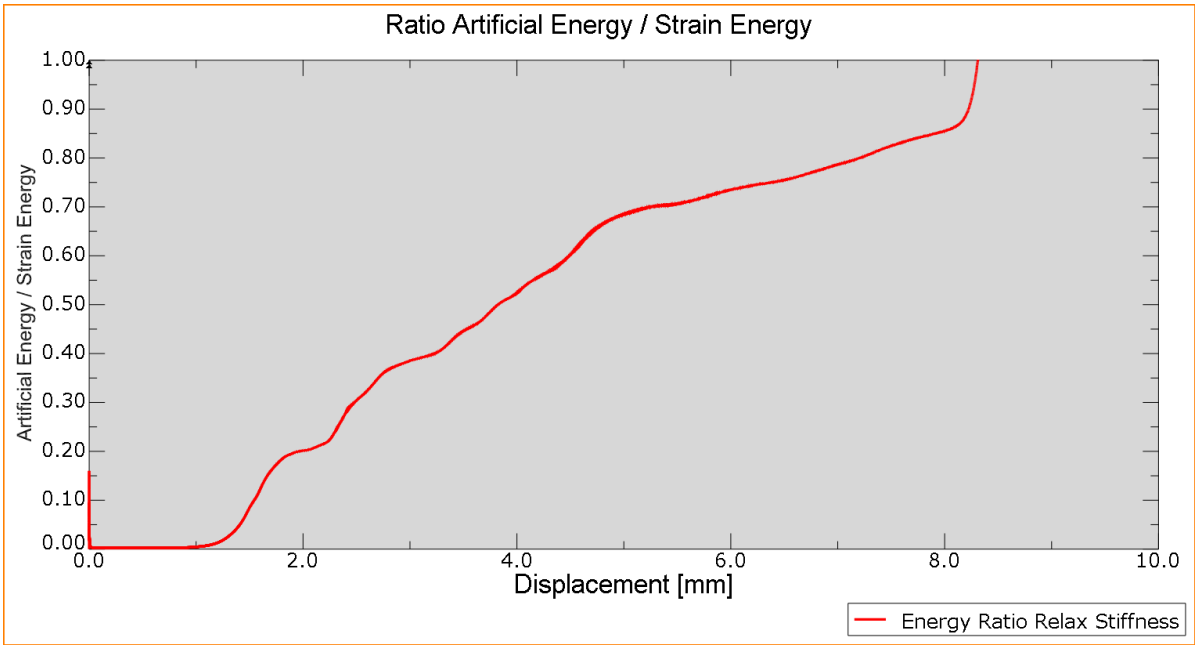

Figure 7.11: Ratio of hourglass energy in model with relax stiffness hourglass control.

In figure 7.11 the energy ratio of the model with relax stiffness hourglass control is shown in more detail. The energy ratio is very low until 1mm displacement, from 1mm displacement onward, the energy ratio starts increasing. From approximately 1.4mm displacement, the energy ratio exceeds 5%, which is too high. This is the point where the stiffness of the model decreases and undulations in the force-displacement curve appear, this can be seen in figure 7.8. This suggests that the undulations in the force-displacement curve are caused by hourglass modes.

From figures 7.8, 7.9 and 7.11 the relax stiffness hourglass control method seems to be the best hourglass control method for these models. However, hourglassing is still a problem, it has a significant influence on the results of the model and figure 7.11 shows that the hourglass energy ratio is too high. In section 2.1.3 it is mentioned that in most cases, hourglass modes are restrained by neighbouring elements. In these models, they are clearly not restrained by neighbouring elements, the mesh is extremely regular in the regions where hourglass modes occur. This suggests that making the mesh more irregular should reduce the effects of hourglass modes.

7.2. HOURGLASS MODES IN IRREGULAR MESHES

Figure 7.12 shows an axial model with hourglass modes appearing at 0.15mm displacement, this is the lowest displacement at which the hourglass modes are visible. Figure 7.13 shows the corresponding energy ratio, it is observed that the energy ratio increases a lot at 0.15mm displacement. The energy ratio is very high, for displacements larger than 0.15mm, indicating severe hourglassing in the model.

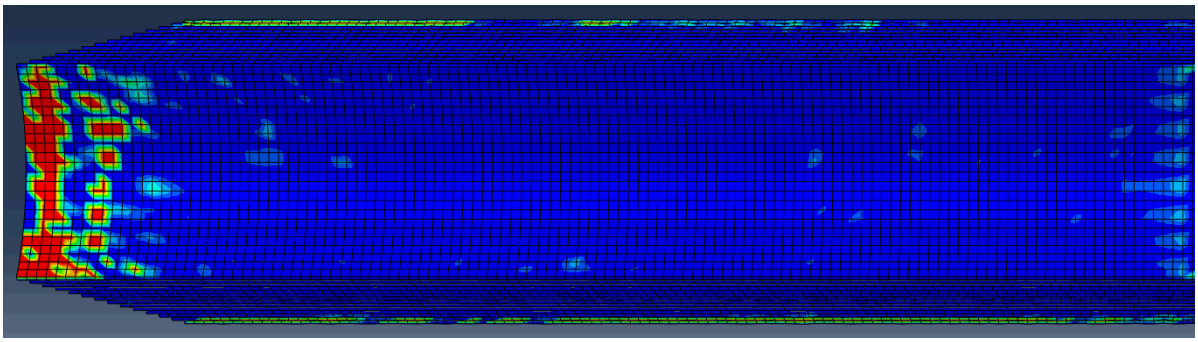

Figure 7.12: Hourglass modes are visible on the outside layer and near the end of the wrap, at 0.15mm displacement.

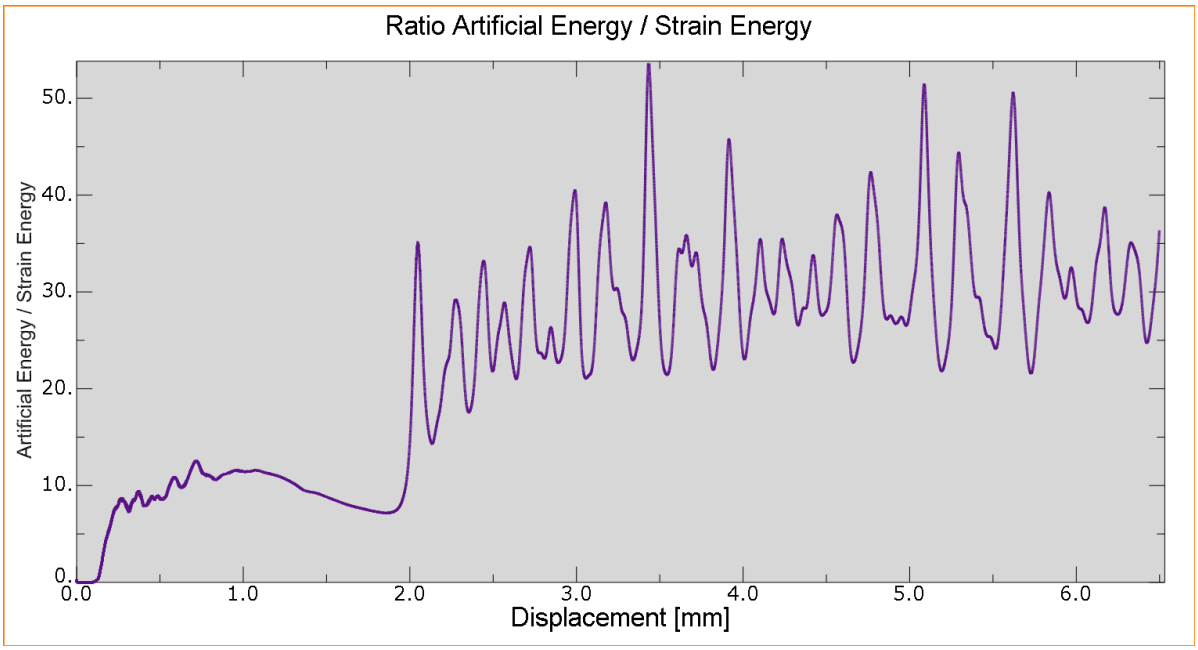

Figure 7.13: Ratio of hourglass energy in axial model.

Figure 7.14 shows the same model as figure 7.12, the difference being that the model in figure 7.14 has wedge elements. There is some hourglass modes, but at much larger displacement and the hourglass modes are less severe, they are only on the interface between the steel and FRP. In section 2.1.3 it is mentioned that the hourglass energy ratio cannot be plotted for models that use wedge elements, because wedge elements do not have hourglass control in Abaqus. Therefore, no hourglass energy plots are shown for models that consist of wedge elements.

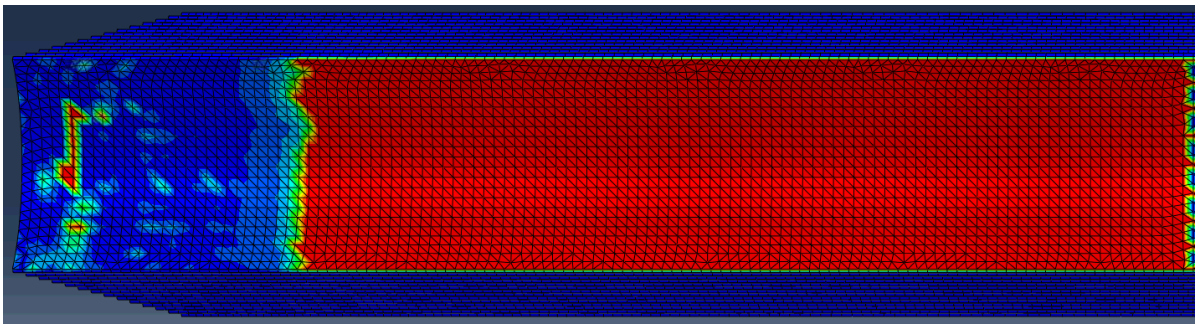

Figure 7.14: Using wedge elements, initiation of hourglassing occurs just before failure, at 0.97mm displacement and only on the steel-FRP interface.

Figure 7.15 shows the interface damage of a model with wedge elements, where the elements size changes through the thickness of the wrap and with a significantly finer mesh on the inside layer of FRP. This model does not suffer from hourglass modes.

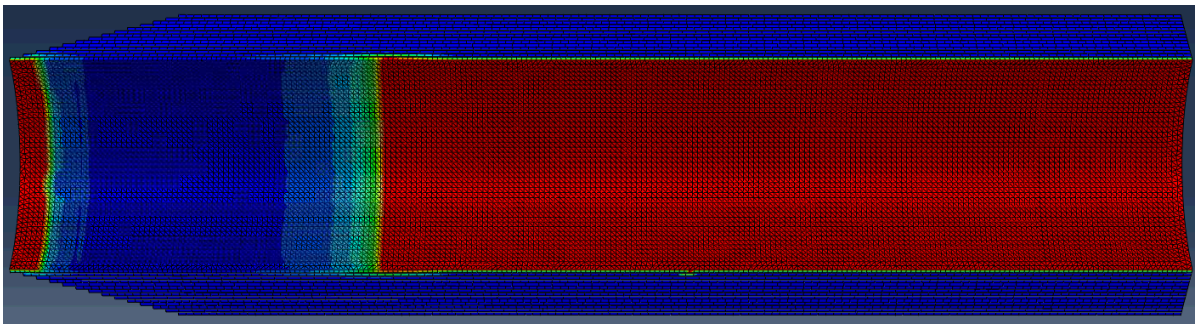

Figure 7.15: Using wedge elements and a finer mesh on the inside layer, no hourglassing occurs in the model before failure.

It seems that have a mesh with wedge elements and a varying element size through the thickness of the wrap solves the hourglass problem in axial models. The same method was tested on the X90 geometry. The results of this are seen in figures 6.10a and 6.10c. The spotted areas with shear damage in figure 6.10a indicate the presence of hourglass modes. The same thing can be said about the spotted areas which are not near the root of the joint in figure 6.10c. A lot of hourglass modes are observed in the model in these figures. This model only has an irregular mesh through the thickness of the wrap, in the curved plane of the plies, the mesh is still very regular.
To improve the hourglass behaviour, in-plane irregularity was introduced into the mesh. The model of which results are shown in figures 7.16b and 7.16d has this in-plane irregular mesh. Comparing figures 6.10a and 7.16b, it is observed that while the model with the in-plane irregular mesh still has some hourglass modes, is has significantly less of them than the model with only through thickness irregularity. The same is observed when considering figures 6.10c and 7.16d. It is also observed that the model with in-plane irregularity has local contact damage between the layers of FRP, this damage is also caused by hourglass modes.

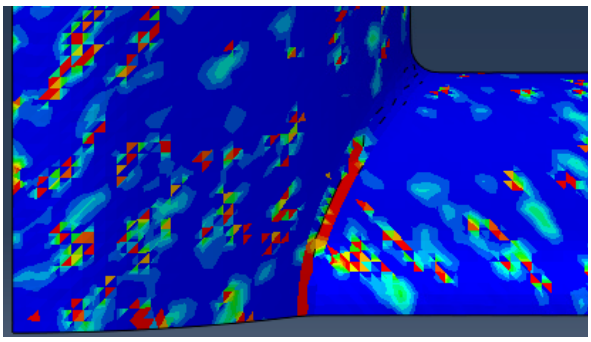

(a) Shear damage at 2.47 mm displacement in model with wedge elements

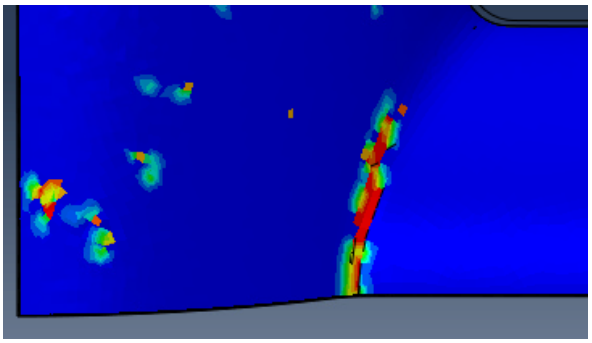

(b) Shear damage at 2.47mm displacement in model with in-plane irregular hex mesh

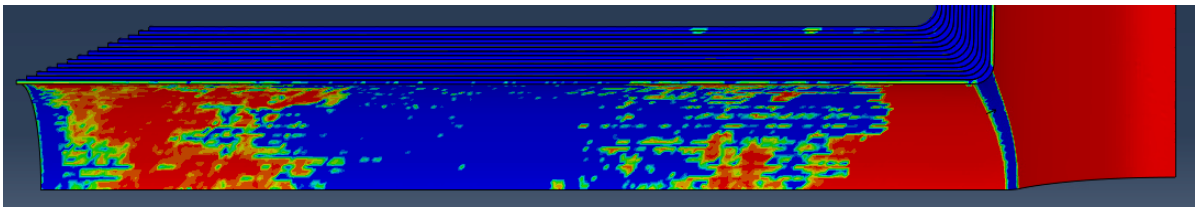

(c) Contact damage on inside of wrap at 2.47 mm displacement in model with wedge elements

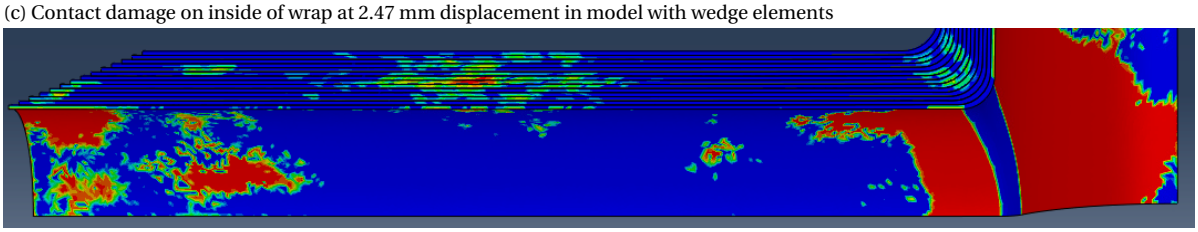

(d) Contact damage on inside of wrap at 2.47 mm displacement in model with in-plane irregularity

Figure 7.16: Hourglass modes are indicated by shear damage on the outside of the wrap and contact damage on the inside of the wrap.

Figure 7.17 shows a comparison of model with both through thickness and in-plane irregularity with stiffness hourglass control and relax stiffness hourglass control. Figures 7.17a and 7.17b show the difference in hourglass modes on the outside of the wrap at a displacement of 2.47 mm. It is observed that the model with relax stiffness hourglass control has slightly more hourglass modes on the outside of the wrap at this displacement. On the inside of the wrap, the opposite is true, as seen in figures 7.17c and 7.17d. The model with relax stiffness hourglass control has less hourglass modes on the inside of the wrap. Another observation is made, the model with stiffness hourglass control has hourglass modes inside of the wrap, while the model with relax stiffness hourglass control does not have hourglass modes inside of the wrap. It must be noted, that the differences in visible hourglass modes are small.

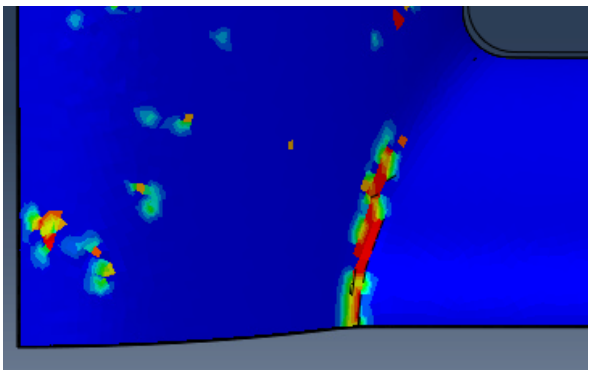

(a) Shear damage at 2.47mm displacement with stiffness hourglass control.

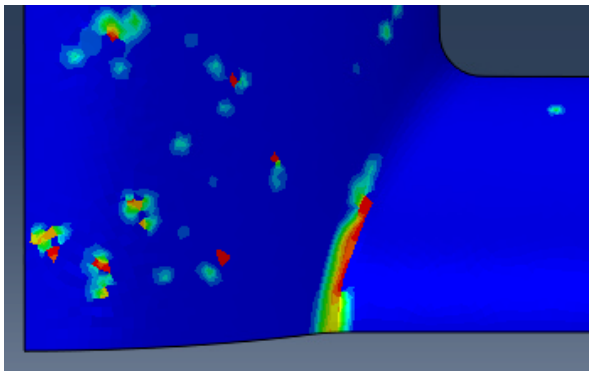

(b) Shear damage at 2.47 mm displacement with relax stiffness hourglass control.

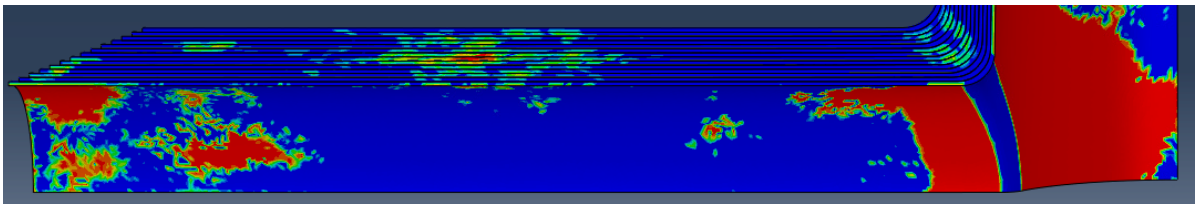

(c) Contact damage on inside of wrap at 2.47 mm displacement with stiffness hourglass control.

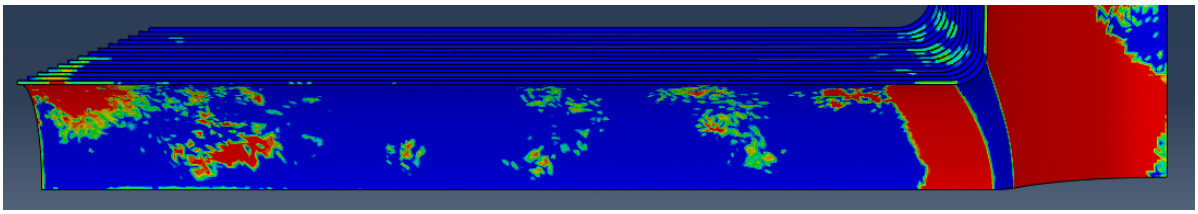

(d) Contact damage on inside of wrap at 2.47 mm displacement with relax stiffness hourglass control.

Figure 7.17: Hourglass modes are indicated by shear damage on the outside of the wrap and contact damage on the inside of the wrap.

Figure 7.18 shows the energy ratios of the models with through thickness and in-plane irregularity with stiffness and relax stiffness hourglass control. It is observed that the energy ratio of the model with relax stiffness hourglass control is higher than the energy ratio of the model with stiffness hourglass control. This means that the model with relax stiffness hourglass control has means hourglass modes than the model with stiffness hourglass control. This is in accordance to the observation made in figure 7.17 that the model with relax stiffness hourglass control has slightly more visible areas with hourglass modes.

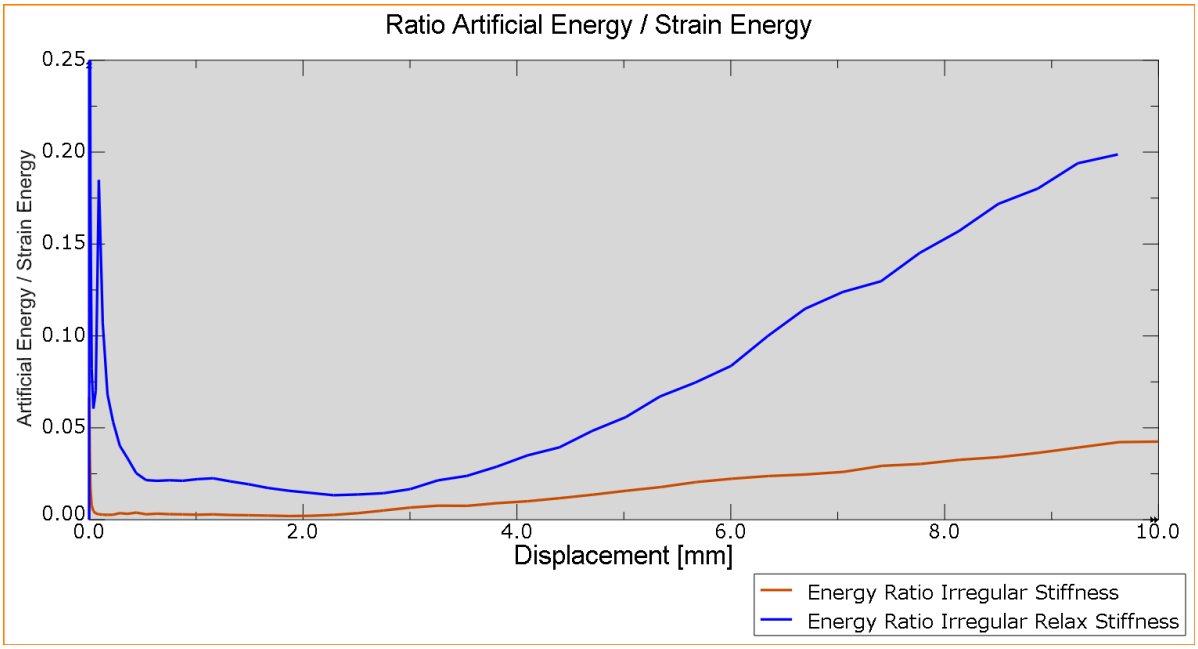

Figure 7.18: Ratio of hourglass energy in models with irregular mesh.

Figure 7.19 shows the force-displacement curves of the models with irregular mesh and stiffness and relax stiffness hourglass control. The curves are very similar, only minor differences are observed. The model with relax stiffness hourglass control has some stiffness degradation at 1.5mm displacement. This is caused by hourglass modes and is in correspondence with figure 7.18 where the observation is made that the hourglass ratio of the model with relax stiffness hourglass control has a higher hourglass energy ratio that the model with stiffness hourglass control.

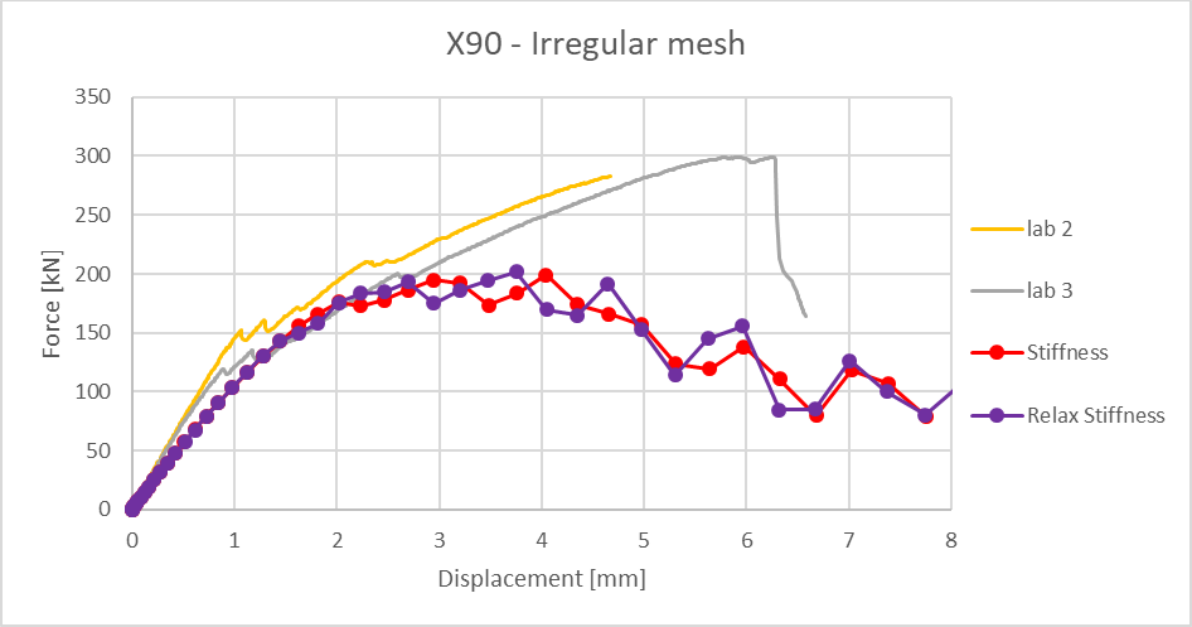

Figure 7.19: Force-displacement curves of irregular models with stiffness and relax stiffness hourglass control.

7.3. CONCLUSIONS

Figures 7.4 and 7.5 show that decreasing the element size reduces the effects of hourglass modes, but only to limited extent. Figure 7.10 shows that hourglass control methods do improve the hourglass behaviour, but do not completely solve the hourglass problem.
In section 7.2 it is shown that the hourglassing problem is solved in the models of axial joints by varying the element sizes through the thickness of the wrap, using wedge elements and by having a finer mesh on the steel-FRP interface, which was shown to be a critical region regarding hourglass modes. This method did not achieve a similar result in the model of the X90 geometry. The mesh was modified to be irregular in the curved plane of the wrap. This did improve the hourglass behaviour significantly, especially when combined with the stiffness hourglass control method. It is believed that introducing more even more irregularity into the mesh will further improve, if not solve, the hourglass problem in these models. This irregularity can be implemented by performing the forming simulation of the wrap mentioned in section 6.2.

8

CONCLUSIONS AND RECOMMENDATIONS

8.1. ELASTIC BEHAVIOUR - GEOMETRY UPGRADES

For all three geometries that have been modelled with the linear elastic approach, very little difference was found when comparing solid elements to continuum shell elements. In section 4.4, it was shown that dividing the FRP piece into layers reduces the stiffness of the models. This is valid for both Abaqus/Standard and Abaqus/Explicit. Abaqus/Explicit was shown to be more accurate in predicting the strength and displacement at failure of the joint and the CPU time was shown to be significantly shorter. Also, Abaqus/Explicit is more suitable for models with complex contact interactions. Therefore it is recommended that Abaqus/Explicit is used instead of Abaqus/Standard when modelling FRP wrapped joints. The use of Abaqus/Explicit implies that continuum shell elements should be used, because it is not possible to model anisotropic material behaviour with solid elements in Abaqus/Explicit. The results obtained with continuum shell elements were satisfactory and continuum shell elements are the only 3D elements which support anisotropic material behaviour in Abaqus/Explicit.

8.2. DEBONDING

In section 5.1 it is shown that in order to model damage propagation properly, the default stiffness option should be used in the CZM. Using the default stiffness option, it is possible to model debonding with high accuracy, however, the models are sensitive to small changes in fracture energy. A reason for this sensitivity is that in these models, the debonding failure mode happens at approximately the same time as yielding in the steel occurs. Values of the shear strength and fracture energy of the bond that give realistic results haven been found, however, no unique set of values of the shear strength and fracture energy could be determined. To determine these values with more certainty, isolated experiments are needed. These experiments could include tensile tests on wrapped axial joints with varying wrapping lengths, to compare FE analyses to. In this way, a unique set of values of shear strength and fracture energy can be found.

8.3. FRP FAILURE

The use of lumped plies, as described in section 6.1, results in premature failure of the model. Modelling the exact layup of the plies results in a better approximation of the

model. However, failure of the wrap occurs earlier than expected, based on the test specimens. This is at least partly caused by the fact that the geometry of the model is slightly different than the geometry of the actual joint, leading to higher stress concentrations in the regions where failure of the wrap is expected. Using this method, the model is a rather good approximation of the layup, but only some distance away from the root of the joint. To better capture the geometry and layup near the root of the joint, a forming simulation is suggested. It is believed that the results of this forming simulation will be a sufficiently accurate approximation of the geometry and layup of the joint. This increase in accuracy in geometry should solve the stress concentrations that cause the premature failure.

8.4. HOURGLASSING

Hourglass modes have a severe influence on the results of the more complex models, especially regarding debonding. The methods available in Abaqus/Explicit for hourglass control do improve the results, but only up to a certain level. Even when using hourglass control methods, the results are still severely influenced by the hourglass modes.
Introducing irregularities in the mesh and refining the mesh in critical locations improves the results. For modelling axial joints, using wedge elements and having a finer mesh on the interface between the steel and FRP suffices to solve the hourglassing problem. For the X90 geometry this strategy is less effective. Modifying the mesh to be irregular in the plane of the layers improves the hourglassing behaviour, but it does not solve it. It is believed that introducing even more irregularity will solve the hourglassing problem. The forming simulation suggested in section 8.3 can be a starting point for introducing more irregularity into the mesh.

BIBLIOGRAPHY

[1] M. Liatzouras, *Feasibility of non-welded CHS steel joints adhesively bonded by GFRP*, Master's thesis, Delft University of Technology (2018).

[2] X. Meng, *Shear Strengthening of Prestressed Hollow Core Slabs Using Externally Bonded Carbon Fiber Reinforced Polymer Sheets*, Master's thesis, University of Windsor (2016).

[3] B. C. KOH and N. KIKUCHI, *New improved hourglass control for bilinear and trilinear elements in anisotropic linear elasticity,* COMPUTER METHODS IN APPLIED MECHANICS AND ENGINEERING **65**, 1 (1987).

[4] *Abaqus Analysis User's Guide (6.14).*

[5] JRC, *Prospect for new guidance in the design of frp,* (2017).

[6] *Abaqus/CAE User's Guide (6.14).*

A

APPENDIX A: STIFFNESS CALCULATIONS

11.6.2.1 UD PLIES

(1) The (mean) stiffness properties of UD plies can be calculated from:

$$E_1 = \left[E_R + (E_{f1} - E_R)\cdot V_f\right]\cdot \varphi_{UD} \tag{11.1}$$

$$E_2 = \left[\frac{(1+\xi_2\eta_2 V_f)}{(1-\eta_2 V_f)}\cdot E_R\right]\cdot \varphi_{UD} \tag{11.2}$$

$$G_{12} = \left[\frac{(1+\xi_G\eta_G V_f)}{(1-\eta_G V_f)}\cdot G_R\right]\cdot \varphi_{UD} \tag{11.3}$$

$$\nu_{12} = \nu_R - (\nu_R - \nu_f)\cdot V_f \tag{11.4}$$

where:

with E_2: $\eta_2 = \dfrac{\left(\frac{E_{f2}}{E_R} - 1\right)}{\left(\frac{E_{f2}}{E_R} + \xi_2\right)}$, $\xi_2 = 2$; with G_{12}: $\eta_G = \dfrac{\left(\frac{G_f}{G_R} - 1\right)}{\left(\frac{G_f}{G_R} + \xi_G\right)}$, $\xi_G = 1$.

In which:

E_1, E_2	is the in plane Young's modulus of the ply in the 1 or 2-direction;
G_{12}	is the in ply shear modulus of the ply;
ν_{12}	is the Poisson's ratio of the fibre reinforced ply;
ν_R	is the Poisson's ratio of the resin;
ν_F	is the Poisson's ratio of the fibre;
ϕ_{UD}	is an empirical reduction factor;
E_R	is the Young's modulus of the resin;
E_{F1}, E_{F2}	is the Young's modulus of the fibre in the 1 or 2-direction;
G_R	is the shear modulus of the resin;
V_f	is the fibre volume ratio of the ply.

The formulas are derived from the semi-empirical Halpin and Tsai equations, where an additional empirical reduction factor $\varphi_{UD} = 0.97$ has been applied.

Figure A.1: Taken from [5]

11.6.2.3 MAT PLY

(1) Using UD ply properties in conformity with 11.6.2.1, the (mean) stiffness properties of mat plies can be calculated from:

$$E_1 = E_2 = \left[\frac{(U_1 + U_4)\cdot(U_1 - U_4)}{U_1}\right]\cdot\varphi_{mat} \tag{11.8}$$

$$G_{12} = \left[\frac{(U_1 - U_4)}{2}\right]\cdot\varphi_{mat} \tag{11.9}$$

$$\nu_{12} = \frac{U_4}{U_1} \tag{11.10}$$

with:

$$U_1 = \frac{3C_{11} + 3C_{22} + 2C_{12} + 4C_{66}}{8}$$

$$U_4 = \frac{C_{11} + C_{22} + 6C_{12} - 4C_{66}}{8}$$

$$C_{11} = \frac{E_{1UD}}{1 - \nu_{12UD}^2 \cdot \frac{E_{2UD}}{E_{1UD}}}$$

$$C_{22} = \frac{E_{2UD}}{1 - \nu_{12UD}^2 \cdot \frac{E_{2UD}}{E_{1UD}}}$$

$$C_{12} = \frac{\nu_{12UD} \cdot E_{1UD}}{1 - \nu_{12UD}^2 \cdot \frac{E_{2UD}}{E_{1UD}}}$$

$$C_{66} = G_{21UD}$$

The formulas are derived from Manera's equations and φ_{mat} is an empirically defined reduction factor of value 0.91.

Figure A.2: Taken from [5]

B

APPENDIX B :ALTERNATIVE GEOMETRIES

B.1. X45 JOINT

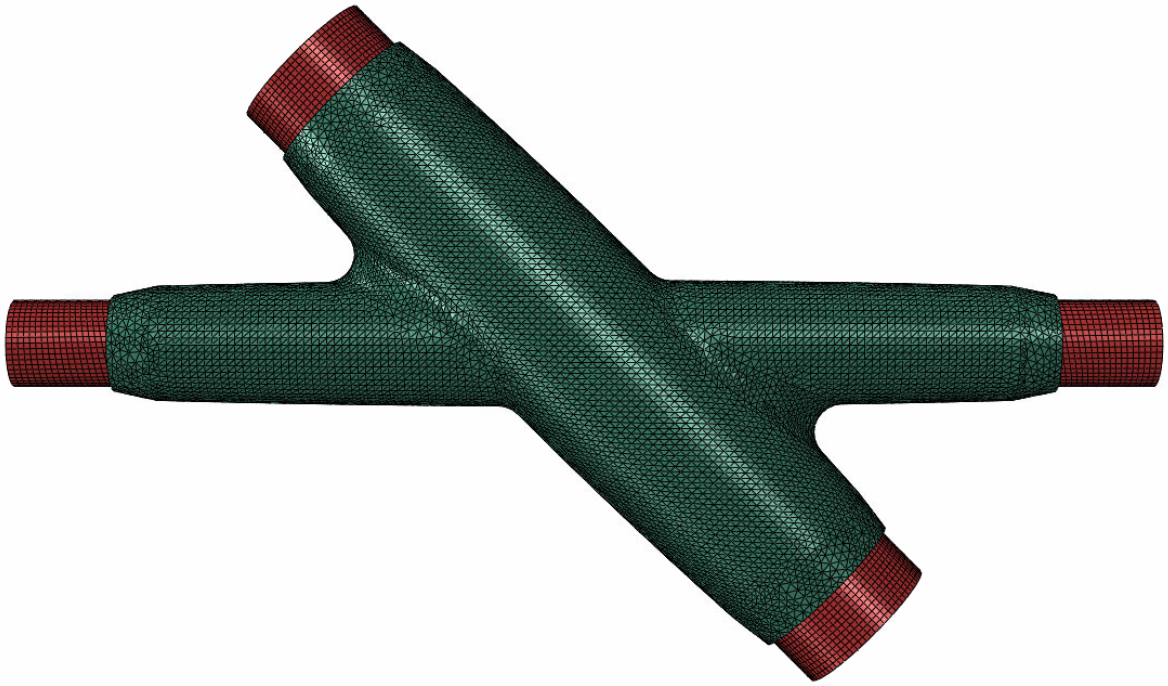

Figure B.1: Geometry of the X45 joint

B.1.1. GEOMETRY ACCORDING TO SPECIFICATION

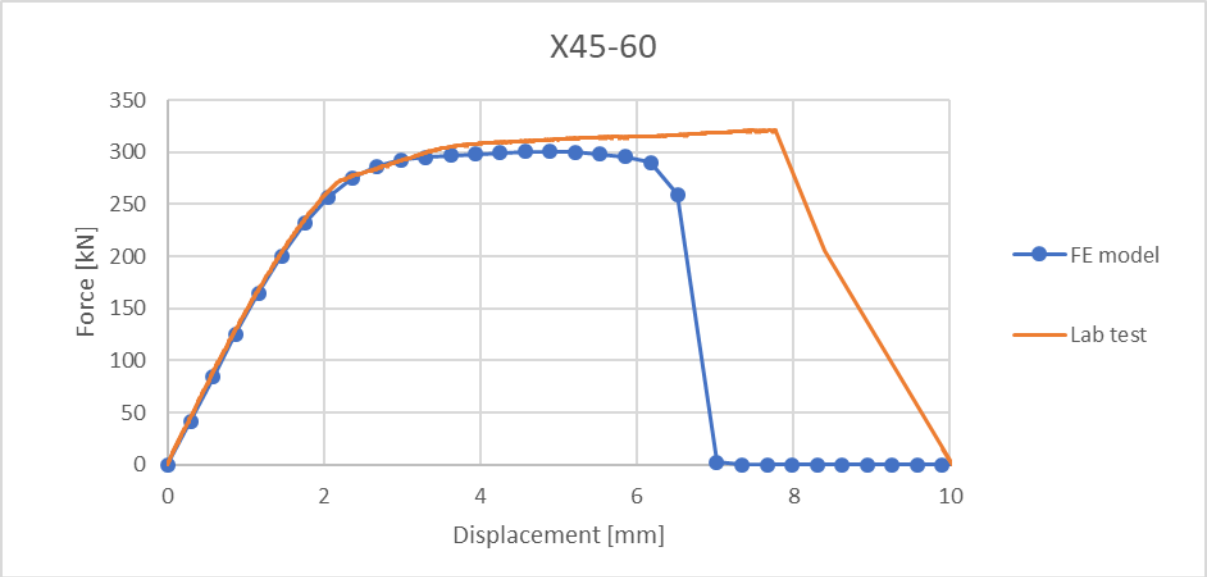

Figure B.2: X45-60 model versus experiment

In figure B.2 it can be seen that the FE model matches the stiffness of the specimen exactly. The model is also very accurate when the stiffness starts to degrade. When the displacement exceeds 3 mm, difference start to occur, this is caused by the appearance of a crack in the specimen. The model does not have this crack as it considers the FRP wrap to be purely elastic. It is expected that when cracking is included in the material model, the model will match the test even better. This is because cracking of the FRP will resolve some stress concentrations because stresses will be redistributed.

COMPARISON OF STRAINS FROM FE MODELS TO DIC RESULTS

Figure B.3 show a comparison between strain results obtained with DIC in the lab and strain results from the model. In figure B.3a, a strain contour from DIC measurements at 2.1 mm displacement is shown, this can be compared to figure B.3b, the strain contour from the FE model at 2.24 mm displacement. It can be seen that the strains have similar values in both images. The strains in the FE model are slightly more spread out compared to the DIC measurements. This is due to difference in the radius of the corner. It is expected that when the corner radii are the same, the strain contours will be more similar.

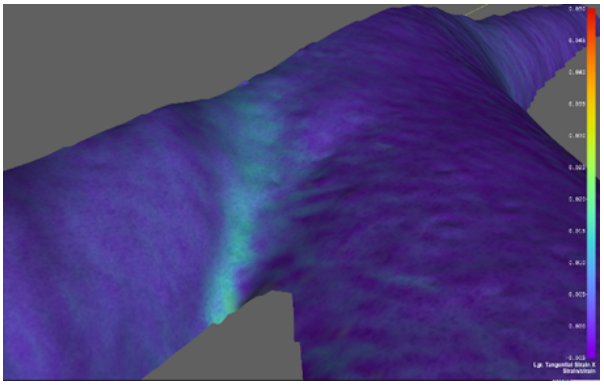

(a) Strain contour from DIC measurements at 2.10 mm displacement

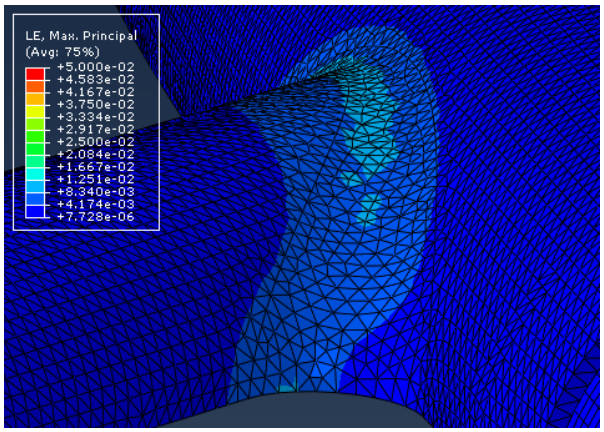

(b) Strain contour from FE model at 2.24 mm displacement

Figure B.3: Comparison of DIC strain results to strain contours from the model at approximately 2.2 mm displacement

In figures B.4a and B.4b the strain contours from DIC and FE model are seen, respectively at 2.95 and 2.88 mm. In the strain contour from the DIC measurements the beginning of a crack is clearly visible as the red band. This crack has not appeared in the strain contour from the FE model. This is because failure of the FRP material is not yet incorporated in the material model that is used

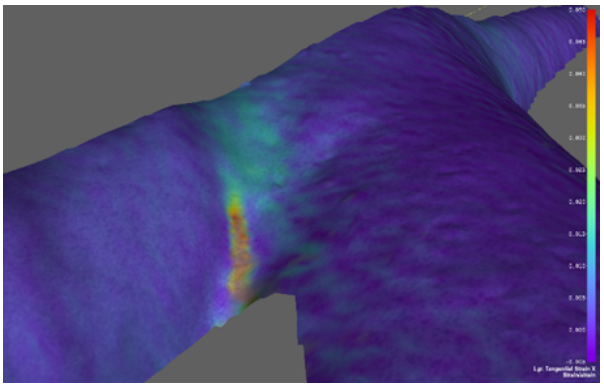

(a) Strain contour from DIC measurements at 2.95 mm displacement

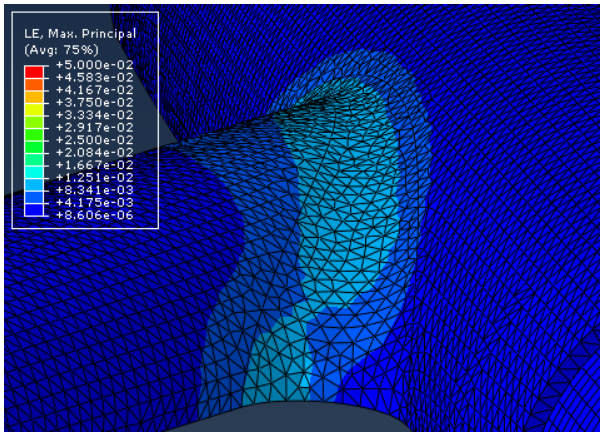

(b) Strain contour from FE model at 2.88 mm displacement

Figure B.4: Comparison of DIC strain results to strain contours from the model at approximately 2.9 mm displacement

B.2. UP-SCALING OF X45 JOINT

Models have been made to investigated suitable dimensions of the FRP wrap for larger scale specimens. The results of this can be seen in figures B.5, B.6 and B.7, the diameter of the brace member is 219 mm. Figure B.5 shows the force-displacement diagrams for a wrapping length of 480 mm with different thicknesses of the wrap. It shows a clear trend that with increasing thickness, the strength and stiffness increase and the displacement at failure decreases. On each force-displacement curve, there is one black dot, this dot marks the moment the ultimate stress is first exceeded. It is clear that both the load and the displacement at the ultimate stress is exceeded increase with increasing thickness of the

wrap.

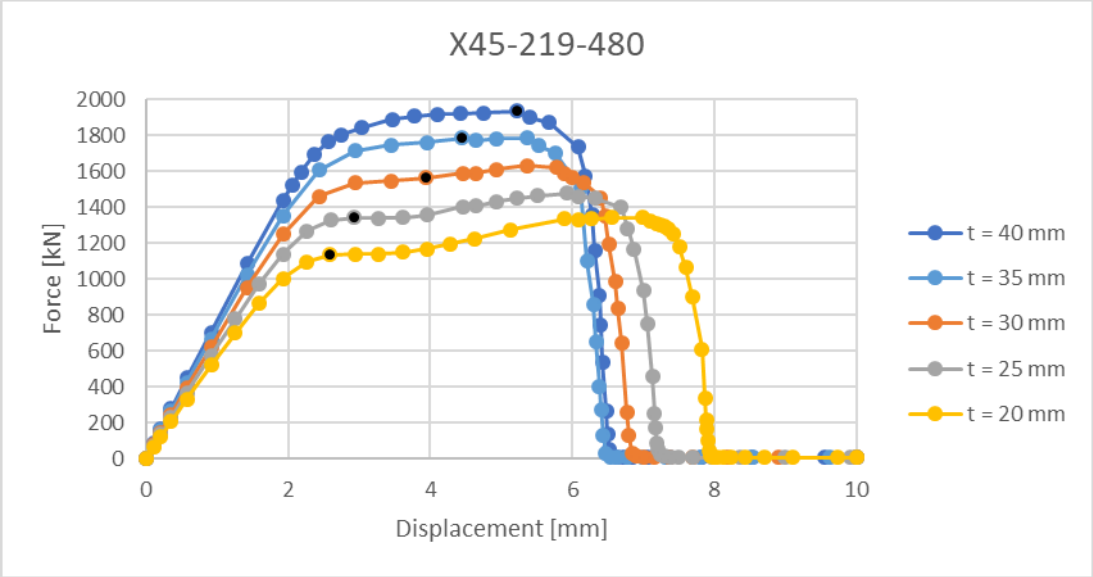

Figure B.5: Thickness variation for a wrapping length of 480 mm

Figure B.6 shows the force-displacement diagrams for a wrapping length of 523 mm with different thicknesses of the wrap. It shows a clear trend that with increasing thickness, the strength and stiffness increase and the displacement at failure decreases. On each force-displacement curve, there is one black dot, this dot marks the moment the ultimate stress is first exceeded. It is clear that both the load and the displacement at the ultimate stress is exceeded increase with increasing thickness of the wrap.

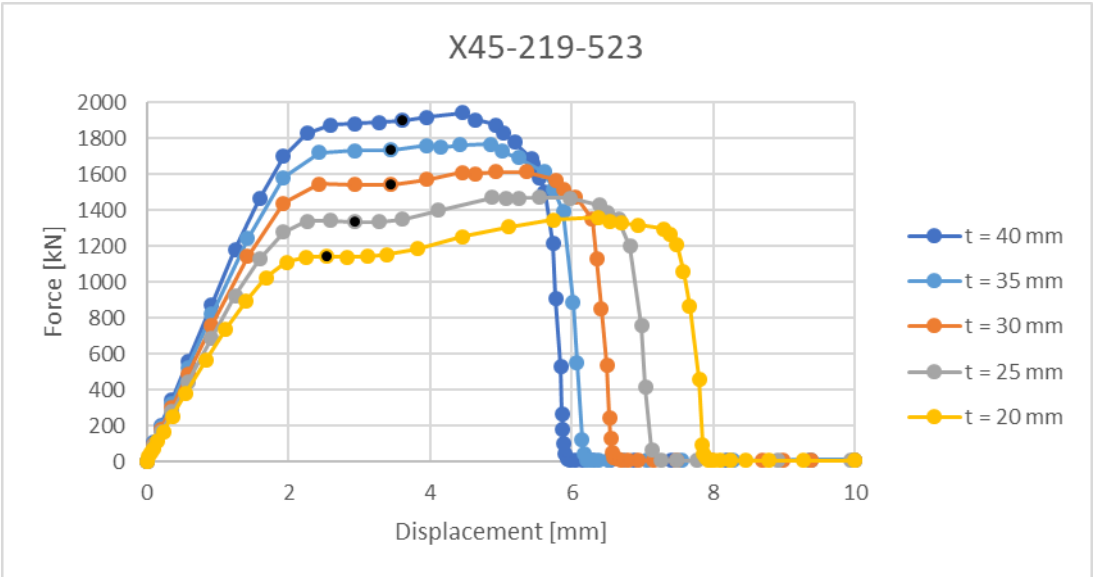

Figure B.6: Thickness variation for a wrapping length of 523 mm

The same trend is observed in figure B.7, where the wrapping length is 628 mm. The strength increases as the wrapping length increases. It is also observed that the increased

wrapping length leads to a higher displacement at failure, but this is at least partly caused by the increased length of the specimen. On each force-displacement curve, there is one black dot, this dot marks the moment the ultimate stress is first exceeded. It is clear that both the load and the displacement at the ultimate stress is exceeded increase with increasing thickness of the wrap. On the force-displacement curve of the model with a wrapping thickness of 40 mm, the ultimate stress is never reached in the FRP.

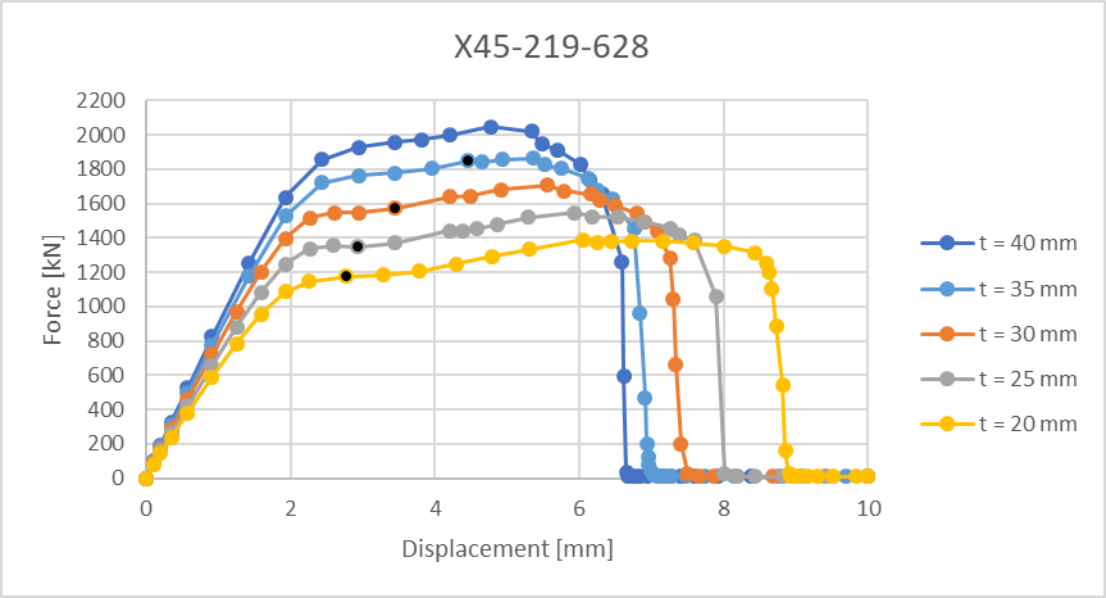

Figure B.7: Thickness variation for a wrapping length of 628 mm

In figure 12, the strength of the joints is shown as a function of the wrapping thickness, we can see that the strength increases with increases thickness but is below the cross-section resistance of the brace member for all thicknesses.

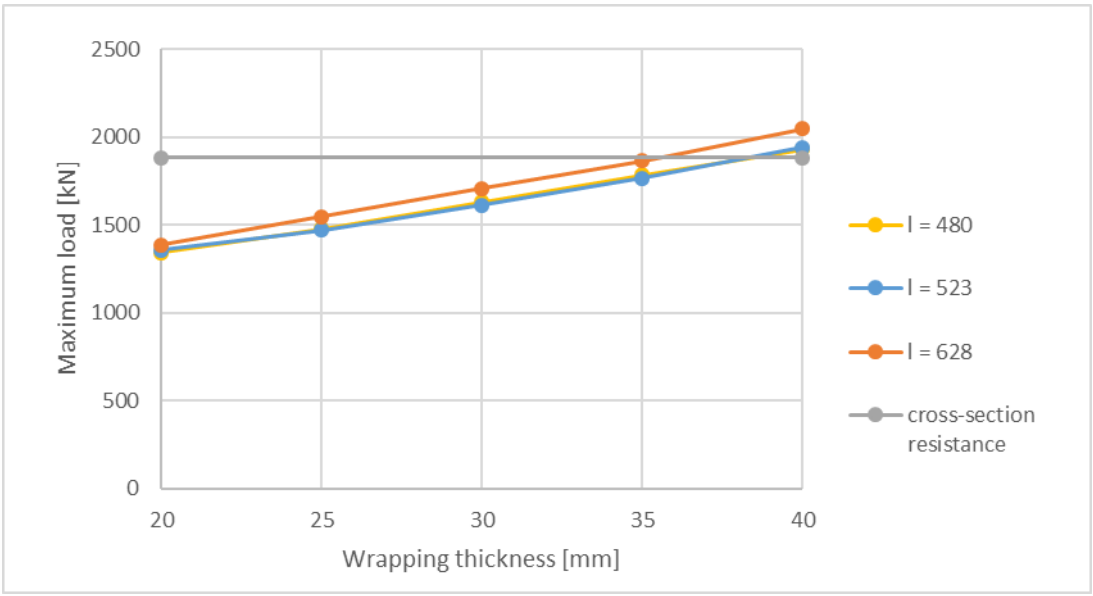

Figure B.8: Influence of wrapping thickness on the strength of the joint

C

INCREASING BOND STRENGTH IN AXIAL JOINT

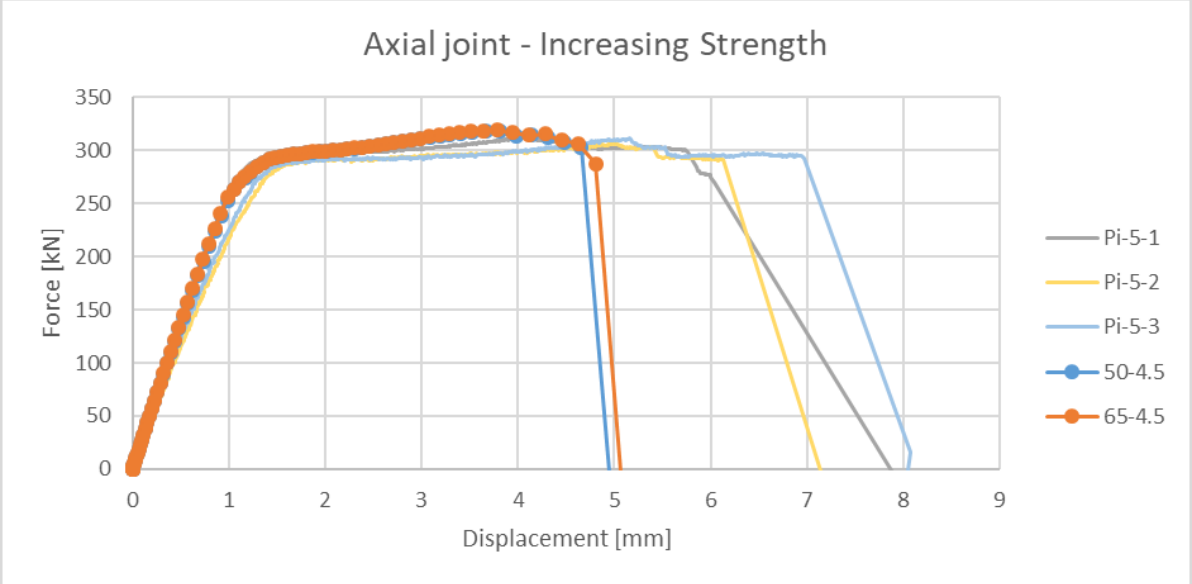

Figure C.1: Increasing the bond strength has a very limited effect on the force-displacement curve of the axial joint.

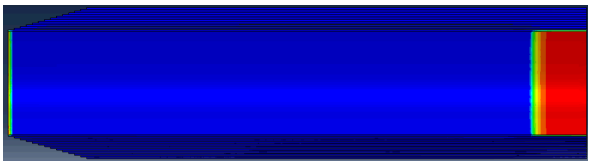

(a) 50-4.5 at 2.2 mm displacement

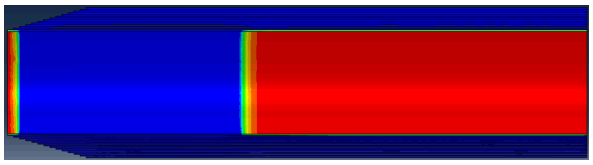

(b) 50-4.5 at 4.5 mm displacement

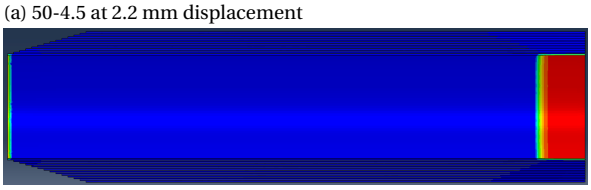

(c) 65-4.5 at 2.2 mm displacement

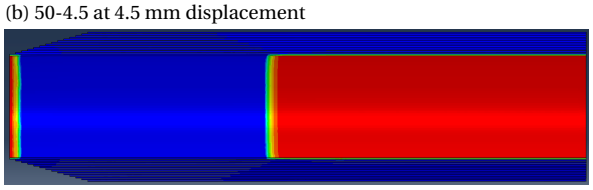

(d) 65-4.5 at 4.5 mm displacement

Figure C.2: Interface damage evolution comparison between shear strength of 50 MPa and 65 MPa. Damage propagating from the left side of the figures is caused by yielding of the steel

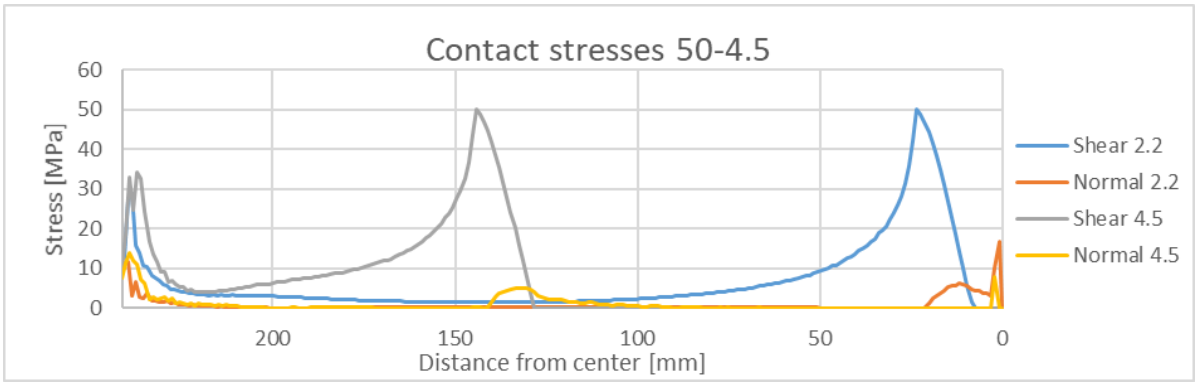

(a) 50-4.5

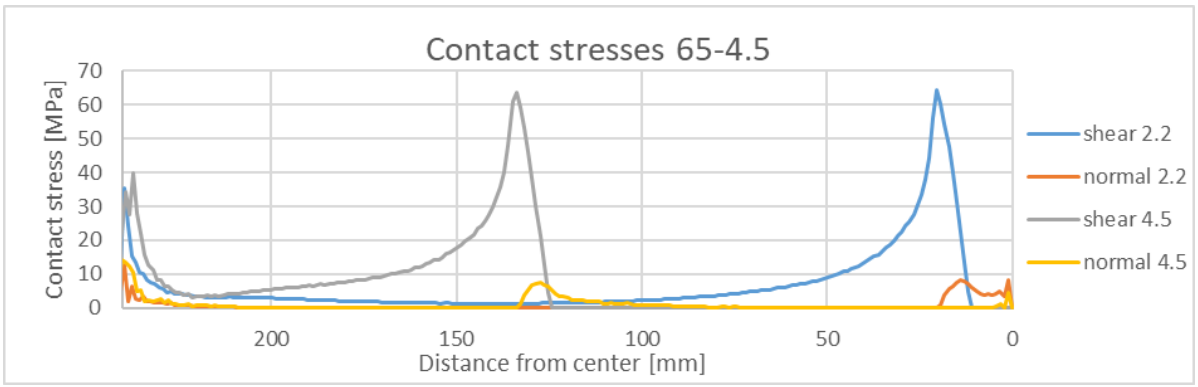

(b) 50-4.6

Figure C.3: Absolute values of contact stresses

D

HIGH STRENGTH STEEL

Figure D.1 shows the force-displacement curve of an axial joint with High Strength Steel. The steel material model used, does not match the steel that is used in the test specimen. However this model can be used to have an indication of the values for strength and fracture energy.

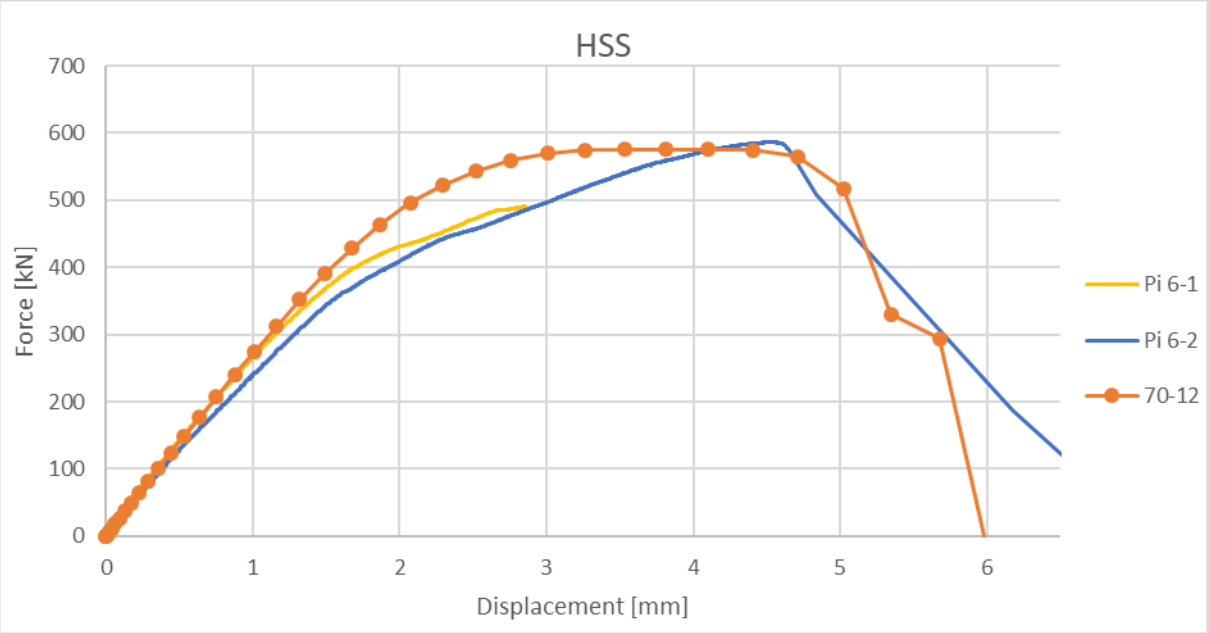

Figure D.1: High Strength Steel, the steel material model does not match the steel used in the test specimen